Thiago Gamboa Ritto

Numerical analysis of the nonlinear dynamics of a drill-string with uncertainty modeling

TESE DE DOUTORADO

DEPARTAMENTO DE ENGENHARIA MECÂNICA
Postgraduate Program in Mechanical Engineering

Rio de Janeiro
April 2010

Pontifícia Universidade Católica
do Rio de Janeiro

Thiago Gamboa Ritto

Numerical analysis of the nonlinear dynamics of a drill-string with uncertainty modeling

Tese de Doutorado

Thesis presented to the Postgraduate Program in Mechanical Engineering of the Departamento de Engenharia Mecânica, Centro Técnico Científico da PUC-Rio as partial fulfillment of the requirements for the degree of Doutor em Engenharia

Advisor: Prof. Rubens Sampaio
Co-Advisor: Prof. Christian Soize

Rio de Janeiro
April 2010

Pontifícia Universidade Católica
do Rio de Janeiro

Thiago Gamboa Ritto

Numerical analysis of the nonlinear dynamics of a drill-string with uncertainty modeling

Thesis presented to the Postgraduate Program in Mechanical Engineering of the Departamento de Engenharia Mecânica, Centro Técnico Científico da PUC-Rio as partial fulfillment of the requirements for the degree of Doutor em Engenharia

Prof. Rubens Sampaio
Advisor
Departamento de Engenharia Mecânica, PUC-Rio

Prof. Christian Soize
Co-Advisor
Laboratoire de Modélisation et Simulation Multi-Echelle (MSME),
Université Paris-Est

Prof. José Roberto de Franca Arruda
Departamento de Mecânica Computational, UNICAMP

Prof. Roger Ohayon
Laboratoire de Mécanique des Structures et des Systèmes Couplés,
CNAM

Prof. Paulo Batista Gonçalves
Departamento de Engenharia Civil, PUC-Rio

Prof. Hans Ingo Weber
Departamento de Engenharia Mecânica, PUC-Rio

Prof. Edson Cataldo
Departamento de Matemática Aplicada, UFF

Prof. José Eugênio Leal
Coordenador Setorial do Centro Técnico Científico – PUC–Rio

Rio de Janeiro, April 15th, 2010

Thiago Gamboa Ritto

Thiago Ritto graduated as mechanical engineer and industrial engineer in 2003 from PUC-Rio (Rio de Janeiro, RJ), and he got his marter's degree in 2005 from the same institution. This DSc. thesis was a joint work between PUC-Rio and Université Paris-Est in a program of double diploma.

Bibliographic data

Ritto, Thiago Gamboa

Numerical analysis of the nonlinear dynamics of a drill-string with uncertainty modeling / Thiago Gamboa Ritto; advisor: Rubens Sampaio; Christian Soize . — 2010.

155 f: ; 30 cm

Tese (Doutorado em Engenharia Mecânica) - Pontifícia Universidade Católica do Rio de Janeiro, Departamento de Engenharia Mecânica, 2010.

Inclui referências bibliográficas.

1. Engenharia mecânica - Teses. 2. Dinâmica não-linear. 3. Modelagem de incertezas. 4. Análise estocástica. 5. Dinâmica de uma coluna de perfuração de petróleo I. Sampaio, Rubens. II. Soize, Christian. III. Pontifícia Universidade Católica do Rio de Janeiro. Departamento de Engenharia Mecânica. IV. Título.

CDD: 621

Acknowledgement

In 3 years and 8 months many things have happened in my life, therefore, I will be economic on the acknowledgements to avoid lapses of memory. However, as this thesis is the result of many random interactions that have occurred, each person that has passed in my live has influenced this final piece.

First, I would like to thank my father Ritto, my mother Nazareth, my brother Fabio and his wife Fernanda for their support, no matter what. Their words and incentive have motivated me a lot to do a great job.

Then, I would like to thank my wife Cristina for all the patience, carrying and love throughout the period of the thesis. She is the one who knows the joy and the distress that I have passed through. She was always there for me.

I have to acknowledge the importance of my two advisors, Rubens Sampaio and Christian Soize, for the present work. They were always available, full of ideas, and restless hard-working. I have learned a lot from them about research and about life. I hope we can work together for a long time.

I would also like to thank the jury: Prof. Ohayon, Prof. Rochinha, Prof. Arruda, Prof. Cataldo, Prof. Weber and Prof. Gonçalves. They contributed for this work, not only for their suggestions in the defense, but also because of our informal talks during the congresses.

I would like to thank my friends and my colleagues of PUC-Rio and Université Paris-Est (many of my colleagues have become my friends). Special thanks to Romulo, Marcelo Piovan, Morad, Charles, Anas and Christophe, who gave me a big help in my work. Thanks for my friends of the French Lab: Isabelle, Charles, Christophe, Évangeline, Morad, Anas, Jéremie, Éric, Moustapha, Amin, Sandra, David, Sulpicio, Bao, Do, Camille, Ziane...(désolé si j'ai oublié quelqu'un)... and my friends of the Brazilian Lab: Rosely, Carlúcio, Márcia, Wagner, Romulo, Julien, Maurício, Mônica, Roberta, Hernan, Josué, Fredy. Special thanks to Wagner, who was present and very helpful all the time.

I have still some persons to thank: Prof. Jean François Deü (CNAM), Prof. James Beck (CALTECH), Prof. Spanos (Rice University), Prof. Marcelo Trindade (USP), Prof. Marcelo Piovan (Bahía Blanca), Prof. André Beck (USP), Prof. Eduardo Cursi (INSA-Rouen), Prof. Juliana Valério (UFRJ), Prof. Roney Thompson (UFF), Prof. Luiz Eduardo Sampaio (UFF), Prof. André Isnard (IFRJ) and Prof. Márcio Carvalho (PUC-Rio). I have learned a lot from them in informal talks.

It was a pleasure to work and to publish with Adriano Fabro, Fernando Buezas, Romulo Aguiar, Rafael Lopes, Maurício Gruzman, Edson Cataldo, Hans Weber, Eduardo Cursi, José Arruda, Roberto Riquelme, and, of course, my two advisors Christian Soize and Rubens Sampaio.

Finally, I would like to acknowledge the financial support of the Brazilian agencies CNPq and CAPES (project CAPES-COFECUB 476/04).

Resumo expandido

Ritto, Thiago Gamboa; Sampaio, Rubens; Soize, Christian. **Análise numérica da dinâmica não-linear de uma coluna de perfuração de petróleo com modelagem de incertezas**. Rio de Janeiro, 2010. 155p. Tese de Doutorado — Departamento de Engenharia Mecânica, Pontifícia Universidade Católica do Rio de Janeiro.

Este trabalho analisa a dinâmica não-linear de uma coluna de perfuração de petroléo incluindo a modelagem de incertezas. A análise realizada é uma anlálise numérica, onde um código computational é desenvolvido para tal propósito. As duas motivações para este trabalho foram (1) a aplicação prática visando a indústria de óleo e gás e (2) a modelagem de incertezas em dinâmica estrutural não-linear. A modelagem de incertezas em dinâmica estrutural é um assunto relativamente novo no Brasil, e, quando se analisam sistemas mecânicos complexos, o papel das incertezas no resultado final pode ser significativo. Uma coluna de perfuração é uma estrutura flexível esbelta que trabalha em rotação e penetra na rocha em busca de petróleo. Esse sistema mecânico é complexo e seu comportamento dinâmico é não-linear. Um modelo matemático-mecânico é desenvolvido para esta estrutura. Primeiramente, as leis da física são usadas para escrever as equações do sistema. Nesta etapa algumas simplificações são feitas para que o modelo numérico seja tratável. Depois, o sistema de equações é discretizado tanto no espaço quanto no tempo. Finalmente, um código computacional é desenvolvido para que simulações numéricas possam ser realizadas para analisar o sistema. O modelo construído inclui interação fluido-estrutura, impacto, não-linearidade geométrica e interação broca-rocha. A coluna de perfuração é modelada como uma viga de Timoshenko. Após a dedução das equações de movimento, o sistema é discretizado usando o método dos elementos finitos. Um código computacional é desenvolvido com a ajuda do programa MATLAB®. A coluna está tracionada na parte superior e comprimida na parte inferior. A dinâmica e vibração da estrutura são observadas em torno desta configuração pré-tensionada. Os modos normais do sistema dinâmico (na configuração pré-tensionada) são usados para construir um modelo reduzido do sistema. Depois da construção do modelo computacional determinístico, faz-se a modelagem de incertezas. Dois tipos de incertezas são considerados: (1) incertezas dos parâmetros e (2) incertezas do modelo. A abordagem probabilística não-paramétrica introduzida por Soize (2000)

é usada nas análises. Esta abordagem é capaz de levar em consideração tanto incertezas nos paramâmetros do sistema quanto incertezas no modelo empregado. As distribuições de probabilidades relacionadas com as variáveis aleatórias do problema são construídas usando o Princípio da Entropia Máxima, e a resposta estocástica do sistema é calculada usando o método de Monte Carlo. Uma nova forma de considerar incertezas (no modelo) de uma equação constitutiva não-linear (interação broca-rocha) é desenvolvida usando a abordagem probabilística não-paramétrica. O modelo de interação broca-rocha usado na análise numérica é simplificado, portanto, é legítimo imaginar que exista incerteza neste modelo. A abordagem probabilística não-paramétrica permite que essas incertezas sejam captadas. Para identificar os parâmetros do modelo probabilístico do modelo de interação broca-rocha, o Princípio da Verossimilhança Máxima é empregado junto com uma redução estatística no domínio da freqüência (usando a Análise das Componentes Principais). Esta redução estatística é necessária para que o problema possa ser resolvido com um tempo de simulação razoável. O objetivo do desenvolvimento de um modelo computacional de um sistema mecânico é usá-lo para melhorar desempenho do sistema, logo, a última etapa deste trabalho é resolver um problema de otimização robusta. Robusta porque as incertezas estão sendo levadas em consideração. Como a probabilidade é usada na modelagem das incertezas, pode-se chamar também de problema de otimização estocástica. Neste problema, propõe-se encontrar os parâmetros operacionais do sistema que maximizam o seu desempenho, respeitando limites de integridade, tais como fadiga e instabilidade torcional. Esta tese, além de investigar a dinâmica de uma coluna de perfuração, também traz uma metodologia de trabalho. De forma simples as etapas são: obter o modelo determinístico do sistema, modelar as incertezas usando a teoria da probabilidade para obter o modelo estocástico, calcular as estatísticas da resposta, identificar os parâmetros do modelo probabilístico, e, finalmente, resolver um problema de otimização considerando a presença de incertezas. Por fim, vale mencionar que este trabalho originou três artigos publicados em revistas internacionais, e mais um artigo está submetido. Outros trabalhos foram desenvolvidos durante o período da tese, o que resultou em mais cinco artigos publicados em revistas internacionais.

Palavras–chave

dinâmica não-linear; modelagem de incertezas; análise estocástica; dinâmica de uma coluna de perfuraçção de petróleo.

Abstract

Ritto, Thiago Gamboa; Sampaio, Rubens; Soize, Christian. **Numerical analysis of the nonlinear dynamics of a drill-string with uncertainty modeling**. Rio de Janeiro, 2010. 155p. DSc. Thesis — Departamento de Engenharia Mecânica, Pontifícia Universidade Católica do Rio de Janeiro.

This thesis analyzes the nonlinear dynamics of a drill-string including uncertainty modeling. A drill-string is a slender flexible structure that rotates and digs into the rock in search of oil. A mathematical-mechanical model is developed for this structure including fluid-structure interaction, impact, geometrical nonlinearities and bit-rock interaction. After the derivation of the equations of motion, the system is discretized by means of the Finite Element Method and a computer code is developed for the numerical computations using the software MATLAB®. The normal modes of the dynamical system in the prestressed configuration are used to construct a reduced-order model of the system. To take into account uncertainties, the nonparametric probabilistic approach, which is able to take into account both system-parameter and model uncertainties, is used. The probability density functions related to the random variables are constructed using the Maximum Entropy Principle and the stochastic response of the system is calculated using the Monte Carlo Method. A novel approach to take into account model uncertainties in a nonlinear constitutive equation (bit-rock interaction model) is developed using the nonparametric probabilistic approach. To identify the probabilistic model of the bit-rock interaction model, the Maximum Likelihood Method together with a statistical reduction in the frequency domain (using the Principal Component Analysis) is applied. Finally, a robust optimization problem is performed to find the operational parameters of the system that maximize its performance, respecting the integrity limits of the system, such as fatigue and torsional instability.

Keywords

nonlinear dynamics; uncertainty modeling; stochastic analysis; drill-string dynamics.

Table of Contents

List of Figures

List of Tables

List of symbols

The symbols are defined on the text, as long as they appear.

Matrices

$[M]$	mass matrix, [kg, kg.m^2]
$[\mathbf{M}]$	random mass matrix, [kg, kg.m^2]
$[C]$	damping matrix, [N.s/m, N.s.m]
$[\mathbf{C}]$	random damping matrix, [N.s/m, N.s.m]
$[K]$	stiffness matrix, [N/m, N.m]
$[\mathbf{K}]$	random stiffness matrix, [N/m, N.m]
$[\mathbf{G}]$	random germ, [–]
[MAC]	matrix of the Modal Assurance Criterion, [–]
$[{}_{\mathsf{a}}T_{\mathsf{b}}]$	transformation matrix from referential b to a, [–]
$[I_t]$	diagonal cross sectional inertia matrix, [m^4]
$[I]$	identity matrix, [–]
$[E]$	strain tensor, [–]
$[S]$	second Piola-Kirchhoff tensor, [Pa]
$[F]$	deformation gradient tensor, [–]
$[D]$	elastic matrix, [Pa]
$[\Phi]$	normal modes matrix, [m, rad]
$[L]$	upper diagonal matrix obtained through decomposition, [$\sqrt{\mathsf{m}}$, $\sqrt{\mathsf{rad}}$]
$[\mathbb{C}]$	covariance matrix, [m^2, rad^2]

Vectors

$\mathbf{u}$	displacement vector, [m, rad]
$\mathbf{U}$	random displacement vector, [m, rad]
$\overline{\mathbf{u}}$	displacement vector about the prestressed configuration, [m, rad]
$\overline{\mathbf{U}}$	random displacement vector about the prestress configuration, [m, rad]
$\mathbf{q}$	generalized displacement vector, [–]
$\mathbf{Q}$	random generalized displacement vector, [–]
$\mathbf{f}$	force vector, [N, N.m]
$\mathbf{F}$	random force vector, [N, N.m]
$\mathbf{N}$	shape function of the finite element, [m]
$\boldsymbol{\epsilon}$	strain tensor written in Voigt notation, [–]
$\boldsymbol{\phi}$	normal mode, [m, rad]
$\mathbf{v}$	velocity vector, [m/s]
$\mathbf{w}$	cross section angular velocity vector, [rad/s]
$\mathbf{S}$	second Piola-Kirchhoff tensor written in Voigt notation, [Pa]
$\mathbf{x}$	Position in the deformed configuration, [m]
$\mathbf{X}$	Position in the non-deformed configuration, [m]
$\mathbf{p}$	displacement field in the non-deformed configuration, [m]

Scalars

t	time, [s]
T	kinetic energy, [N.m]
U	potential energy of deformation; or fluid velocity, [N.m, m/s]
W	work done by the external forces and work not considered in U or T, [N.m]
u	displacement in x-direction, [m]
v	displacement in y-direction, [m]
w	displacement in z-direction, [m]
r	radial displacement $\sqrt{v^2+w^2}$, [m]
R	radius, [m]
D	diameter; or random damage, [m, –]
A	cross sectional area of the column, [m^2]
L	length of the column, [m]
I	cross sectional moment of inertia. [m^4]
E	elasticity modulus, [Pa]
G	shear modulus, [Pa]
k_s	shear factor
l_e	length of the element, [m]
V	volume (integration domain), [m^3]
F	force, [N]
T	torque, [N.m]
$a_1, .., a_5$	constants of the bit-rock interaction model, [m/s, m/(N.s), m/rd, N.rd, N.m]
Z	regularization function (bit-rock interaction model), [–]
e	regularization parameter, [rad/s]
α_1, α_2	positive constants of the bit-rock interaction model
M_f	mass per unit length of the fluid, [kg/m]
ρ_f	fluid density, [kg/m^3]
p	fluid pressure, [Pa]
C_f	fluid damping coefficient, [–]
k	fluid damping coefficient, [–]
g	gravity acceleration, [m/s^2]
h	head loss, [m]
conv	convergence function of the stochastic solution, [m^2.t]
L	log-likelihood function, [–]
J	objective function of the optimization problem, [m/s]
$\mathcal{R}$	mathematical expectation of the rate of penetration, [m/s]
P_risk	risk allowed, [–]
$\mathfrak{ss}$	stick slip stability factor, [–]
$\mathcal{S}$	random stick slip stability factor, [–]

Greek symbols

δ	symbol of variation; or dispersion parameter, [–]
Π	total potential of the system, [N.m.t]
θ_x	rotation about x-axis [rad]
θ_y	rotation about y-axis [rad]
θ_z	rotation about z-axis [rad]
ξ	element coordinate, [–]
ρ	mass density of the material of the column, [kg/m^3]
ν	Poisson coefficient; or frictional coefficient, [–]
μ	1st Lame constant, [Pa]
λ	2nd Lame constant, [Pa]
σ	Von Mises stress, [Pa]
$\mathfrak{S}$	random Von Mises stress, [Pa]
τ	shear stress, [Pa]
ϵ	strain, [–]
ω	frequency; or rotational speed, [rad/s]
χ	factor relating the diameter of the borehole with the outer diameter, [–]

Subscripts

br	bit-rock
bit	bit
ch	channel (or borehole)
ke	kinetic energy
se	strain energy
NL	nonlinear
stab	stabilizer
r	reduced system
e	element
f	fluid
g	geometric (for $[K]$) and gravity (for $\mathbf{f}$)
p	polar
S	static response
x	x-direction
y	y-direction
z	z-direction
i	inner diameter; or inside
o	outer diameter; or outside
M	mass matrix
C	damping matrix
K	stiffness matrix
G	random germ matrix

Other definitions

(x, y, z)	Cartesian coordinate system
$\dot{f} = \partial f / \partial t$	time derivative of function f
$f' = \partial f / \partial x$	spatial derivative of function f
∇f	gradient of f
$< \cdot, \cdot >$	Euclidian inner product
$\| \cdot \|$	norm associated with the Euclidian inner product
$[A]^T$	transpose of matrix $[A]$
tr$([A])$	trace of matrix $[A]$
$\|[A]\|_F$	Frobenius norm of matrix $[A]$
$\mathcal{E}\{X\}$	mathematical expectation of random variable X
p_X	probability density function of random variable X
$\mathbb{1}_B(x)$	indicator that is equal to one if $x \in B$ and is equal to zero otherwise
sign(a)	indicator that is equal to one if $a \geq 0$ and is equal to zero if $a < 0$

Abbreviations

BHA	Bottom hole assembly
TOB	Torque on bit
WOB	Weight on bit
ROP	Rate of penetration
DOC	Depth of cut
FEM	Finite Element Method

If a man will begin with certainties, he shall end in doubts; but if he will be content to begin with doubts, he shall end in certainties.

Sir Francis Bacon, 1605.

1
Introduction

1.1
Context of the thesis

We are interested in the dynamics and control of flexible structures used in engineering applications, such as turbines, airplanes, vehicles, bridges etc. In especial, this work analyzes the nonlinear dynamics of a drill-string system, which is described in Chapter 2. The modeling of complex structures is difficult and the numerical predictions usually differ from real data. One of the reasons for such fact is that uncertainties play an important role in many complex dynamical systems. To improve the predictions of the computational model, uncertainties must be taken into account.

The Brazilian research community in the field of structural dynamics in mechanical engineering is making efforts to create a group to understand, to apply, and to teach mathematical tools that can help on uncertainty quantification and stochastic modeling. In 2008, a committee called *Comitê de Quantificação de Incertezas e Modelagem Estocástica* (`http://www.abcm.org.br/comites/comitesQualificacaoIncertezas.shtml`) was created in the *Associação Brasileira de Engenharia e Ciências Mecânicas* (ABCM), which is the Brazilian Society of Engineering and Mechanical Science.

On the other hand, the French research community has some tradition in stochastic modeling in the field of structural dynamics in mechanical engineering. For example, Prof. Soize published a book in 1983 ([60]) about random mechanics.

The field of stochastic modeling and uncertainty quantification is challenging and several mathematical tools are necessary for the applications. The present thesis is not intended to be a basic material for this subject; those people are encouraged to read, for instance, [103, 114, 117].

In 2008 and 2009 two seminars in uncertainty quantification and

stochastic modeling were organized by Professor Rubens Sampaio at PUC-Rio. Besides presentations given by the Professors that compose the ABCM committee and their students, short courses were provided by Professor Christian Soize (*Université Paris-Est*, France), Professor Eduardo Souza de Cursi (*INSA de Rouen*, France) and Professor Nicholas Zabaras (Cornell University, USA). In 2009 and 2010, Brazilian researchers organized mini-symposiums of uncertainty quantification and stochastic modeling in traditional conferences, such as *Congresso Ibero-Latino de Métodos Computationais em Engenharia* (CILAMCE), International Congress of Mechanical Engineering (COBEM) and Pan-American Congress of Applied Mechanics (PACAM).

1.2 Uncertainty modeling

Imagine a real system for which we intend to construct a computational model. What is called computational model is the mathematical-mechanical model that is implemented as a computer code. In many cases, experimental tests are too expensive or even not feasible. In these cases, virtual (computational) experiments are advantageous. The idea is to use the computational model to improve the performance of a mechanical system and/or to reduce the number of experiments. Moreover, uncertainties must be taken into account. We will consider two types of uncertainties [115]:

1. Parameter uncertainties are uncertainties related to the parameters of a computational model. For example, the diameter of the shaft, the density of the material, the damping coefficient, etc.

2. Model uncertainties are uncertainties related to the model itself. The computational model used might be wrong due to incomplete information and unmodeled phenomena. For example, simplifications introduced in order to decrease the complexity of the model.

We differ uncertainties from numerical errors, which are related to the construction of the approximations of the computational model. For example, error due to the Finite Element Method approximation, error due to the numerical integration scheme and round-off errors. These errors can and should be controlled [29].

There are several ways of taking into account uncertainties in a dynamical system. In a general way, two approaches can be considered: the

probabilistic approach and the non-probabilistic approach. In the present work, the probabilistic approach is used to model the uncertainties, since we consider it the most powerful one. As examples of non-probabilistic approaches see, for instance, the Fuzzy method and the Interval method [75].

In the middle of the XVII century, Blaise Pascal together with Pierre de Fermat established the basis of the probability theory and combinatory analysis. Pierre Simon Laplace [62, 63] has made a huge contribution to this field, setting out a mathematical system of inductive reasoning based on probability. He has given a broader interpretation for the Bayes theorem [7]. It was only in 1933 that the Russian Andrey Kolmogorov [57] established formally the probability axioms.

In structural dynamics, we are concerned about (random) vibration analysis. Random vibration analysis has its origin in the work of Einstein about the Brownian motion [34], and the history of random vibration, from 1905 until Crandall seminar of 1958, can be found in [79]. Crandall made the random vibration analysis accessible for non-researcher engineers through his seminar of 1958. There are some books about random vibration analysis with random excitation of linear and nonlinear dynamical systems; see, for instance, [26, 66, 61, 69] and, more recently [133]. The classical study of random vibration considers random excitation forces.

To model uncertainties within the parameters of the computational model, we should use the parametric probabilistic approach. See its first applications in dynamical systems in [132, 108], some general developments can be found in [56, 39, 35] and some general methods for computational stochastic mechanics are in [105]. This approach is very efficient to take into account parameter uncertainties. Nevertheless, model uncertainties can not be modeled with the parametric probabilistic approach.

A recent approach called nonparametric probabilistic approach can be used to take into account model uncertainties for dynamical systems. It was introduced by Soize [112, 113, 116, 115, 120] and it is very well suited when simplifications are introduced in order to decrease the complexity of the deterministic model (for example, a cylindrical elastic body modeled using the beam theory). The nonparametric approach uses the random matrix theory [71, 43, 17].

A crucial step when using the probabilistic approach is the choice of the probability distribution for the random variables. Data should guide the construction of the probabilistic model, which is given by the probability distribution or the probability density function of the random variables. One

way to choose the probability distribution is through a hypothesis test, such as the chi-square and the Kolmogorov-Smirnov [18, 98]. Another way, is to construct the probabilistic model using the Maximum Entropy Principle [107, 49, 50]. Applying this principle, only the available information is used to calculate the probability density function that maximizes the entropy (see Chapter 4), *i.e.*, we are opting for the least prejudice probabilistic model that is coherent with the physics of the problem. If data are available, the probabilistic model constructed using the Maximum Entropy Principle can be updated using Bayesian statistics (see, for instance, [111, 9, 21, 16]).

Figures 1.1 to 1.4 show a scheme that summarizes the steps of the computational analysis. First, a nominal (deterministic) computational model is constructed, then, uncertainties are modeled (see Fig. 1.1). The system considered in the analysis is a flexible dynamical system that is discretized by means of the Finite Element Method, and the probabilistic model is constructed using the Maximum Entropy Principle. After the uncertainty modeling, we have a stochastic computational model that enable us to do stochastic simulations, which generate the random responses that are analyzed using statistics (see Fig. 1.1). The Monte Carlo method [98] is used to analyze the propagation of the uncertainty throughout the dynamical system. The next step is to identify the parameters of the stochastic model using data from experimental results (see Fig. 1.2). The Maximum Likelihood method [3] is used for the identification procedure. The main goal of the computational stochastic model is to help improving the system performance (see Fig. 1.3). In this step a robust optimization problem has to be solved. The *a priori* probabilistic model might be updated if data are available using the Bayesian approach (see Fig. 1.4). However, this step is not performed in the present work.

Figure 1.1: From deterministic to stochastic analysis.

1.3 Objectives of the thesis

The first objective of this thesis is to develop a deterministic model for the drill-string dynamics that takes into account the main forces acting

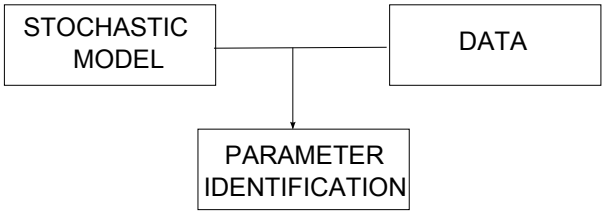

Figure 1.2: Identification of the stochastic parameters.

Figure 1.3: Robust optimization.

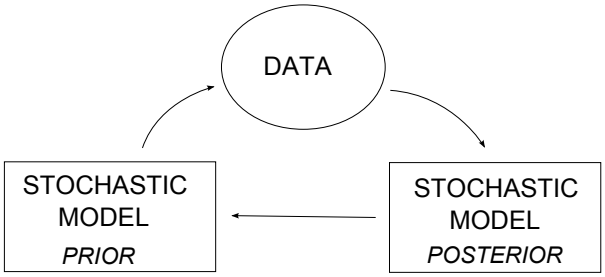

Figure 1.4: Model updating.

on the system. This includes, for instance, bit-rock interaction, geometric nonlinearities, impacts and fluid-structure interaction. The second objective is to develop a probabilistic model for the drill-string dynamics and to obtain the stochastic response (there are few works that analyze the random response of a drill-string [58, 127]). The third objective is to propose a procedure to identify the probabilistic model of the bit-rock interaction model. Finally, the forth objective is to perform a robust optimization problem to find the best operational parameters of the system, respecting the integrity limits, such as fatigue and torsional instability.

1.4 Organization of the thesis

The thesis is organized as following. First, in Chapter 2, the problem of the drill-string is presented. The deterministic model of the drill-string is described in Chapter 3 and the probabilistic model of the drill-string is

described in Chapter 4. Finally, in Chapter 5, the results are summarized and future works are discussed.

2
Drill-string problem

The oil exploitation has begun around 1850 in the United States of America with oil wells of approximately twenty meters of depth. The depth achieved in a perforation has been growing over the years due to the increasing demand and the technological innovations of the sector. For example, the maximum depth achieved by a drill-string in 1977 was of 277 meters in Brazil, nowadays it is common to see drill-strings 2000 meters long. The exploitation of oil and gas is a complex activity. This thesis analyzes one step of the oil exploitation, which is the drilling process, with special attention to the dynamic behavior of the structure. Figure 2.1 shows the main components of a drilling equipment. A quick explanation of each component can be found in the glossary `http://www.glossary.oilfield.slb.com/`.

The exploitation of oil and gas involves the following steps (`http://www.lrc.usace.army.mil`):

1) Identification of the local where the exploitation will be done,

2) Economic viability analysis,

3) Identification of the best places for the drilling process,

4) Drilling process,

5) Analysis of the geological formation found,

6) Construction of an unit of exploitation and beginning of the exploitation.

There are many units of exploitation that use rotating columns (drill-strings) for the drilling process. This process consists on cutting the rock using a bit, in rotation, conducted by a column that transmits the torque generated by the rotary table located at the surface. The column gives the necessary weight (weigh on bit, WOB) to drill the rock. A drill-string is composed by drill pipes, drill collars and a bit. The lower part of the column is called Bottom Hole Assembly (BHA) and it has a length of approximately two hundred meters, even though the total length

1. Crown block
2. Traveling block and hook
3. Drawwork
4. Swivel
5. Hose
6. Tube
7. Mud pump
8. Kelly
9. Rotary drive
10. Rotary table
11. Drill pipe
12. Tool joint
13. Stabilizers
14. Drill collar
15. Bit
16. Casing
17. Blowout preventer
18. Derrick

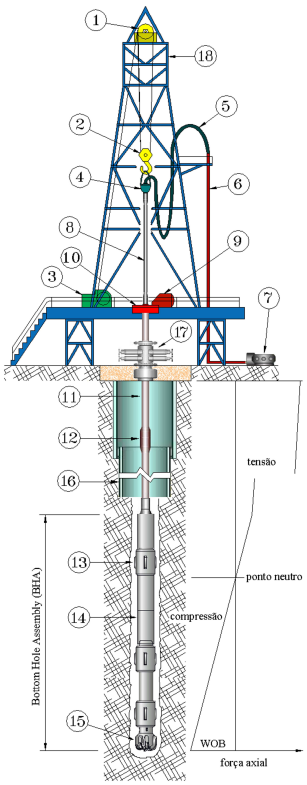

Figure 2.1: Typical drilling equipment.

of the column might have some kilometers. This part is under compression and is composed by the drill-collars, tubes with larger diameters and thicker walls. The drill-string is a slender structure that might be twisted several times because of the torque on bit (TOB).

Another important element on the drilling process is the drilling fluid (or mud) (see Fig. 2.2, `http://www.lrc.usace.army.mil`). The mud is used for: refrigeration, displacement of the drilled solids and stability of the well wall. It plays also a role in the drill-string dynamics.

The dynamics of a drill-string is complicated, consisting on coupled axial, lateral and torsional vibrations. Figure 2.3 illustrates these vibrations.

The relation between excessive vibration and instability in the drilling process was observed in [104], where in two case studies the instability was due to vibration problems, such as stick-slip, bit-bounce and whirl. They are described as following:

• Stick-slip happens when the friction between the bit and the rock is big. The bit might eventually get stuck and then, after accumulating energy in terms of torsion, be suddenly released. This phenomenon generates torsional vibrations and can be identified by periodic oscillations on the

Figure 2.2: Drilling fluid (mud).

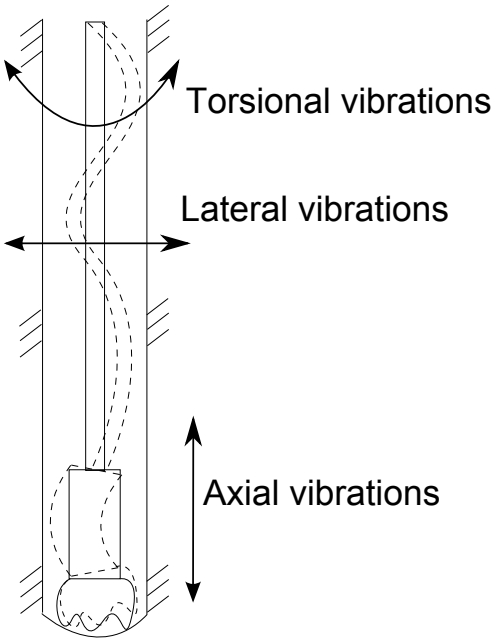

Figure 2.3: Axial, lateral and torsional vibrations are coupled.

torque.

• Bit-bounce happens when the bit looses contact with the rock, hitting it in the sequence with great strength. This phenomenon generates axial vibrations and can be identified by periodic vibrations on the weight of the column.

• Whirl is a lateral instability that is intensified by impacts between the column and the borehole. This phenomenon generates lateral vibrations and can be identified by the increasing of these vibrations and harmonics in the frequency spectrum.

The drill-string vibrations are induced by the characteristics of the bit-rock interaction and by the impacts that might occur between the column and the borehole [31]. If not controlled, vibrations are harmful to the drilling process causing:

1. Premature wear and consequent damage of the drilling equipment, resulting many times in failures, especially due to fatigue.
2. Decrease of the rate of penetration (ROP), increasing the well cost [28].
3. Interferences on the measurements performed during the drilling process and damage of the measurement equipment [64].
4. Significant waste of energy.
5. BHA instability, reducing the directional control [31].

Some typical drill-string failures are discussed in the following article [70]. The cost of repairing a failure is approximately two times the cost of the prevention. The most common types of failures are: ductile failure, fragile failure, and crack due to fatigue and corrosion under tension (see Fig. 2.4, taken from [70]). Although the mechanisms of failure are well understood, the harmful environment and the type of excitation make the failure difficult to be avoided. The equipment performance is getting better with the improvement of the control and inspection techniques. At this point, the understanding of the structure dynamics is essential. A computational model of the drill-string can and should be used to develop a strategy of vibration control, allowing the optimization of its performance. Nevertheless, the controlling strategy is not considered in this work.

It should be noted that it is very limiting to analyze each vibration (axial, lateral and torsional) separately, since usually they are all coupled. Some computational models have been developed to analyze the coupling between two or three vibration directions (see, for instance, Yigit and Christoforou works [134, 135, 24], or Khulief et al. [55], and also Sampaio et al. [128, 101]). The mentioned works and the present work consider only a vertical well, however, there are other possibilities for the drilling process, as illustrated in Fig. 2.5 (`http://www.lrc.usace.army.mil`).

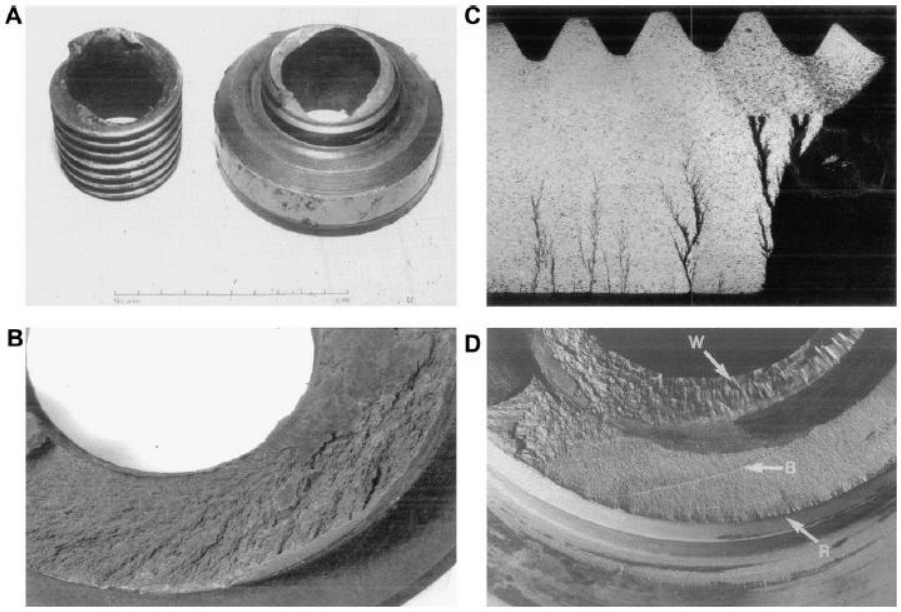

Figure 2.4: Typical failures: A) ductile, B) fragile, C) and D) fatigue.

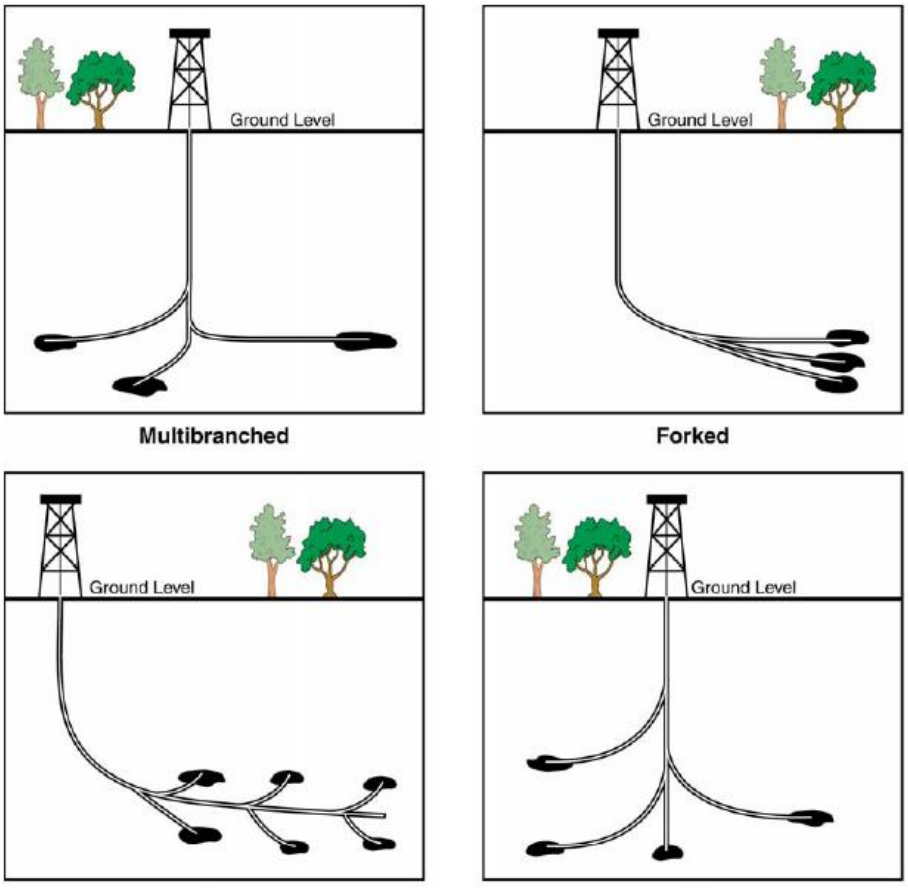

Figure 2.5: Different directions of drilling.

3
Deterministic model

There are still many challenges involving the modeling of the complex dynamics of a drill-string, which includes bit-rock interaction, fluid-structure interaction, coupling vibrations and also impact. A general vibration perspective overview of the process of oil well rotary drilling can be found in the works of Spanos et al. [125, 127]. In the work of Jogi et al. [51], some drill-string models are used and compared with field data (to compute natural frequencies). These models ([82], [44], [33]) were developed in the 1990s and use the beam theory combined with the finite element method. Paslay et al. [82] performs separate computations for lateral displacements, and axial and torsional vibrations. This model includes the effect of the fluid added mass, but neglects impacts between the column and the borehole. Heisig [44] considers spatially curved boreholes and takes into account impacts between the column and the borehole, but the dynamical response is calculated only for two situations: a given bit displacement or a given mass imbalance. In the Jansen's PhD thesis [47], the nonlinear dynamics of an oil well drill-string is analyzed. A detailed discussion of the drill-string problem is presented and simple computational models are simulated. Jansen [47] also presents the nonlinear formulation of an Euler-Bernoulli beam, but some elements are not considered, such as stabilizers, bit-rock interaction and fluid-structure interaction (the fluid is considered in a simplistic way).

Figure 3.1 sketches a drill-string system. The upper region is composed by thin tubes called drill-pipes and the bottom region (bottom hole assembly, BHA) is composed by thicker tubes called drill-collars.

There are some ways to model the nonlinear dynamics of a drill-string, *e.g.*, see the papers of Christoforou and Yigit [134, 23, 24], the papers of Tucker and Wang [129, 130], the papers of Khulief et al. [54, 55], the paper of Richard et al. [84], the thesis of Alamo [2], and also the papers of Sampaio et al. [128, 101]. Each author uses a different approach to the problem: Christoforou and Yigit use a one-mode approximation to analyze the problem, Khulief et al. and Sampaio et al. use the Euler-Bernoulli beam

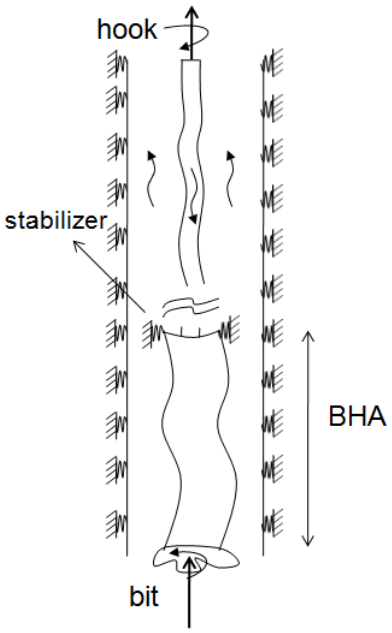

Figure 3.1: Sketch of a drill-string.

model with the Finite Element Method, Richard et al. use a discrete system with two degrees of freedom, while Tucker and Wang, and Alamo, use the Cosserat theory. None of these works consider a fluid-structure interaction that takes into account the drilling fluid that flows inside and outside of the column. In references [129, 24] the influence of the fluid is considered in a simplistic way. In [13], the fluid-structure interaction model developed in [5] is used. This model considers the column rotating immersed in a fluid, but the axial flow of the fluid is neglected. In the present work, the fluid-structure interaction model proposed in [81] is employed in the analysis, as explained in the sequence.

We want to construct a nominal model that takes into account the main forces acting on the column, therefore, the fluid-structure interaction must be considered. The drilling fluid (mud) is responsible for transporting the cuttings (drilled solids) from the bottom to the top to avoid borehole clogging. The fluid flows downward inside the column and then upward in the annulus. It also plays an important role in cooling the bit and stabilizing the system [1]. The mud has complex rheological properties, see for instance [25]. There are some papers that analyze only the drilling-fluid flow, as, for example, [36, 37, 83].

A simple fluid-structure interaction model that neglects the rotation of the fluid is used. (Note that the fluid should rotate, since the column rotates.) This model considers the fluid that flows downward inside the

column and then upward in the annulus. It is an extension of the one developed in [81] and it permits the influence of the fluid to be computed by adding an axial force and three matrices, which are constant in time (mass, damping and stiffness).

Comparing to what is found in the literature, the proposed model is the most complete one, since it uses the Timoshenko beam theory combined with finite strain (using all the terms of the Green-Lagrange strain) and all the important forces of the system are taken into account. The equations of motion are derived using the extended Hamilton Principle and discretized by means of the Finite Element Method.

3.1 Base Model

In this Section the base model without the fluid-structure interaction is described. The fluid-structure interaction model is discussed in Section 3.2. The basic references for the finite element formulation developed in this Section are [109, 110, 46, 65, 27, 6, 137, 138].

Previous papers (see, for instance [55, 128, 24]) have used the Euler-Bernoulli beam theory (which neglects shear deformation) to model the drill-string. In this work the Timoshenko beam theory (which considers shear deformation) is used because (1) it includes the Euler-Bernoulli theory and (2) it allows more flexibility in applications. A 3D beam model is used with six degrees of freedom for each interpolation point (see Fig.3.2): three translational displacements of the neutral line (axial u, lateral in y-axis v and lateral in z-axis w) and three rotations of the cross sections (about the x-axis θ_x, about the y-axis θ_y and about the z-axis θ_z). It is assumed small angles for θ_y and θ_z, which is justified because the vibration of the column is constrained inside the borehole, however, θ_x is finite.

The equations of motion are derived using the extended Hamilton Principle in which the first variation of the potential Π must vanish:

$$\delta\Pi = \int_{t_1}^{t_2} (\delta U - \delta T - \delta W) dt = 0\,, \tag{3-1}$$

where U is the potential strain energy, T is the kinetic energy and W is the work done by the nonconservative forces and by any force not accounted in the potential energy.

The system is discretized using the Finite Element Method, with the element displacements and rotations written as

$$\begin{aligned} u_e(\xi,t) &= \mathbf{N}_u(\xi)\mathbf{u}_e(t), \quad & v_e(\xi,t) &= \mathbf{N}_v(\xi)\mathbf{u}_e(t), \\ w_e(\xi,t) &= \mathbf{N}_w(\xi)\mathbf{u}_e(t), \quad & \theta_{xe}(\xi,t) &= \mathbf{N}_{\theta_x}(\xi)\mathbf{u}_e(t), \\ \theta_{ye}(\xi,t) &= \mathbf{N}_{\theta_y}(\xi)\mathbf{u}_e(t), \quad & \theta_{ze}(\xi,t) &= \mathbf{N}_{\theta_z}(\xi)\mathbf{u}_e(t) \end{aligned} \tag{3-2}$$

where t is time, ξ is the element coordinate ($\xi = x/l_e$), l_e is the length of the element, $\mathbf{N}$ are the shape functions written as line vectors (see appendix A) and the element displacement vector is written as $\mathbf{u}_e = \begin{pmatrix} u_1 & v_1 & \theta_{z1} & w_1 & \theta_{y1} & \theta_{x1} & u_2 & v_2 & \theta_{z2} & w_2 & \theta_{y2} & \theta_{x2} \end{pmatrix}^T$; where $(\cdot)^T$ denotes transpose. Figure 3.2 shows the two node finite element used in the computational model.

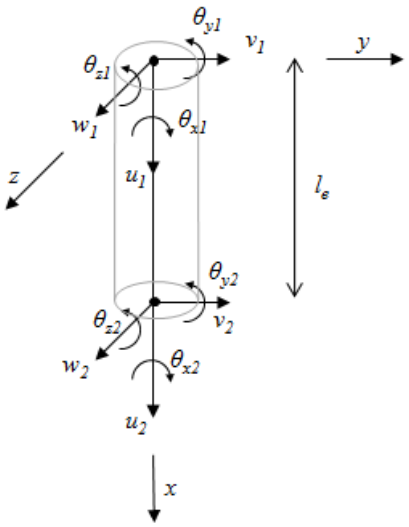

Figure 3.2: Two node finite element with six degrees of freedom per node.

Note that:

$$\begin{aligned} dx &= l_e d\xi\,, \\ \frac{\partial v}{\partial x} &= \frac{\partial v}{\partial \xi}\frac{\partial \xi}{\partial x} = \frac{\partial v}{\partial \xi}\frac{1}{l_e}\,, \\ \frac{\partial^2 v}{\partial x^2} &= \frac{\partial}{\partial x}\left(\frac{\partial v}{\partial x}\right) = \frac{\partial^2 v}{\partial \xi^2}\frac{1}{l_e^2}\,, \end{aligned}$$

where these operations are also valid for u, w, θ_x, θ_y, and θ_z. Denoting the time derivative by a superposed dot and the spatial derivative by $(')$ we have:

$$\dot{v}_e = \mathbf{N}_v \dot{\mathbf{u}}_e \,,$$
$$\frac{\partial v_e}{\partial x} = \frac{\partial (\mathbf{N}_v \mathbf{u}_e)}{\partial x} = \mathbf{u}_e \frac{\partial \mathbf{N}_v}{\partial \xi} \frac{\partial \xi}{\partial x} = \frac{\mathbf{N}'_v \mathbf{u}_e}{l_e} \,,$$
$$\delta v_e = \mathbf{N}_v \delta \mathbf{u}_e \,,$$
$$\delta w_e v_e = (\delta \mathbf{u}_e^T \mathbf{N}_w^T)(v_e) = \delta \mathbf{u}_e^T (\mathbf{N}_w^T \mathbf{N}_v) \mathbf{u}_e \,,$$
$$u_e v_e \delta w_e = (\delta \mathbf{u}_e^T \mathbf{N}_w^T)(u_e v_e) = (\delta \mathbf{u}_e^T \mathbf{N}_w^T)(\mathbf{N}_u \mathbf{u}_e)(\mathbf{N}_v \mathbf{u}_e) \,,$$

where these operations are also valid for u, θ_x, θ_y, and θ_z.

3.1.1 Gravity

The work done by gravity is written as:

$$W = \int_0^L \rho g A u \, dx \,, \tag{3-3}$$

where ρ is the mass density, A is the cross-sectional area, L is the length of the column and g is the gravity acceleration. The variation of Eq. (3-3) gives

$$\delta W = \int_0^L \rho g A \delta u \, dx \,, \tag{3-4}$$

and the discretization by means of the finite element method yields the force element vector

$$(\mathbf{f}_{\mathrm{g}})^{(e)} = \int_0^1 \mathbf{N}_u^T \rho g A \, l_e d\xi \,. \tag{3-5}$$

3.1.2 Kinetic energy

The kinetic energy is written as

$$T = \frac{1}{2} \int_0^L \rho (A \mathbf{v}^T \mathbf{v} + \mathbf{w}^T [I_t] \mathbf{w}) \, dx \,, \tag{3-6}$$

where $\mathbf{v}$ is the velocity vector, $[I_t]$ is the cross-sectional inertia matrix and $\mathbf{w}$ is the section angular velocity vector:

$$\mathbf{v} = \begin{pmatrix} \dot{u} \\ \dot{v} \\ \dot{w} \end{pmatrix} \ , \ [I_t] = \begin{bmatrix} I_p & 0 & 0 \\ 0 & I & 0 \\ 0 & 0 & I \end{bmatrix} \ , \ \mathbf{w} = \begin{pmatrix} \dot{\theta}_x + \theta_y \dot{\theta}_z \\ \cos(\theta_x)\dot{\theta}_y - \sin(\theta_x)\dot{\theta}_z \\ \sin(\theta_x)\dot{\theta}_y + \cos(\theta_x)\dot{\theta}_z \end{pmatrix} , \tag{3-7}$$

where I is the cross-sectional moment of inertia and I_p is the polar moment of inertia.

$$\begin{aligned} I &= \int_A z^2 dA = \int_A y^2 dA = \frac{\pi}{64}(D_o^4 - D_i^4) \, , \\ I_p &= \int_A (z^2 + y^2) dA = 2I \, , \end{aligned} \tag{3-8}$$

where D_i and D_o are the inner and the outer diameter of the column.

To calculate $\mathbf{w}$, the rotations have been parameterized in the following way. The matrix that transforms a vector written in (x_1, y_1, z_1) to the inertial reference (x, y, z) is (see Fig. 3.3):

$$[{}_0T_1] = \begin{pmatrix} 1 & 0 & 0 \\ 0 & cos(\theta_x) & -sin(\theta_x) \\ 0 & sin(\theta_x) & cos(\theta_x) \end{pmatrix} .$$

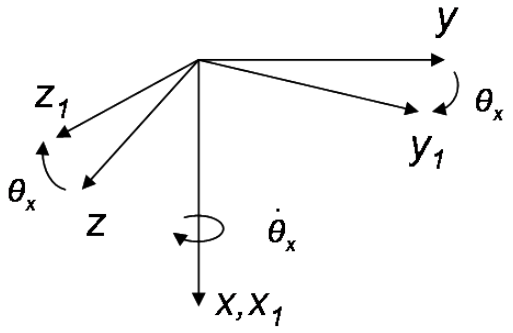

Figure 3.3: Rotation about the x-axis

The matrix that transforms a vector written in (x_2, y_2, z_2) to (x_1, y_1, z_1) is (see Fig. 3.4):

$$[{}_1T_2] = \begin{pmatrix} cos(\theta_y) & 0 & sin(\theta_y) \\ 0 & 1 & 0 \\ -sin(\theta_y) & 0 & cos(\theta_y) \end{pmatrix}.$$

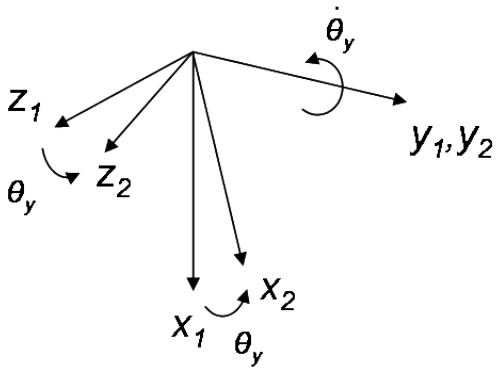

Figure 3.4: Rotation about the y_1-axis

For small θ_y:

$$[{}_1T_2] = \begin{pmatrix} 1 & 0 & \theta_y \\ 0 & 1 & 0 \\ -\theta_y & 0 & 1 \end{pmatrix}.$$

The matrix that transforms a vector written in (x_3, y_3, z_3) to (x_2, y_2, z_2) is (see Fig. 3.5):

$$[{}_2T_3] = \begin{pmatrix} cos(\theta_z) & -sin(\theta_z) & 0 \\ sin(\theta_z) & cos(\theta_z) & 0 \\ 0 & 0 & 1 \end{pmatrix}.$$

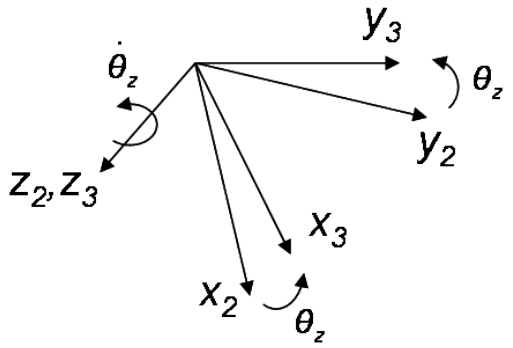

Figure 3.5: Rotation about the z_2-axis

For small θ_z:

$$[{}_2T_3] = \begin{pmatrix} 1 & -\theta_z & 0 \\ \theta_z & 1 & 0 \\ 0 & 0 & 1 \end{pmatrix}.$$

The angular velocity vector written in the inertial frame (x, y, z) can be calculated as following:

$$\mathbf{w} = \begin{pmatrix} \dot{\theta}_x \\ 0 \\ 0 \end{pmatrix}_{(x,y,z)} + [{}_0T_1] \begin{pmatrix} 0 \\ \dot{\theta}_y \\ 0 \end{pmatrix}_{(x_1,y_1,z_1)} + [{}_0T_1][{}_1T_2] \begin{pmatrix} 0 \\ 0 \\ \dot{\theta}_z \end{pmatrix}_{(x_2,y_2,z_2)} =$$

$$= \begin{pmatrix} \dot{\theta}_x + \theta_y \dot{\theta}_z \\ cos(\theta_x)\dot{\theta}_y - sin(\theta_x)\dot{\theta}_z \\ sin(\theta_x)\dot{\theta}_y + cos(\theta_x)\dot{\theta}_z \end{pmatrix}. \tag{3-9}$$

Note that the rotational speed about the x-axis $\dot{\theta}_x$ is not constant, therefore the discretization of kinetic energy yields a constant mass matrix $[M]$ and a nonlinear force vector $\mathbf{f}_{\text{ke}}$ that couples axial, torsional and lateral vibrations. The mass element matrix is written as:

$$\begin{aligned} [M]^{(e)} = \int_0^1 [\rho A(\mathbf{N}_u^T\mathbf{N}_u + \mathbf{N}_v^T\mathbf{N}_v + \mathbf{N}_w^T\mathbf{N}_w) + \\ +\rho I(\mathbf{N}_{\theta_y}^T\mathbf{N}_{\theta_y} + \mathbf{N}_{\theta_z}^T\mathbf{N}_{\theta_z}) + \rho I_p(\mathbf{N}_{\theta_x}^T\mathbf{N}_{\theta_x})]\, l_e d\xi\,. \end{aligned} \tag{3-10}$$

Using the rotational speeds $\dot{\theta}_{xe} = \mathbf{N}_{\theta_x}\dot{\mathbf{u}}_e$, $\dot{\theta}_{ye} = \mathbf{N}_{\theta_y}\dot{\mathbf{u}}_e$, $\dot{\theta}_{ze} = \mathbf{N}_{\theta_z}\dot{\mathbf{u}}_e$ and the angular accelerations $\ddot{\theta}_{xe} = \mathbf{N}_{\theta_x}\ddot{\mathbf{u}}_e$, $\ddot{\theta}_{ye} = \mathbf{N}_{\theta_y}\ddot{\mathbf{u}}_e$, $\ddot{\theta}_{ze} = \mathbf{N}_{\theta_z}\ddot{\mathbf{u}}_e$, the nonlinear force element vector due to the kinetic energy is written as:

$$\mathbf{f}_{\text{ke}}^{(e)} = \rho I_p \int_0^1 \left[\mathbf{N}_{\theta_x}^T(\theta_{ye}\ddot{\theta}_{ze} + \dot{\theta}_{ye}\dot{\theta}_{ze}) + \mathbf{N}_{\theta_z}^T(\theta_{ye}\ddot{\theta}_{xe} + \dot{\theta}_{ye}\dot{\theta}_{xe}) - \mathbf{N}_{\theta_y}^T(\dot{\theta}_{xe}\dot{\theta}_{ze})\right] l_e d\xi\,. \tag{3-11}$$

3.1.3 Strain energy

The strain energy is written as:

$$U = \frac{1}{2}\int_V \boldsymbol{\epsilon}^T \mathbf{S} dV\,, \tag{3-12}$$

where V is the integration domain, $\boldsymbol{\epsilon}$ is the Green-Lagrange strain tensor and $\mathbf{S}$ is the second Piola-Kirchhoff stress tensor (written in Voigt notation):

$$\boldsymbol{\epsilon} = \begin{pmatrix} \epsilon_{xx} \\ \epsilon_{yy} \\ \epsilon_{zz} \\ 2\epsilon_{xy} \\ 2\epsilon_{xz} \\ 2\epsilon_{yz} \end{pmatrix} \quad , \quad \mathbf{S} = \begin{pmatrix} \sigma_{xx} \\ \sigma_{yy} \\ \sigma_{zz} \\ \tau_{xy} \\ \tau_{xz} \\ \tau_{yz} \end{pmatrix} .$$

Traditionally, the engineering strain is used in the Voigt notation; that is why the last three terms of the strain are multiplied by two. Let's consider the constitutive relation of a isotropic material with linear elasticity as:

$$[S] = 2\mu[E] + \lambda \mathrm{tr}([E])[I] \,, \tag{3-13}$$

where $[S]$ is the second Piola-Kirchhoff stress tensor, $[E]$ is the Green strain tensor and $\mathrm{tr}(\cdot)$ is the trace of a matrix. The Lame's constants are defined by:

$$\mu = \frac{E}{2(1+\nu)} \quad , \quad \lambda = \frac{E\nu}{(1+\nu)(1-2\nu)} \,, \tag{3-14}$$

where E is the elasticity modulus and ν is the Poisson coefficient. $[S]$ and $[E]$ may be written as:

$$[S] = \begin{bmatrix} \sigma_{xx} & \tau_{xy} & \tau_{xz} \\ \tau_{xy} & \sigma_{yy} & \tau_{yz} \\ \tau_{xz} & \tau_{yz} & \sigma_{zz} \end{bmatrix} \quad , \quad [E] = \begin{bmatrix} \epsilon_{xx} & \epsilon_{xy} & \epsilon_{xz} \\ \epsilon_{xy} & \epsilon_{yy} & \epsilon_{yz} \\ \epsilon_{xz} & \epsilon_{yz} & \epsilon_{zz} \end{bmatrix} . \tag{3-15}$$

In indicial notation, the stress and strain relation, Eq. (3-13), may be written as:

$$[S]_{ij} = D_{ijkl}[E]_{kl} \,, \tag{3-16}$$

where D_{ijkl} is the forth order tensor that establishes the linear elastic model between the Green strain and the second Piola-Kirchhoff stress tensors.

The deformation gradient tensor relative to the reference position is given by $[F] = d\mathbf{x}/d\mathbf{X}$, with $\mathbf{x}$ for the deformed configuration and $\mathbf{X}$ for the reference configuration. The Green-Lagrangian strain tensor may be written as $[E] = 1/2([F]^T[F] + [I])$, where $[I]$ is the identity matrix (see appendix B). Equation (3-16) is written in Voigt notation as:

$$\mathbf{S} = [D]\boldsymbol{\epsilon}\,, \tag{3-17}$$

and for isotropic materials we have

$$[D] = \frac{E(1-\nu)}{(1+\nu)(1-2\nu)} \begin{bmatrix} 1 & \frac{\nu}{(1-\nu)} & \frac{\nu}{(1-\nu)} & 0 & 0 & 0 \\ \frac{\nu}{(1-\nu)} & 1 & \frac{\nu}{(1-\nu)} & 0 & 0 & 0 \\ \frac{\nu}{(1-\nu)} & \frac{\nu}{(1-\nu)} & 1 & 0 & 0 & 0 \\ 0 & 0 & 0 & \frac{1-2\nu}{2(1-\nu)} & 0 & 0 \\ 0 & 0 & 0 & 0 & \frac{1-2\nu}{2(1-\nu)} & 0 \\ 0 & 0 & 0 & 0 & 0 & \frac{1-2\nu}{2(1-\nu)} \end{bmatrix}.$$

Using the beam hypothesis, which means that the dimension in x is much bigger than dimensions in y and z, we assume that $\sigma_{yy} \sim \sigma_{zz} \sim \tau_{yz} \sim 0$ and $\epsilon_{yy} \sim \epsilon_{zz} \sim \epsilon_{yz} \sim 0$. Thus:

$$\boldsymbol{\epsilon} = \begin{pmatrix} \epsilon_{xx} \\ 2\epsilon_{xy} \\ 2\epsilon_{xz} \end{pmatrix} \quad , \quad \mathbf{S} = \begin{pmatrix} \sigma_{xx} \\ \tau_{xy} \\ \tau_{xz} \end{pmatrix} ,$$

$$[D] = \begin{bmatrix} E & 0 & 0 \\ 0 & k_s G & 0 \\ 0 & 0 & k_s G \end{bmatrix} ,$$

where $G = \mu = E/2(1+\nu)$ is the shear modulus and k_s is the shearing factor that depends on the cross section area. The strain tensor can be obtained through

$$[E] = \frac{1}{2}\left[\left(\frac{d\mathbf{p}}{d\mathbf{X}}\right) + \left(\frac{d\mathbf{p}}{d\mathbf{X}}\right)^T + \left(\frac{d\mathbf{p}}{d\mathbf{X}}\right)^T \left(\frac{d\mathbf{p}}{d\mathbf{X}}\right)\right] , \tag{3-18}$$

where $\mathbf{X} = (x\ y\ z)^T$ is the position on the non-deformed configuration

and $\mathbf{p} = (u_x\ u_y\ u_z)^T$ is the displacement field written in the non-deformed configuration, such that

$$\begin{aligned} u_x &= u - y\theta_z + z\theta_y\,, \\ u_y &= v + y(\cos(\theta_x) - 1) - z\sin(\theta_x)\,, \\ u_z &= w + z(\cos(\theta_x) - 1) + y\sin(\theta_x)\,. \end{aligned} \tag{3-19}$$

The displacement field can be deduced by translating the center point of a cross sectional area by $(u\ v\ w)^T$, then rotating the plane of this section θ_x, θ_y and θ_z (with the hypothesis of small rotations θ_y and θ_z).

$$(\mathbf{p})_0 = \begin{pmatrix} u_x \\ u_y \\ u_z \end{pmatrix}_0 = \begin{pmatrix} u \\ v \\ w \end{pmatrix}_0 + (\mathbf{x})_0 - (\mathbf{X})_0\,, \tag{3-20}$$

where the subscript 0 refers to the non-deformed configuration and:

$$(\mathbf{X})_0 = \begin{pmatrix} 0 \\ y \\ z \end{pmatrix}_0\,, \quad (\mathbf{x})_0 = [{}_0T_3] \begin{pmatrix} 0 \\ y \\ z \end{pmatrix}_3 \tag{3-21}$$

where $[{}_0T_3] = [{}_0T_1][{}_1T_2][{}_2T_3]$. Back to the strain energy, we have:

$$U = \frac{1}{2}\int_V \boldsymbol{\epsilon}^T \mathbf{S} dV = \frac{1}{2}\int_V \boldsymbol{\epsilon}^T [D] \boldsymbol{\epsilon} dV = \frac{1}{2}\int_V \left[E(\epsilon_{xx}^2) + 4k_s G(\epsilon_{xy}^2 + \epsilon_{xz}^2)\right] dV\,, \tag{3-22}$$

where

$$\begin{aligned} \epsilon_{xx} &= \frac{\partial u_x}{\partial x} + \frac{1}{2}\left(\frac{\partial u_x}{\partial x}\frac{\partial u_x}{\partial x} + \frac{\partial u_y}{\partial x}\frac{\partial u_y}{\partial x} + \frac{\partial u_z}{\partial x}\frac{\partial u_z}{\partial x}\right)\,, \\ \epsilon_{xy} &= \frac{1}{2}\left(\frac{\partial u_y}{\partial x} + \frac{\partial u_x}{\partial y} + \frac{\partial u_x}{\partial x}\frac{\partial u_x}{\partial y} + \frac{\partial u_y}{\partial x}\frac{\partial u_y}{\partial y} + \frac{\partial u_z}{\partial x}\frac{\partial u_z}{\partial y}\right)\,, \\ \epsilon_{xz} &= \frac{1}{2}\left(\frac{\partial u_z}{\partial x} + \frac{\partial u_x}{\partial z} + \frac{\partial u_x}{\partial x}\frac{\partial u_x}{\partial z} + \frac{\partial u_y}{\partial x}\frac{\partial u_y}{\partial z} + \frac{\partial u_z}{\partial x}\frac{\partial u_z}{\partial z}\right)\,. \end{aligned} \tag{3-23}$$

The discretization of the linear terms yields the stiffness matrix $[K]$ and the discretization of the higher-order terms yields the nonlinear force vector $\mathbf{f}_{\mathrm{se}}$ that couples axial, torsional and lateral vibrations. In fact, the dynamics takes place around a prestressed configuration (see Section 3.3) and the constant geometric stiffness matrix $[K_{\mathrm{g}}(\mathbf{u}_{\mathrm{S}})]$ is used, where $\mathbf{u}_{\mathrm{S}}$ is the prestressed state. There is no simplification, all the terms obtained from the strain energy are used in the formulation. The stiffness element matrix is written as:

$$
\begin{aligned}
[K]^{(e)} = \int_0^1 \Bigg[& \frac{EA}{l_e}\left(\mathbf{N}_u'^T\mathbf{N}_u'\right) + \frac{k_sGI_p}{l_e}\left(\mathbf{N}_{\theta_x}'^T\mathbf{N}_{\theta_x}'\right) + \frac{EI}{l_e}\Big(\mathbf{N}_{\theta_y}'^T\mathbf{N}_{\theta_y}' + \\
& + \mathbf{N}_{\theta_z}'^T\mathbf{N}_{\theta_z}'\Big) + \frac{k_sGA}{l_e}\left(\mathbf{N}_v'^T\mathbf{N}_v' + \mathbf{N}_w'^T\mathbf{N}_w'\right) + k_sGAl_e\Big(\mathbf{N}_{\theta_y}^T\mathbf{N}_{\theta_y} + \\
& + \mathbf{N}_{\theta_z}^T\mathbf{N}_{\theta_z}\Big) + k_sGA\Big(\mathbf{N}_v'^T\mathbf{N}_{\theta_z} + \mathbf{N}_{\theta_z}^T\mathbf{N}_v' + \mathbf{N}_w'^T\mathbf{N}_{\theta_y} + \mathbf{N}_{\theta_y}^T\mathbf{N}_w'\Big)\Bigg]\, d\xi\,,
\end{aligned}
\tag{3-24}
$$

where $(u_e)' = \dfrac{1}{l_e}\mathbf{N}_u'\mathbf{u}_e$, $(v_e)' = \dfrac{1}{l_e}\mathbf{N}_v'\mathbf{u}_e$, $(w_e)' = \dfrac{1}{l_e}\mathbf{N}_w'\mathbf{u}_e$, $(\theta_{xe})' = \dfrac{1}{l_e}\mathbf{N}_{\theta_x}'\mathbf{u}_e$, $(\theta_{ye})' = \dfrac{1}{l_e}\mathbf{N}_{\theta_y}'\mathbf{u}_e$, $(\theta_{ze})' = \dfrac{1}{l_e}\mathbf{N}_{\theta_z}'\mathbf{u}_e$. The geometric stiffness element matrix, when the only nonzero displacement is the axial one ($\mathbf{u}_{\mathrm{S}}$), may be written as

$$
\begin{aligned}
([K_{\mathrm{g}}(\mathbf{u}_{\mathrm{S}})])^{(e)} = (u_e)' \int_0^1 \Bigg[& \frac{AE}{(l_e)^2}\left(\mathbf{N}_v'^T\mathbf{N}_v' + \mathbf{N}_w'^T\mathbf{N}_w' + 3\mathbf{N}_u'^T\mathbf{N}_u'\right) + \\
& + \frac{k_sGA}{l_e}\Big(\mathbf{N}_v'^T\mathbf{N}_{\theta_z} + \mathbf{N}_w'^T\mathbf{N}_{\theta_y} + \mathbf{N}_{\theta_z}^T\mathbf{N}_v' + \mathbf{N}_{\theta_y}^T\mathbf{N}_w' + 2l_e\mathbf{N}_{\theta_z}^T\mathbf{N}_{\theta_z} + \\
& + 2l_e\mathbf{N}_{\theta_y}^T\mathbf{N}_{\theta_y}\Big) + \frac{EI}{(l_e)^2}\Big(2\mathbf{N}_{\theta_x}'^T\mathbf{N}_{\theta_x}' + 3\mathbf{N}_{\theta_y}'^T\mathbf{N}_{\theta_y}' + 3\mathbf{N}_{\theta_z}'^T\mathbf{N}_{\theta_z}'\Big)\Bigg] l_e d\xi + \\
& + (u_e)'^2 \int_0^1 \Bigg[k_sGA\Big(\mathbf{N}_{\theta_y}^T\mathbf{N}_{\theta_y} + \mathbf{N}_{\theta_z}^T\mathbf{N}_{\theta_z}\Big) + \frac{EI}{(l_e)^2}\Big(\mathbf{N}_{\theta_x}'^T\mathbf{N}_{\theta_x}' + \frac{3}{2}\mathbf{N}_{\theta_y}'^T\mathbf{N}_{\theta_y}' \\
& + \frac{3}{2}\mathbf{N}_{\theta_z}'^T\mathbf{N}_{\theta_z}'\Big) + \frac{EA}{(l_e)^2}\Big(\frac{3}{2}\mathbf{N}_u'^T\mathbf{N}_u' + \frac{1}{2}\mathbf{N}_v'^T\mathbf{N}_v' + \frac{1}{2}\mathbf{N}_w'^T\mathbf{N}_w'\Big)\Bigg] l_e d\xi\,.
\end{aligned}
\tag{3-25}
$$

The nonlinear force element vector due to the strain energy is written

as:

$$(\mathbf{f}_{\text{se}})^{(e)} = \int_0^1 \Big[\mathbf{N}_u'^T f_1 + \mathbf{N}_v'^T f_2 + \mathbf{N}_w'^T f_3 + \mathbf{N}_{\theta_x}'^T f_4 + \mathbf{N}_{\theta_y}'^T f_5 + \\ + \mathbf{N}_{\theta_z}'^T f_6 + \mathbf{N}_{\theta_x}^T f_7 + \mathbf{N}_{\theta_y}^T f_8 + \mathbf{N}_{\theta_z}^T f_9 \Big] \, l_e d\xi \,, \tag{3-26}$$

where $f_1, .., f_9$ are found in appendix C.

3.1.4 Impact, rubbing and stabilizers

The drill-string may impact the borehole. If the radial displacement $r = \sqrt{v^2 + w^2}$ is high enough to exceed the diameter of the borehole, there is a reaction force. This means that there is impact and rubbing if $r > (R_{\text{ch}} - R_o)$, where R_{ch} is the radius of the borehole and R_o is the outer radius of the column, see Fig. 3.6.

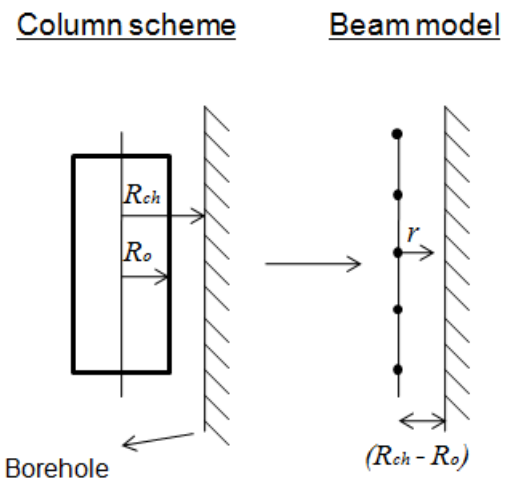

Figure 3.6: Scheme of the radial displacement.

There are several ways to model contact dynamics [40]; in this work, the impact is modeled as an elastic force

$$F_{y\text{ip}} = -\mathbb{1}_{\text{ip}}(r)\; k_{\text{ip}}(r - (R_{\text{ch}} - R_o))\frac{v}{r} \,, \\ F_{z\text{ip}} = -\mathbb{1}_{\text{ip}}(r)\; k_{\text{ip}}(r - (R_{\text{ch}} - R_o))\frac{w}{r} \,, \tag{3-27}$$

where k_{ip} is the stiffness parameter of the impact and $\mathbb{1}_{\text{ip}}(r)$ is an indicator that is equal to one if $r > (R_{\text{ch}} - R_o)$ and is equal to zero otherwise. Rubbing between the column and the borehole is modeled as a frictional torque

$$T_{x\text{ip}} = -\mathbb{1}_{\text{ip}}(r)\ \mu_{\text{ip}} F_n R_o \,\text{sign}(\dot{\theta}_x)\,, \tag{3-28}$$

where $F_n = \sqrt{(F_{y\text{ip}})^2 + (F_{z\text{ip}})^2}$, μ_{ip} is the friction coefficient and $\text{sign}(a)$ returns the sign of a ($\text{sign}(a) = 1$ if $a \geq 0$ and $\text{sign}(a) = -1$ if $a < 0$).

In drilling operations there are stabilizers in the BHA region that help to decrease the amplitude of lateral vibrations. Stabilizers are considered as elastic elements:

$$F_y|_{x=x_{\text{stab}}} = k_{\text{stab}}\ v|_{x=x_{\text{stab}}} \quad \text{and} \quad F_z|_{x=x_{\text{stab}}} = k_{\text{stab}}\ w|_{x=x_{\text{stab}}}\,, \tag{3-29}$$

where x_{stab} is the stabilizer location and k_{stab} is the stabilizer stiffness.

3.1.5 Bit-rock interaction

Figure 3.7 (`http://www.glossary.oilfield.slb.com`) shows two types of bit: the roller cone bit and the polycrystalline diamond compact bit.

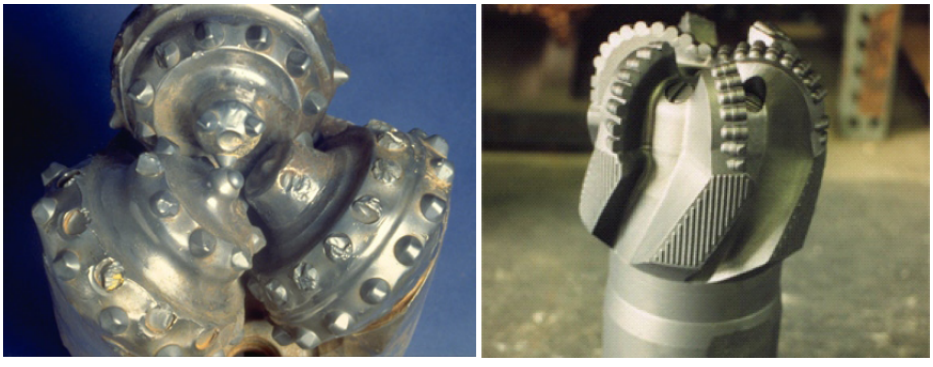

Figure 3.7: Bits. Left: roller cone. Right: polycrystalline diamond compact.

For the bit-rock interaction, the model used is the one developed by [130] (polycrystalline diamond bit) because it describes well how the bit

penetrates the rock. It can be written as

$$\begin{aligned} \dot{u}_{\text{bit}}(t) &= -a_1 - a_2 f_{\text{bit}}(t) + a_3 \omega_{\text{bit}}(t)\,, \\ t_{\text{bit}}(t) &= -\text{DOC}(t)\, a_4 - a_5\,, \\ \text{DOC}(t) &= \frac{\dot{u}_{\text{bit}}(t)}{\omega_{\text{bit}}(t)}\,, \end{aligned} \tag{3-30}$$

where f_{bit} is the axial force (also called weight-on-bit), t_{bit} is the torque about the x-axis and $a_1, \ldots, a_5$ are positive constants that depend on the bit and rock characteristics as well as on the average weight-on-bit. Note that $\dot{u}_{\text{bit}}$ (which is the rate-of-penetration) depends linearly on f_{bit} and on ω_{bit} $(=\dot{\theta}_{\text{bit}})$, and t_{bit} depends linearly on the depth-of-cut (DOC). Note also that these forces couple the axial and torsional vibrations. For convenience, Eq. (3-30) is rewritten as

$$\begin{aligned} f_{\text{bit}}(t) &= -\frac{\dot{u}_{\text{bit}}(t)}{a_2 Z(\omega_{\text{bit}}(t))^2} + \frac{a_3 \omega_{\text{bit}}(t)}{a_2 Z(\omega_{\text{bit}}(t))} - \frac{a_1}{a_2}\,, \\ t_{\text{bit}}(t) &= -\frac{\dot{u}_{\text{bit}}(t) a_4 Z(\omega_{\text{bit}}(t))^2}{\omega_{\text{bit}}(t)} - a_5 Z(\omega_{\text{bit}}(t))\,, \end{aligned} \tag{3-31}$$

where Z is the regularization function:

$$Z(\omega_{\text{bit}}(t)) = \frac{\omega_{\text{bit}}(t)}{\sqrt{(\omega_{\text{bit}}(t))^2 + e^2}}\,, \tag{3-32}$$

and e is the regularization parameter. The regularization function and the torque in function of ω_{bit} are plotted in Fig. 3.8.

The models usually applied for the bit-rock interaction are based on [122], see [24, 101, 55], for instance. In [101, 55] the bit can not move and the torque at the bit is essentially given by:

$$t_{\text{bit}}(t) = \mu_{\text{bit}} f_{\text{bit}} \left[\tanh(\omega_{\text{bit}}(t)) + \frac{\alpha_1 \omega_{\text{bit}}(t)}{1 + \alpha_2 \omega_{\text{bit}}(t)^2} \right]\,, \tag{3-33}$$

where μ_{bit} is a factor that depends on the bit cutting characteristics and α_1, α_2 are constants that depend on the rock properties. Figure 3.9 shows a comparison of the torque at the bit for the models given by Eqs. (3-31) and (3-33). It shows that they are close to each other for $f_{\text{bit}} = -100$ kN (value

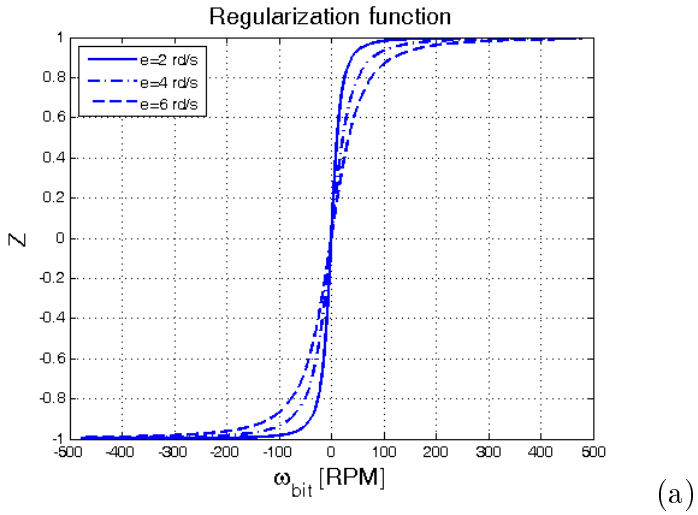

(a)

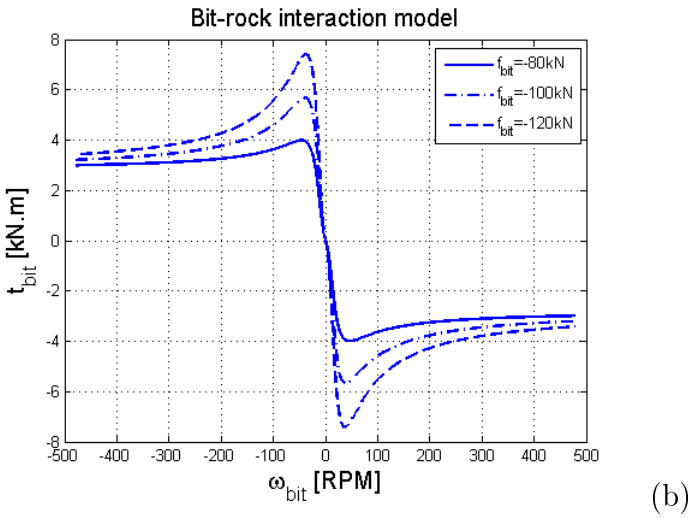

(b)

Figure 3.8: (a) regularization function. (b) torque in function of ω_{bit}.

used in the simulations), $\alpha_1 = \alpha_2 = 1$ and $\mu_{\text{bit}} = 0.04$ (data used in [101]).

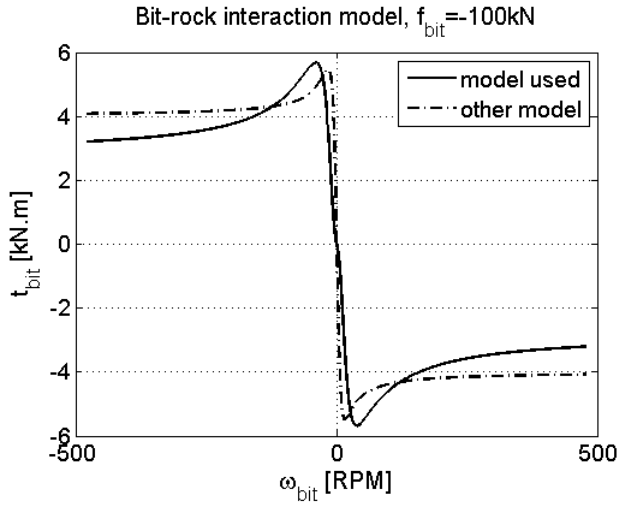

Figure 3.9: Torque at the bit in function of ω_{bit}.

In the next Section the fluid-structure interaction model is developed.

3.2 Fluid-structure interaction

A linear fluid-structure coupling model similar to [80, 81] is used. The proposed simplified model assumes that the pressure varies linearly along x and that the inside flow is inviscid, while the outside flow is viscous. The flow induced by the rotation about the x-axis is not considered in the analysis. Figure 3.10 shows the force balance in a structure-fluid infinitesimal part and Figs. 3.12 and 3.13 show the internal and external flow forces.

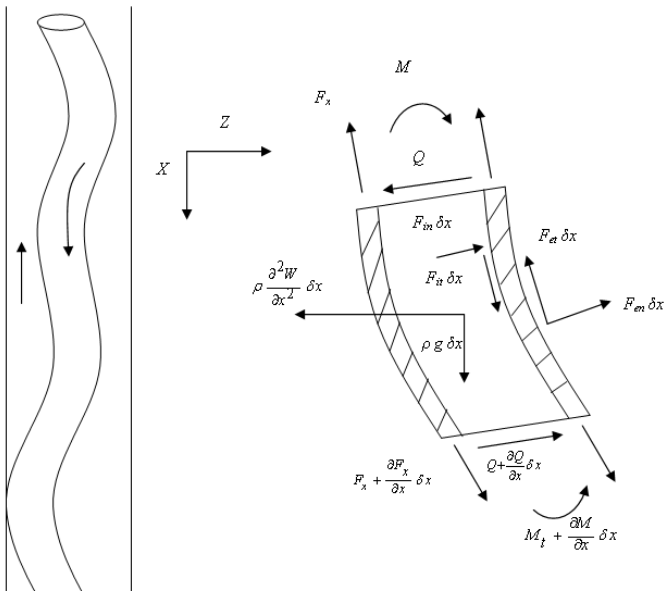

Figure 3.10: Force balance in a structure-fluid infinitesimal part.

Following the strategy presented in [81] and extending the analysis for a 3D problem, we first write the fluid force in x direction, highlighting the forces due to the internal and external flow:

$$F_{x\mathrm{f}} = \underbrace{M_{\mathrm{f}}g - A_i\frac{\partial p_i}{\partial x}}_{internal\,flow}\underbrace{-F^L + \frac{\partial}{\partial x}(A_o p_o) - A_o\frac{\partial p_o}{\partial x}}_{external\,flow}, \tag{3-34}$$

where M_{f} is the mass per unit length, g is the gravity acceleration, A_i and A_o are the cross-sectional areas corresponding to the inner and outer diameters of the column (see Fig. 3.11), ρ_{f} is the fluid density, p_i and p_o are the inside and outside pressures and F_L is a frictional viscous force.

Figures 3.12 and 3.13 shows the internal and external flow forces.

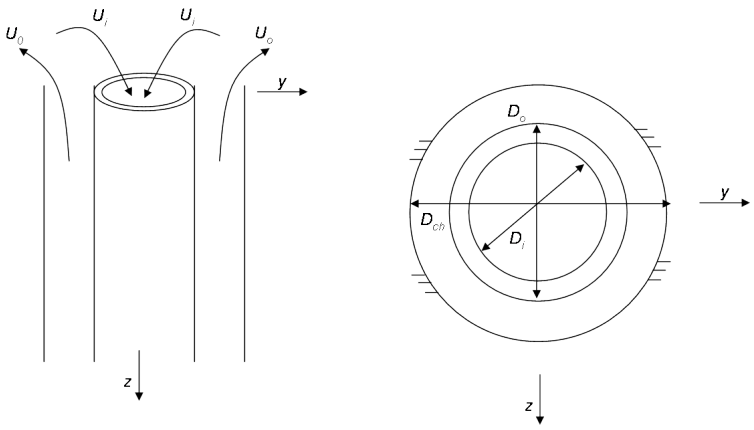

Figure 3.11: Scheme showing the diameters (inside, outside, borehole) and the inlet and outlet flow.

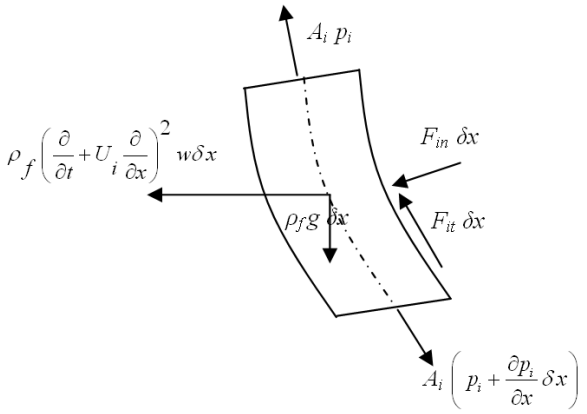

Figure 3.12: Internal flow forces.

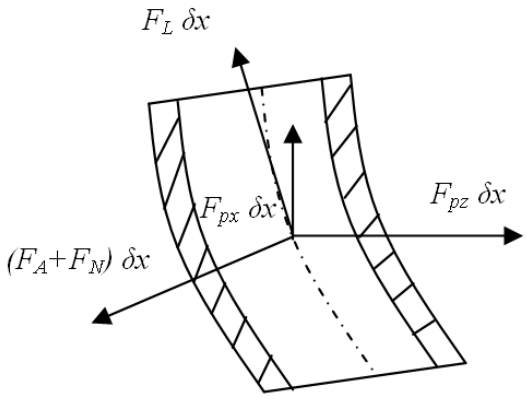

Figure 3.13: External flow forces.

The fluid force in z direction is written as:

$$F_{z\mathrm{f}} = \underbrace{M_{\mathrm{f}}\left(\frac{\partial^2 w}{\partial t^2} + 2U_i\frac{\partial^2 w}{\partial x \partial t} + U_i^2\frac{\partial^2 w}{\partial x^2}\right) + A_i\frac{\partial}{\partial x}\left(p_i\frac{\partial w}{\partial x}\right)}_{internal\,flow} +$$

$$+\underbrace{\chi\left(\frac{\partial}{\partial t} - U_o\frac{\partial}{\partial x}\right)\left[\rho_{\mathrm{f}}A_o\left(\frac{\partial w}{\partial t} - U_o\frac{\partial w}{\partial x}\right)\right] - A_o\frac{\partial}{\partial x}\left(p_o\frac{\partial w}{\partial x}\right) + F_z^N + F^L\frac{\partial w}{\partial x}}_{external\,flow}, \tag{3-35}$$

where U_i and U_o are the flow speed inside and outside the column, $\chi = \frac{(D_{\mathrm{ch}}/D_o)^2+1}{(D_{\mathrm{ch}}/D_o)^2-1}$ which is always > 1 and F_{Nz} is a frictional viscous force. The expressions of the frictional viscous forces are shown below:

$$F^L = \frac{1}{2}C_{\mathrm{f}}\rho_{\mathrm{f}}D_o U_o^2\,, \tag{3-36}$$

$$F_z^N = \frac{1}{2}C_{\mathrm{f}}\rho_{\mathrm{f}}D_o U_o\left(\frac{\partial w}{\partial t} - U_o\frac{\partial w}{\partial x}\right) + k\frac{\partial w}{\partial t}\,, \tag{3-37}$$

where C_{f}, k are the viscous damping coefficients and D_h is the hydraulic diameter $\left(D_h = \frac{4A_{\mathrm{ch}}}{\pi D_{\mathrm{ch}} + \pi D_o}\right)$. The fluid forces in y direction are similar to the ones just presented. As mentioned before, it is assumed that the pressure varies linearly with x:

$$p_i = (\rho_{\mathrm{f}} g)\,x + p_{\mathrm{cte}}\,, \tag{3-38}$$

$$p_o = \left(\rho_{\mathrm{f}} g + \frac{F^L}{A_o}\frac{D_o}{D_h}\right)x\,, \tag{3-39}$$

where p_{cte} is the pump pressure. Another assumption is that there is no head loss when the fluid passes from the drill-pipe to the drill-collar (and vice-versa), see Fig. 3.14.

The head loss due to the change in velocity of the fluid at the bottom

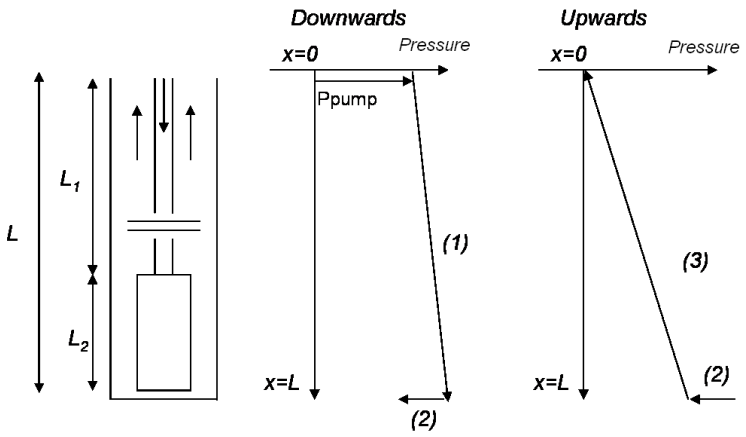

Figure 3.14: Pressure along the x-axis.

(it was going down, then it goes up) is given by

$$h = \frac{1}{2g}(U_i - U_o)^2 \,. \tag{3-40}$$

After discretization by means of the Finite Element Method, the fluid mass element matrix is written as

$$[M_{\mathrm{f}}]^{(e)} = \int_0^1 (M_{\mathrm{f}} + \chi\rho_{\mathrm{f}}A_o)\,(\mathbf{N}_w^T\mathbf{N}_w + \mathbf{N}_v^T\mathbf{N}_v) l_e d\xi \,, \tag{3-41}$$

The fluid mass matrix is the usual added mass. The fluid stiffness element matrix is written as

$$\begin{aligned}[K_{\mathrm{f}}]^{(e)} = &\int_0^1 \left(-M_{\mathrm{f}}U_i^2 - A_i p_i + A_o p_o - \chi\rho_{\mathrm{f}}A_o U_o^2\right)(\mathbf{N}_w'^T\mathbf{N}_w' + \mathbf{N}_v'^T\mathbf{N}_v')\frac{1}{l_e}d\xi + \\ &+ \int_0^1 \left(-A_i\frac{\partial p_i}{\partial x} + A_o\frac{\partial p_o}{\partial x}\right)(\mathbf{N}_{\theta_y}^T\mathbf{N}_{\theta_y} + \mathbf{N}_{\theta_z}^T\mathbf{N}_{\theta_z}) l_e d\xi \,.\end{aligned} \tag{3-42}$$

The fluid stiffness matrix depends on the speed of the inside and outside flow, on the pressure and on the pressure derivatives. The fluid

damping element matrix is written as

$$[C_{\mathrm{f}}]^{(e)} = \int_0^1 \left(-2M_{\mathrm{f}}U_i + 2\chi\rho_{\mathrm{f}}A_oU_o\right)\left(\mathbf{N}_{\theta_y}^T\mathbf{N}_{\theta_y} + \mathbf{N}_{\theta_z}^T\mathbf{N}_{\theta_z}\right)l_e d\xi + \\ + \int_0^1 \left(\frac{1}{2}C_{\mathrm{f}}\rho_{\mathrm{f}}D_oU_o + k\right)\left(\mathbf{N}_w^T\mathbf{N}_w + \mathbf{N}_v^T\mathbf{N}_v\right)l_e d\xi\,. \tag{3-43}$$

The fluid damping matrix depends on the flow speed as well as on the viscous parameters of the fluid which are not well established values. There are uncertainties in the determination of the damping characteristics, but a detailed analysis will not be addressed in the present work. The axial fluid element force is written as

$$(\mathbf{f}_{\mathrm{f}})^{(e)} = \int_0^1 \left(M_{\mathrm{f}}g - A_i\frac{\partial p_i}{\partial x} - \frac{1}{2}C_{\mathrm{f}}\rho_{\mathrm{f}}D_oU_o^2\right)\mathbf{N}_u^T l_e d\xi\,. \tag{3-44}$$

In Section 3.7 we investigate how the dynamical characteristics of the drill-string system change with the inclusion of the fluid-structure interaction model.

3.3 Initial prestressed configuration

Before starting the rotation about the x-axis, the column is put down through the channel until it reaches the soil. At this point the forces acting on the structure are: the reaction force at the bit, the weight of the column, the supporting force at the top and a constant fluid force. In this equilibrium configuration, the column is prestressed (see Fig. 3.15). There is tension above the neutral point and compression below it.
To calculate the initial prestressed state, the column is clamped at the top, and consequently,

$$\mathbf{u}_{\mathrm{S}} = [K]^{-1}(\mathbf{f}_{\mathrm{g}} + \mathbf{f}_c + \mathbf{f}_{\mathrm{f}})\,, \tag{3-45}$$

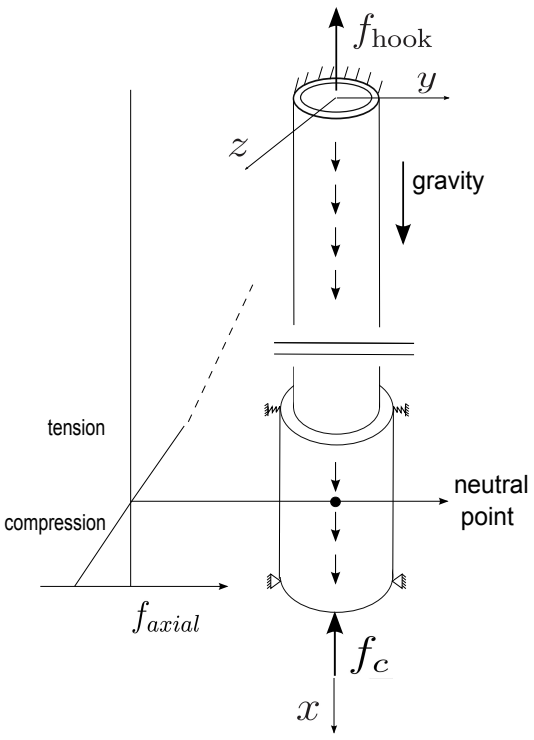

Figure 3.15: Initial prestressed configuration of the system.

where $\mathbf{f}_{\text{g}}$ is the force induced by gravity, $\mathbf{f}_{\text{f}}$ is the fluid axial force and $\mathbf{f}_c$ is the vector related to the reaction force at the bit. Note that $\mathbf{f}_c = [0\ 0 \ldots -f_c\ 0]^T$ in which f_c is the initial reaction force at the bit.

To verify if an element is compressed or tensioned, the element axial displacements of $\mathbf{u}_{\text{S}}$ are checked: $(u_2 - u_1) > 0$ (tensioned), $u_2 = u_1$ (no stress) and $(u_2 - u_1) < 0$ (compressed).

3.4 Boundary and initial conditions

As boundary conditions, the lateral displacements and the rotations about the y and z-axis are zero at the top. At the bit, the lateral displacements are zero. A constant rotational speed about the x-axis Ω_x is imposed at the top. To apply the boundary conditions above, the lines and rows corresponding to the mentioned degrees of freedom are eliminated from the full matrices and the forces corresponding to the imposed rotational speed at the top are considered in the right hand side of the equation.

As initial conditions, all the points move with a constant axial speed and a constant rotational speed about the x-axis, and the column is deflected laterally.

3.5 Discretized system of equations

The vibration takes places around the prestressed configuration, thus $\overline{\mathbf{u}}(t) = \mathbf{u}(t) - \mathbf{u}_{\mathrm{S}}$. The final discretized system of equations are written as

$$
\begin{aligned}
&([M] + [M_{\mathrm{f}}])\ddot{\overline{\mathbf{u}}}(t) + [C]\dot{\overline{\mathbf{u}}}(t) + ([K] + [K_{\mathrm{f}}] + [K_{\mathrm{g}}(\mathbf{u}_{\mathrm{S}})])\overline{\mathbf{u}}(t) = \\
&= \mathbf{g}(t) + \mathbf{f}_{\mathrm{br}}(\dot{\overline{\mathbf{u}}}(t)) + \mathbf{f}_{\mathrm{ip}}(\overline{\mathbf{u}}(t)) - \mathbf{f}_{\mathrm{NL}}(\overline{\mathbf{u}}(t), \dot{\overline{\mathbf{u}}}(t), \ddot{\overline{\mathbf{u}}}(t))\,, \qquad (3\text{-}46) \\
&\overline{\mathbf{u}}(0) = \overline{\mathbf{u}}_0 \quad , \quad \dot{\overline{\mathbf{u}}}(0) = \overline{\mathbf{v}}_0\,,
\end{aligned}
$$

where $\overline{\mathbf{u}}_0$ and $\overline{\mathbf{v}}_0$ are the initial conditions. We identify in Eq. (3-46) the mass and the stiffness matrices of the column $([M], [K])$ and of the fluid $([M_{\mathrm{f}}], [K_{\mathrm{f}}])$. The proportional damping matrix $[C] = \alpha([M]+[M_{\mathrm{f}}])+\beta([K]+[K_{\mathrm{f}}] + [K_{\mathrm{g}}(\mathbf{u}_{\mathrm{S}})])$ (α and β are positive constants) is added *a posteriori* in the computational model; see more details in Section 3.6. The constant α is strictly positive. This yields a positive definite damping matrix, although there are two rigid body modes. Such a damping model is chosen because it is assumed that there is an additional external dissipation when the dynamical system moves in these two rigid body modes. $[K_{\mathrm{g}}(\mathbf{u}_{\mathrm{S}})]$ is the geometric stiffness matrix, $\mathbf{f}_{\mathrm{ip}}$ and $\mathbf{f}_{\mathrm{br}}$ are the impact and bit-rock interaction forces (Eqs. (3-27), (3-28) and (3-31)), and $\mathbf{g}$ is the source force that corresponds to the Dirichlet boundary condition (rotation imposed at the top). The nonlinear force vector $\mathbf{f}_{\mathrm{NL}} = \mathbf{f}_{\mathrm{ke}} + \mathbf{f}_{\mathrm{se}}$, where $\mathbf{f}_{\mathrm{ke}}$ and $\mathbf{f}_{\mathrm{se}}$ are the higher-order terms obtained from the kinetic and strain energies (Eqs. (3-11) and (3-26)).

3.6 Reduced model

Usually the final discretized FE system have high dimensional matrices $(m \times m)$ and the dynamical analysis may be time consuming, which is the case of the present analysis. One way to reduce the system is to project the nonlinear dynamical equation on a subspace V_n, with $n << m$, in which V_n is spanned by a basis of $\mathbb{R}^n$. In the present work, the basis used for the reduction corresponds to the normal modes projection. The normal modes are obtained from the following generalized eigenvalue problem

$$
([K] + [K_{\mathrm{f}}] + [K_{\mathrm{g}}(\mathbf{u}_{\mathrm{S}})])\boldsymbol{\phi} = \omega^2([M] + [M_{\mathrm{f}}])\boldsymbol{\phi}\,, \qquad (3\text{-}47)
$$

where $\boldsymbol{\phi}_i$ is the i-th normal mode and ω_i is the i-th natural frequency. Since initially the column is prestressed, we should compute the normal modes in this prestressed state. Matrices $[K]$ and $[K_\mathrm{f}]$ are positive semi-definite. The geometrical stiffness matrix $[K_\mathrm{g}(\mathbf{u})]$ is not always positive semi-definite, but when $\mathbf{u} = \mathbf{u}_\mathrm{S}$, then $[K_\mathrm{g}(\mathbf{u}_\mathrm{S})]$ is positive semi-definite. Therefore, the sum $([K] + [K_\mathrm{f}] + [K_\mathrm{g}(\mathbf{u}_\mathrm{S})])$ is positive semi-definite. Matrices $[M]$ and $[M_\mathrm{f}]$ are positive-definite, consequently, the sum $([M] + [M_\mathrm{f}])$ is positive-definite.

The following representation is used

$$\overline{\mathbf{u}} = [\Phi]\,\mathbf{q}\,, \tag{3-48}$$

where $[\Phi]$ is a $(m \times n)$ real matrix composed by n normal modes. The normal modes that compose matrix $[\Phi]$ must be conveniently chosen (so that axial, lateral and torsional modes are included) in order that the convergence of the response is reached. We substitute $\overline{\mathbf{u}} = [\Phi]\,\mathbf{q}$ in Eq. (3-46) and project this equation on the subspace spanned by these normal modes yielding

$$\begin{aligned} &[M_r]\ddot{\overline{\mathbf{q}}}(t) + [C_r]\dot{\mathbf{q}}(t) + [K_r]\dot{\mathbf{q}}(t) = \mathbf{f}_r(t, \overline{\mathbf{q}}(t), \dot{\overline{\mathbf{q}}}(t), \ddot{\overline{\mathbf{q}}}(t)) \\ &\mathbf{q}(0) = \mathbf{q}_0 \quad , \quad \dot{\mathbf{q}}(0) = \mathbf{v}_0\,, \end{aligned} \tag{3-49}$$

where $\mathbf{q}_0$ and $\mathbf{v}_0$ are the initial conditions and

$$\begin{aligned} &[M_r] = [\Phi]^T([M] + [M_\mathrm{f}])[\Phi], \quad [C_r] = [\Phi]^T[C][\Phi]\,, \\ &[K_r] = [\Phi]^T([K] + [K_\mathrm{f}] + [K_\mathrm{g}(\mathbf{u}_\mathrm{S})])[\Phi]\,, \\ &\mathbf{f}_r(t, \overline{\mathbf{q}}(t), \dot{\overline{\mathbf{q}}}(t), \ddot{\overline{\mathbf{q}}}(t)) = [\Phi]^T(\mathbf{g}(t) + \mathbf{f}_\mathrm{br}(\dot{\overline{\mathbf{u}}}(t)) + \mathbf{f}_\mathrm{ip}(\overline{\mathbf{u}}(t)) - \mathbf{f}_\mathrm{NL}(\overline{\mathbf{u}}(t), \dot{\overline{\mathbf{u}}}(t), \ddot{\overline{\mathbf{u}}}(t))) \end{aligned} \tag{3-50}$$

are the reduced matrices and the reduced force vector. The proportional damping matrix $[C] = \alpha([M] + [M_\mathrm{f}]) + \beta([K] + [K_\mathrm{f}] + [K_\mathrm{g}(\mathbf{u}_\mathrm{S})])$ is added *a posteriori*, so that:

$$[C_r]_{ij} = 2\omega_i \xi_j \delta_{ij}\,, \tag{3-51}$$

where ξ_j is the j-th damping ratio, and $\delta_{ij} = 1$ if $i = j$ and $\delta_{ij} = 0$ otherwise.

Now, the constants α and β can be adjusted in a way that $\xi \sim 10\%$, or any identified value.

Appendix D presents the time integration scheme used in the numerical simulations.

3.7 Numerical results

In the first part of this Section, the influence of the fluid on the drill-string dynamics is investigated using a numerical example and, in the end of this Section, some simulations are performed varying some parameters, such as the material and the length of the column. The data used for the numerical simulations of the system are representative values that are found in the literature [48, 24, 130, 55, 101] (see Appendix F).

3.7.1 Modal analysis

The elastic modes of the structure (lateral, axial and torsional) and the associated natural frequencies are analyzed in this Section. This analysis is essential to understand how the characteristics of the system are affected by the fluid flow.

To correctly compare the normal modes and the corresponding natural frequencies for two different cases, the matrix [MAC] [4] defined by

$$[\mathrm{MAC}]_{ij} = \frac{< \boldsymbol{\Phi}_i^1, \boldsymbol{\Phi}_j^2 >}{||\boldsymbol{\Phi}_i^1||.||\boldsymbol{\Phi}_j^2||} \tag{3-52}$$

is used, where $\boldsymbol{\Phi}_i^1$ is the i-th mode for the first case, $\boldsymbol{\Phi}_j^2$ is the j-th mode for the second case, $< \cdot, \cdot >$ denotes the Euclidean inner product and $|| \cdot ||$ is the associated norm. Two modes $\boldsymbol{\Phi}_i^1$ $\boldsymbol{\Phi}_j^2$ are well associated if $[\mathrm{MAC}]_{ij}$ has value close to one and they are not well associated if this value is close to zero.

First, the influence of the prestressed configuration is analyzed and no fluid is considered yet. Table 3.1 shows the natural frequencies associated with the first 10 lateral modes of the system with and without the prestressed configuration. For short, we call them lateral natural frequencies and it is implicit that they are the natural frequencies associated with the lateral modes.

Rank of the eigenvalue (prestressed config.)	1-2	3-4	5-6	7-8	9-10
prestressed (Hz)	0.0287	0.0464	0.0928	0.1098	0.1394
no prestress (Hz)	0.0127	0.0004	0.0010	0.0490	0.0020
difference (%)	55.7	99.1	98.9	55.4	98.6

Table 3.1: Lateral natural frequencies with and without the prestressed configuration (no fluid).

The lateral natural frequencies appear in pairs due to the symmetry about the x-axis (and the modes associated to the same frequency have the same shape). The values of the natural frequencies change completely (with differences greater than 50%) when the prestressed state is considered. The first lateral shape for the model considering the prestressed state is associated with the ninth lateral shape for the model without the prestressed state, the second one is associated with the first one, the third one is associated with the second one, the forth is associated with the eighteenth one and so on. Sometimes the shapes are well related ($[\mathrm{MAC}]_{ij} \sim 1$) and sometimes the correlation is not so good ($[\mathrm{MAC}]_{ij} < 0.5$).

Tables 3.2 and 3.3 show the differences of the axial and torsional natural frequencies comparing the column with and without the prestressed configuration.

Rank of the axial eigenvalue (prestressed config.)	1	2	3	4	5
prestressed (Hz)	1.202	2.882	4.676	6.503	8.343
no prestress (Hz)	1.201	2.879	4.672	6.496	8.336
difference (%)	0.092	0.094	0.094	0.095	0.095

Table 3.2: Axial natural frequencies with and without the prestressed configuration (no fluid).

Rank of the torsional eigenvalue (prestressed config.)	1	2	3	4	5
prestressed (Hz)	0.2144	1.1105	2.1526	3.2138	4.2850
no prestress (Hz)	0.2141	1.1094	2.1505	3.2107	4.2809
difference (%)	0.1401	0.0992	0.0977	0.0966	0.0958

Table 3.3: Torsional natural frequencies with and without the prestressed configuration (no fluid).

The axial and torsional natural frequencies not affected considerably by the prestressed configuration. The analyzed modes are always well related ($[\mathrm{MAC}]_{ij} \sim 1$).

Now the influence of the fluid is analyzed, always using the prestressed configuration. It should be remarked that the inclusion of the fluid does not change the axial and torsional natural frequencies of the system as it can be checked from Eqs. (3-41), (3-42) and (3-43).

Figure 3.16 shows the comparison of the mode shapes for the model with and without the fluid.

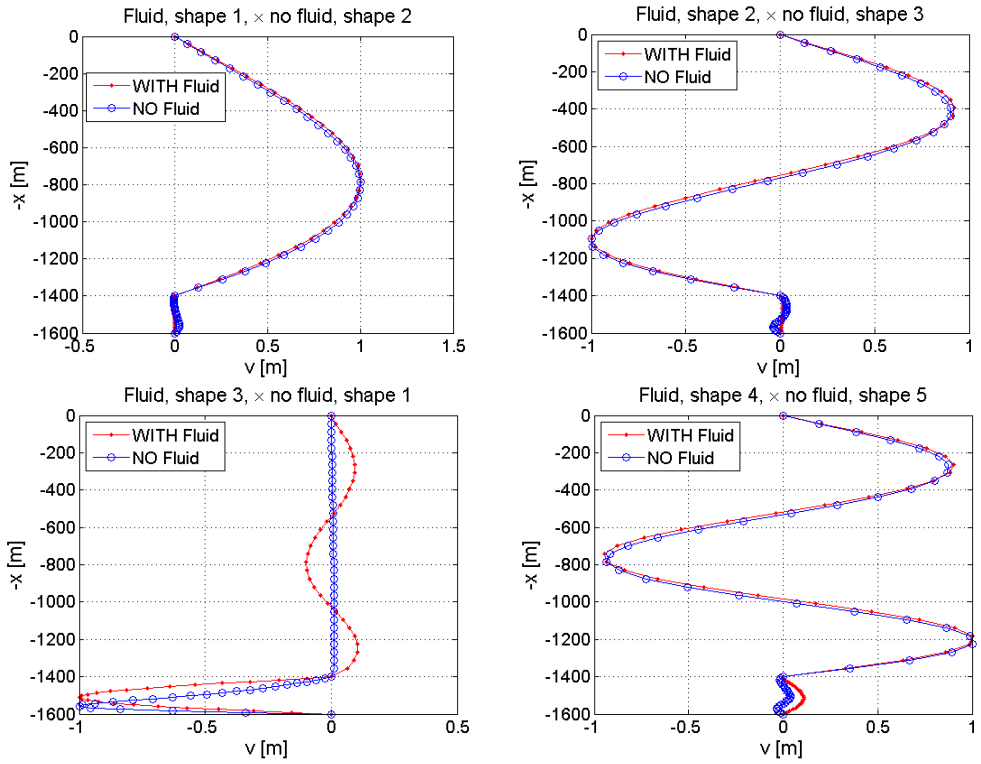

Figure 3.16: Comparison of the lateral modes for the model with and without fluid.

As shown in Fig. 3.16, the first lateral shape for the model with fluid is associated with the second lateral shape for the model without fluid, the second one is associated with the third one, the third one is associated with the first one, the fourth one is associated with the fifth one and so on. Table 3.4 shows a comparison of the lateral natural frequencies.

Rank of the eigenvalue (config. with fluid)	1-2	3-4	5-6	7-8	9-10
with fluid (Hz)	0.037	0.074	0.107	0.112	0.145
no fluid (Hz)	0.046	0.093	0.029	0.139	0.186
difference (%)	-24.7	-24.7	73.1	-24.8	-24.8

Table 3.4: Lateral natural frequencies for the model with and without the fluid.

There is a significant change in the lateral frequencies due to the presence of the fluid. Investigating the influence of each term of the fluid equations, it was found that the term $(-p_i A_i + p_o A_o)$ of the fluid stiffness matrix has a major influence on the stiffness of the system. Note that $p_i \sim p_o$ for a given depth, but in the lower region (BHA) $A_o \sim 10 A_i$, which makes the system much stiffer in the bottom. Table 3.4 shows that the lateral natural frequencies for the model with fluid might be lower or greater than the lateral natural frequencies for the model without fluid when comparing with respect to the associated modes.

Next, it will be investigated the influence of the added mass and added stiffness separately. The influence of the damping depends on the viscous property of the fluid, but it is not analyzed in the present work. Table 3.5 shows the differences of the lateral natural frequencies for the added mass only and for the added stiffness only.

Rank of the eigenvalue (config. without fluid)	1-2	3-4	5-6	7-8	9-10
no fluid (Hz)	0.029	0.046	0.093	0.110	0.140
added mass only (Hz)	0.023	0.036	0.072	0.087	0.108
difference (%)	-20.7	-22.8	-22.8	-20.7	-22.8
no fluid (Hz)	0.029	0.046	0.093	0.110	0.140
added stiffness only (Hz)	0.134	0.048	0.096	0.273	0.145
difference (%)	367.9	3.7	3.8	148.2	3.7

Table 3.5: Influence of the added fluid mass and stiffness on the lateral frequencies.

The presence of the fluid adds around 50% of mass, this is why the natural frequencies are around 20% lower. It should be noted that the shapes of the lateral modes practically do not change when only the fluid mass is considered. The changes in the mode shapes occur mainly due to the fluid added stiffness. The first lateral shape for the model without fluid is associated with the third lateral shape for the model with added fluid stiffness, the second one is associated with the first one, the third one is associated with the second one, the fourth one is associated with the seventh one and so on.

Now, the influence of the inside and outside flow are investigated separately. Table 3.6 shows the differences of the lateral natural frequencies for the inside flow only and for the outside flow only.

The inside flow makes the system less stiff and unstable: the first eigenvalue is imaginary, indicating that the system is unstable. The outside

Rank of the eigenvalue (config. without fluid)	1-2	3-4	5-6	7-8	9-10
no fluid (Hz)	0.029	0.046	0.093	0.110	0.140
inside flow (Hz)	$0.080\sqrt{-1}$	0.040	0.080	0.064	0.121
difference (%)	-	-13.6	-13.4	-42.0	-13.5
no fluid (Hz)	0.029	0.046	0.093	0.110	0.140
outside flow (Hz)	0.113	0.041	0.082	0.228	0.124
difference (%)	292.3	-11.2	-11.2	107.7	-11.3

Table 3.6: Influence of the added fluid mass and stiffness on the lateral frequencies.

flow increases the eigenfrequencies associated with some lateral modes and decreases others.

Finally, Table 3.7 shows the difference in the lateral natural frequencies when the flow speed is increased. It is noted that the flow speed is not so important to change significantly the dynamic characteristics of the structure.

Rank of the eigenvalue	1-2	3-4	5-6	7-8	9-10
U_i=1.5 m s^{-1} (Hz)	0.0372	0.0744	0.1065	0.1117	0.1488
U_i=10 m s^{-1} (Hz)	0.0368	0.0736	0.1066	0.1106	0.1473
difference (%)	1.0753	1.0753	-0.0939	0.9848	1.0081

Table 3.7: Influence of the flow on the lateral frequencies.

3.7.2 Dynamical response

The column was discretized with 56 finite elements. For the time integration, the Newmark scheme was used together with an iteration method (fixed point) to solve the nonlinear algebraic equation (Eq. 3-46) at each time step ($\Delta t = 5 \times 10^{-5}$). As initial conditions, all the points of the column have a given axial speed $\overline{v}_0$ (4.2×10^{-3} m s^{-1}), a given rotational speed about the x-axis ω_{x0} (0.83 Hz) and the column is deflected laterally. For the construction of the reduced dynamical model, 158 lateral modes, 4 torsional modes, 3 axial modes and also the two rigid body modes of the structure (axial and torsional) are used. The columns of matrix $[\Phi]$ are made up of 167 modes. The number 167 was chosen after several numerical experiments in order to get convergence (see Appendix E). The nonzero eigenfrequencies of the linearized system around the prestressed configuration (see Eq. 3-47) are given in Table 3.8. The lateral eigenfrequencies appear in pairs due to the symmetry about the x-axis.

Rank	Eigenfrequency	Type
1-2	0.0372 Hz	Lateral
3-4	0.0744 Hz	Lateral
5-6	0.1065 Hz	Lateral
7-8	0.1117 Hz	Lateral
9-10	0.1488 Hz	Lateral
11-12	0.1860 Hz	Lateral
13	0.2144 Hz	Torsional
14-15	0.2160 Hz	Lateral
16-17	0.2234 Hz	Lateral
18-19	0.2605 Hz	Lateral
...	...	...
76	1.1105 Hz	Torsional
...	...	...
81	1.2018 Hz	Axial
...	...	...
163-164	3.2671 Hz	Lateral
165	4.6761 Hz	Axial

Table 3.8: Eigenfrequencies of the linearized system.

The dynamical system is excited by a constant rotational speed about the x-axis at the top and with value 0.83 Hz (=50 RPM). Note that for such an excitation (no lateral source forces), if there is no bit-rock interaction and no initial displacement in the lateral direction, there is no vibration in the forced response for the linearized system (there is only a rigid body displacement in rotation). In the presence of the nonlinear bit-rock interaction and without initial displacement in the lateral direction, the forced response does not exhibit lateral vibration and there are only coupled torsional and axial vibrations with a broad frequency spectrum. The results presented below correspond to the case with the nonlinear bit-rock interaction and an initial displacement in the lateral direction. Consequently, the forced response exhibits coupled torsional, axial and lateral vibrations on a broad band frequency spectrum. In fact, due to the nonlinearities induced by the bit-rock interactions forces and by the geometrical nonlinearities the frequency spectrum exhibits responses on a broad band for all components of the displacements.

The results presented are the time response and the frequency spectrum defined as the modulus of its Fourier transform. Fig. 3.17 shows the radial response ($r = \sqrt{v^2 + w^2}$) at two points: $x = 700$ m and $x = 1520$ m. Figure 3.17(a) shows the dynamical response of the middle point of the drill-pipe region (the upper part) which is the point that presents the

maximum radial displacement. The amplitude of the displacement begins small and then it increases until a certain value. The opposite happens for the radial displacement in the BHA region (the bottom part): the amplitude of the displacement decreases until a certain value, see Fig. 3.17(b). There is an exchange of energy between the modes, then the radial displacement gets higher in the less stiff region (the drill-pipe region). If the nonlinearities that come from the kinetic and strain energies were neglected ($\mathbf{f}_{\text{se}} = \mathbf{f}_{\text{ke}} = 0$), the amplitude of the lateral displacement would vanish, since there would be no coupling between the lateral with the axial and torsional vibrations. All of these effects happen due to the vibration coupling induced by these nonlinearities.

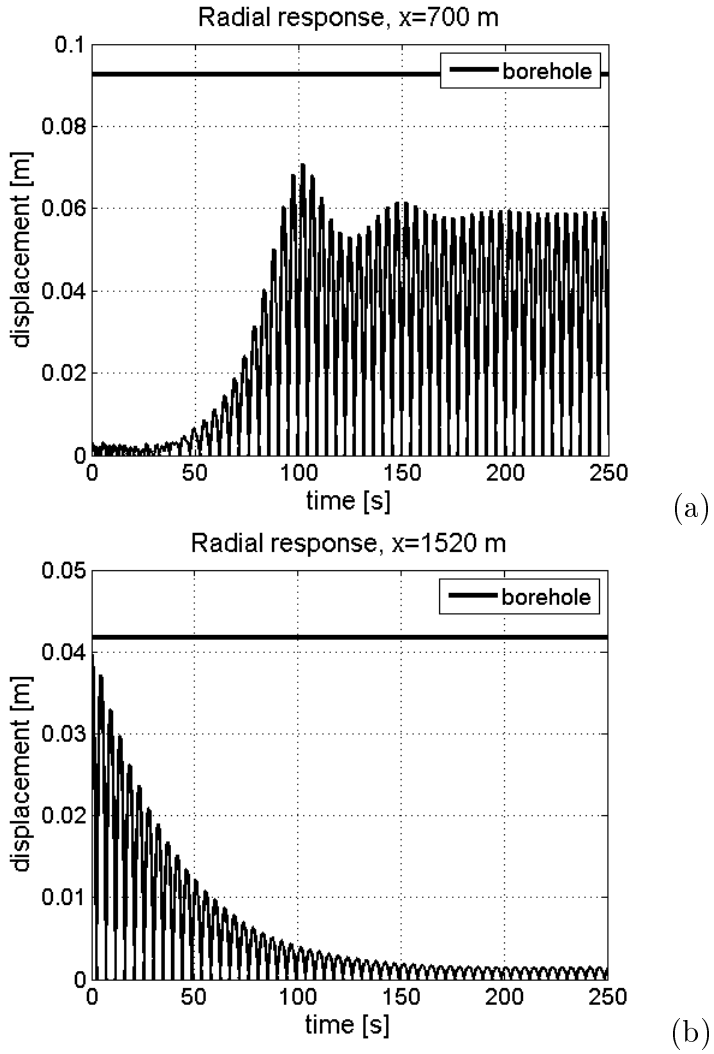

Figure 3.17: Radial response at $x = 700$ m (a) and $x = 1520$ m (b). Note that the distance between the column and the borehole is different depending on the region of the column considered.

For the next analysis the response is considered for $t > t^t$. Time t^t

was identified such that after $t = t^t$ the transient part vanishes, so that for $t \in [t^t, t[$ there is only the forced response. Figure 3.18(a) shows the axial speed at $x = 700$ m and Fig. 3.18(b) shows its frequency spectrum. The fundamental frequency 0.220 Hz is a little higher than the first torsional natural frequency which is 0.214 Hz. The fundamental frequency corresponds to the self-excited vibration of the system that is related to the torsional vibration imposed by the bit-rock interaction. Due to the nonlinearities of the system, the multiples $0.220 \times i$ (with $i = 1, 2, ..$) of the fundamental frequency appear in the frequency spectrum.

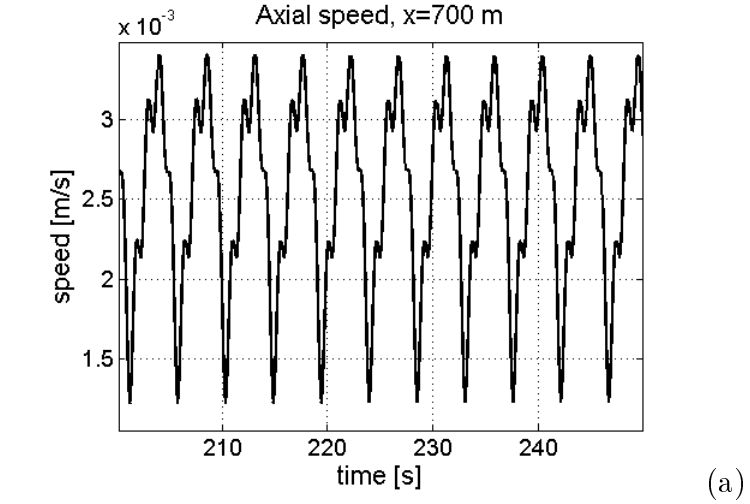

(a)

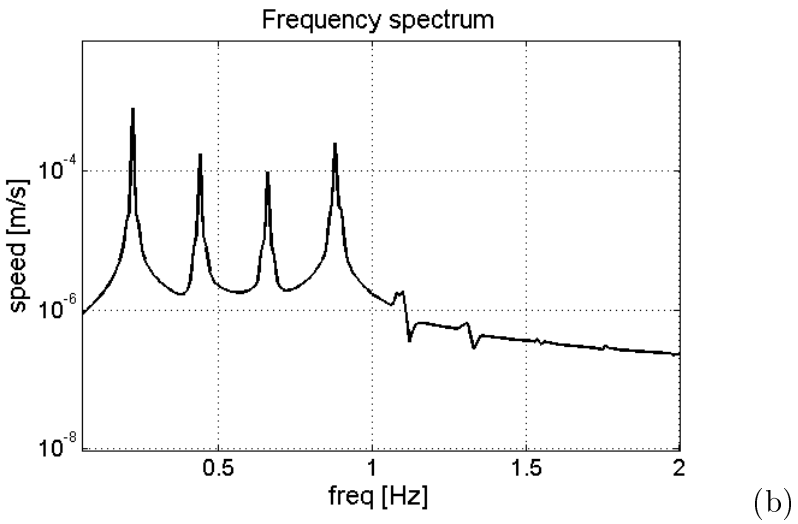

(b)

Figure 3.18: Response at $x = 700$ m. Axial speed (a) and frequency spectrum (b).

Figure 3.19(a) shows the rotational speed about the x-axis at $x = 700$ m and Fig. 3.19(b) shows its frequency spectrum. The bit-rock interaction acts on the axial speed and on the rotational speed about the x-axis, therefore the same kind of frequency spectrum is observed for the rotational speed about the x-axis and for the axial speed.

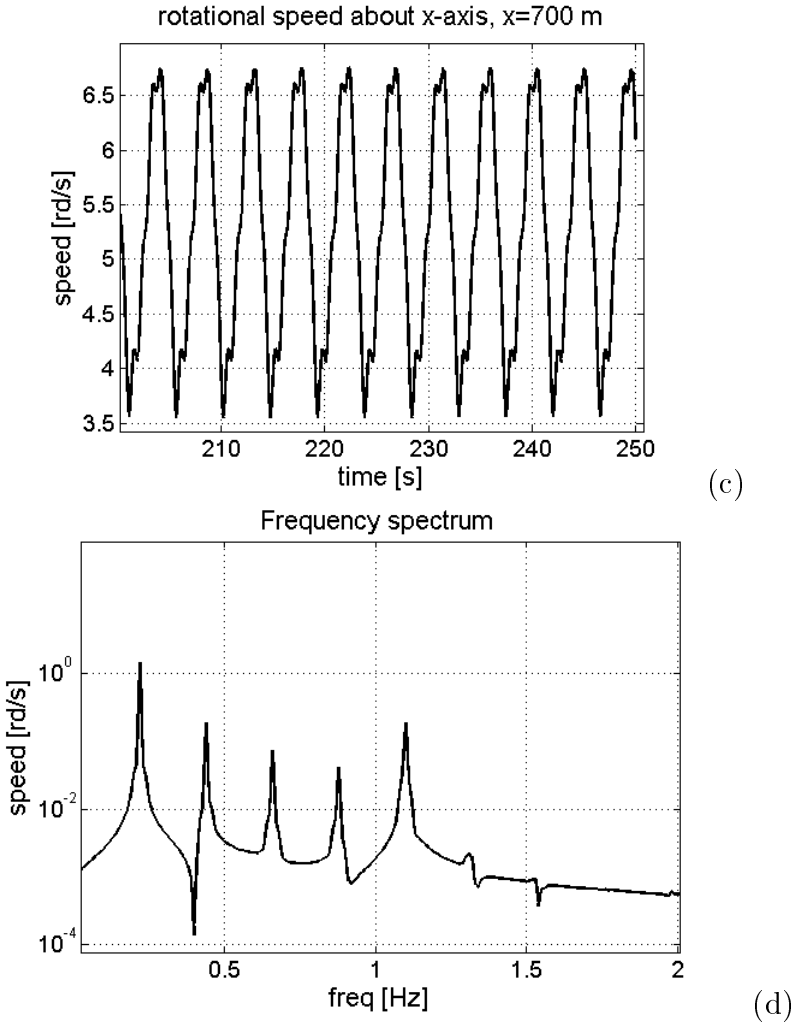

Figure 3.19: Response at $x = 700$ m. Rotational speed about the x-axis (a) and frequency spectrum (b).

Figure 3.20(a) shows the rotation about the z-axis and Fig. 3.20(b) shows its frequency spectrum. The dominant frequency, 0.110 Hz, is equal to the half of the fundamental frequency related to the self excited vibration. The frequency spectrum shows the multiples $0.110 \times i$ (with $i = 1, 3, 5, ..$). The same behavior is observed for the lateral response v, Figs. 3.21(a) and (b).

Next, the dynamical response for the model with and without the fluid are compared. Figure 3.22 shows the radial response for $t = [0, 250]$s at $x = 1560$ m.

Figure 3.23 shows the forced response of the radial displacement at $x = 700$m. The displacement is shown in log-scale. The radial response increases when the fluid is considered in the model. This might be explained by the shape of the first lateral modes: when the fluid is considered, the upper region is more flexible than the bottom region (see the mode shapes

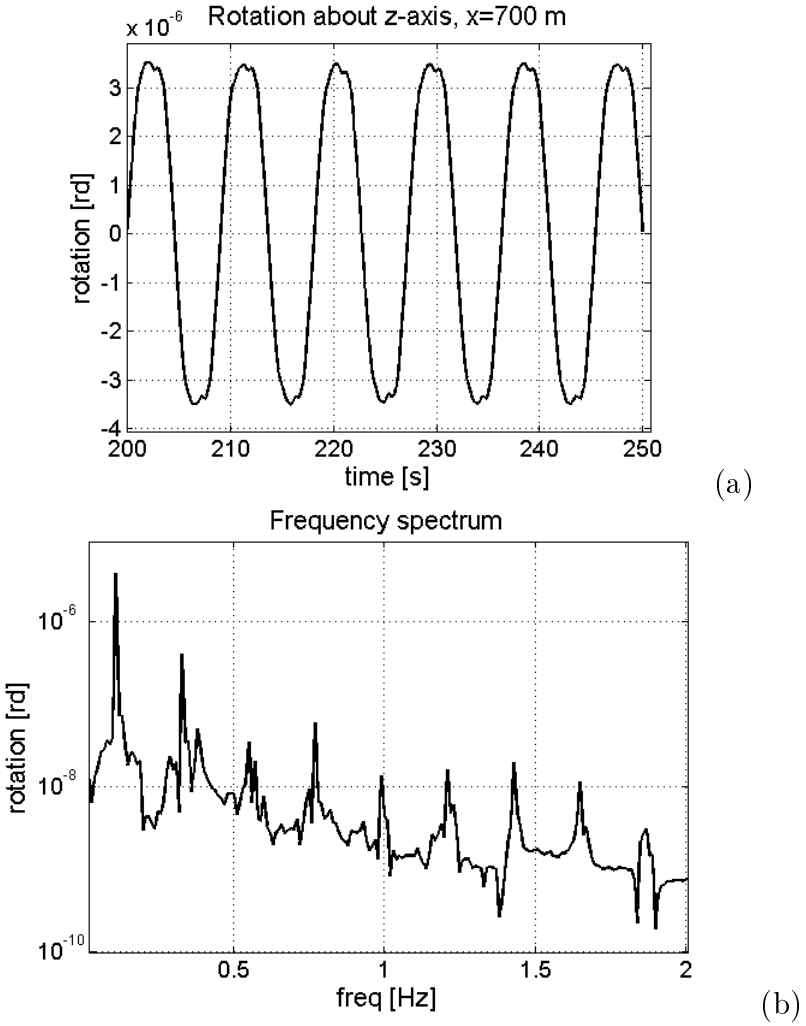

Figure 3.20: Response at $x = 700$ m. Rotation about the z-axis (a) and frequency spectrum (b).

in Fig. 3.16), so the amplitude of vibration increases in the upper region. It can be observed in Fig. 3.23 that the self excited frequency is dominating the movement of both dynamics.

The axial and torsional vibrations are also affected by the presence of the fluid: the fundamental (self excited) frequency changes when the fluid is taken into account. Figure 3.24(a) and (b) shows the axial speed of the bit (or rate-of-penetration) and its frequency spectrum. When the fluid is not taken into account, the fundamental frequency 0.210 Hz is a little lower than the first torsional natural frequency which is 0.214 Hz.

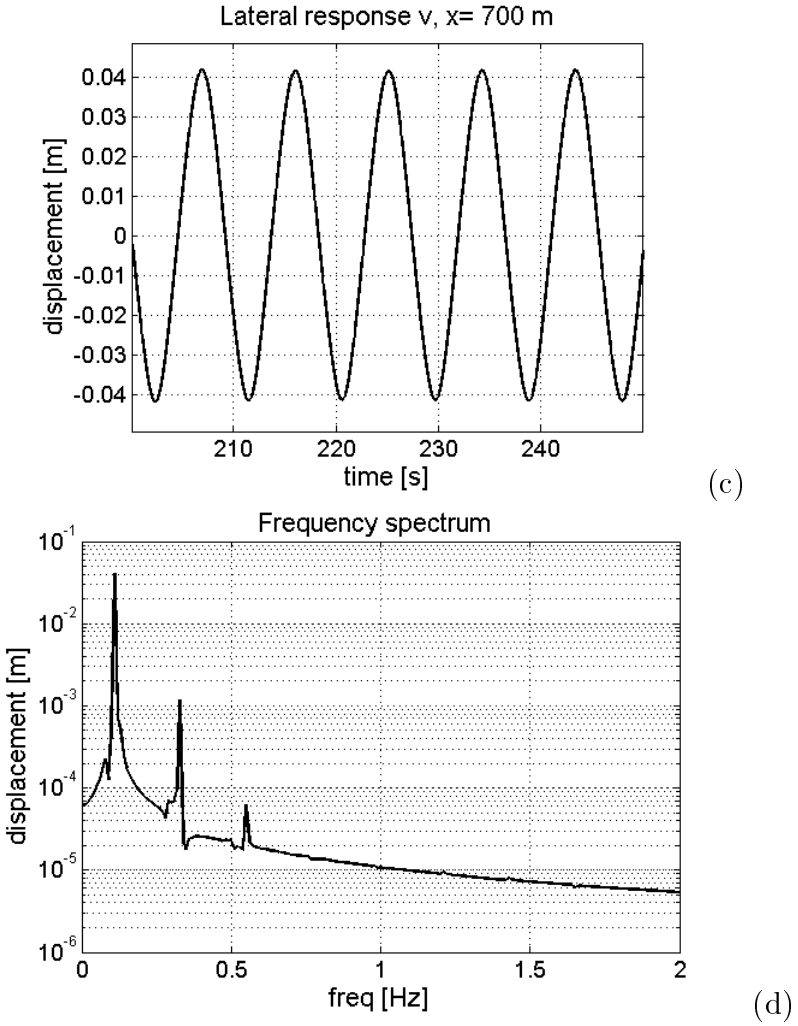

Figure 3.21: Response at $x = 700$ m. Lateral displacement v (a) and frequency spectrum (b).

3.7.3 Some investigations

In this Section, the nonlinear dynamics of the drill-string is analyzed varying some parameters.

Figure 3.25 shows the dynamical results for columns with different lengths. Only the drill-pipe length is varied for the different simulations (the length of the drill-collar and the diameters of the column are kept the same). Five lengths are considered $L_{\rm dp} = \{500, 1400, 1800, 2800, 3800\}$ m. Figure 3.25(a) shows how the dimensionless ROP (mean(ROP)/ROP$_{\rm ref}$) varies with the dimensionless parameter $D_{o\rm dp}/L_{\rm dp}$, where mean(ROP) is the time average (see Eq. (3-53)) and ROP$_{\rm ref}$=10 m/h.

$$\text{mean}(\dot{u}_{\rm bit}(t)) = \frac{1}{n_t}\sum_{i=1}^{n_t} \dot{u}_{\rm bit}(t_i)\,. \tag{3-53}$$

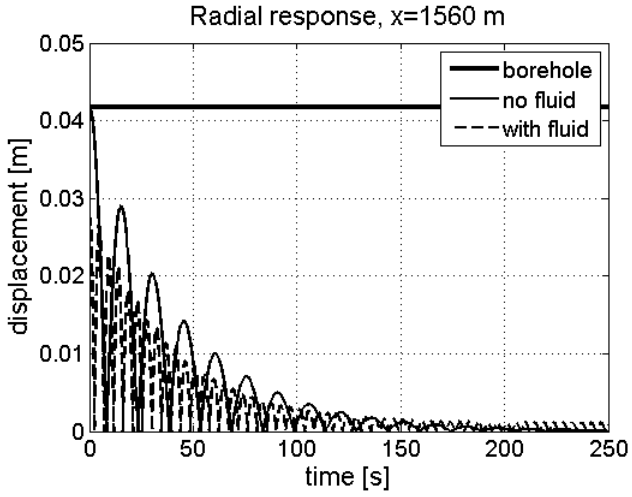

Figure 3.22: Comparison of the dynamical response for model with and without fluid. Radial response at $x = 1560$ m.

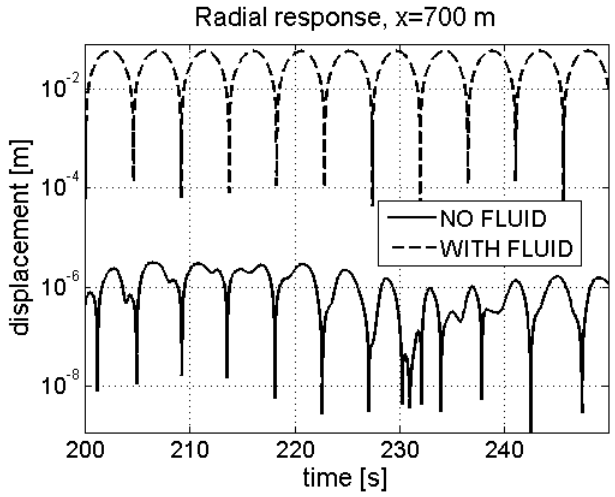

Figure 3.23: Comparison of the dynamical response for model with and without fluid. Radial response at $x = 700$ m.

where n_t are the number of instants. The quantity $D_{o\mathrm{dp}}/L_{\mathrm{dp}}$ represents a measure of the drill-string stiffness; the column gets stiffer as this quantity increases. The dimensionless ROP assumes different values for different values of $D_{o\mathrm{dp}}/L_{\mathrm{dp}}$. For the points analyzed, $D_{o\mathrm{dp}}/L_{\mathrm{dp}} = 5.3 \times 10^{-5}$ presented the maximum dimensionless ROP=0.917, but the differences are lower than 2%. Figure 3.25(b) shows the frequency spectrum of the dimensionless ω_{bit} (rotational speed of the bit), which is given by $\omega_{\mathrm{bit}}/\mathrm{mean}(\omega_{\mathrm{bit}})$. It can be noticed that the fundamental frequency increases when the value of $D_{o\mathrm{dp}}/L_{\mathrm{dp}}$ increases, which can be explained by the fact

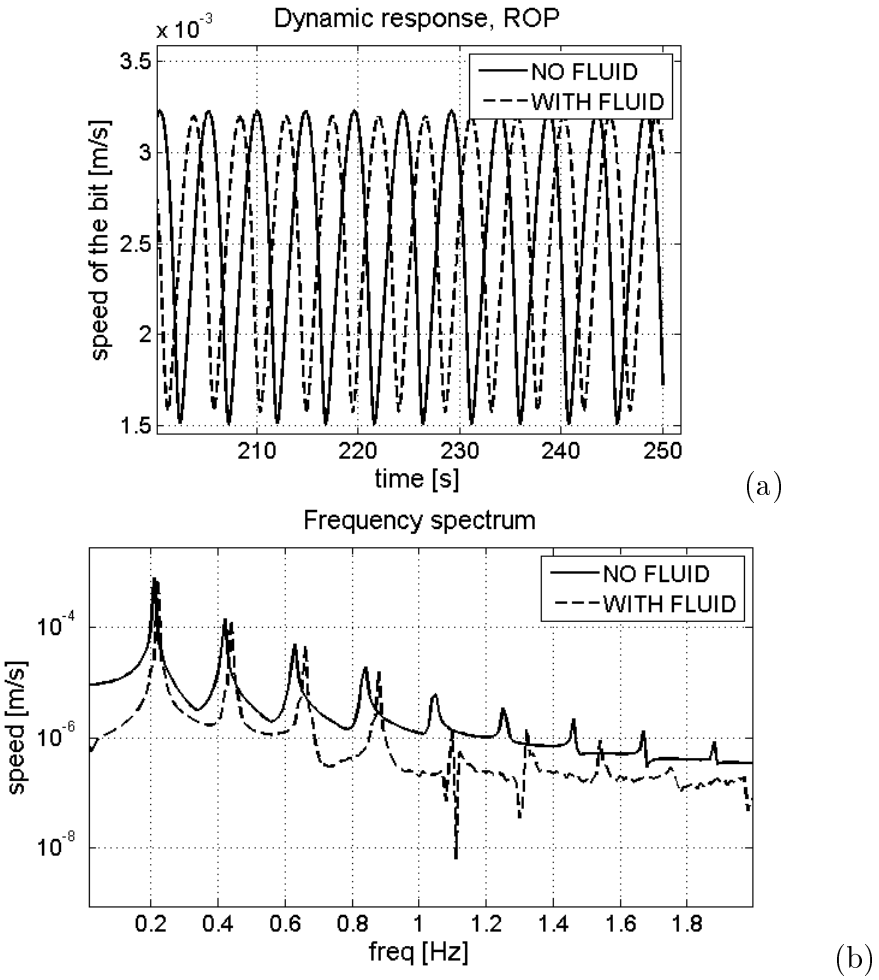

Figure 3.24: Comparison of the dynamical response for model with and without fluid. Rate-of-penetration (ROP) (a) and frequency spectrum (b).

that the system gets stiffer when D_{odp}/L_{dp} increases.

Figure 3.26 shows the dynamical results for columns with different materials, which are shown in table 3.9. Figure 3.26(a) shows how the dimensionless ROP varies with the dimensionless density (ρ/ρ_{steel}), where ρ_{steel} is the steel density. The quantity ρ/ρ_{steel} represents how dense the column is. For the three materials analyzed, the dimensionless ROP increases when ρ/ρ_{steel} increases. However, this is a very limited analysis because we are keeping all the other parameters the same, including the parameters of the bit-rock interaction model. Figure 3.26(b) shows the frequency spectrum of the dimensionless ω_{bit}, and it can be noticed that the fundamental frequency changes depending on the material of the column.

Figure 3.27 shows the dynamical results for columns with different torques at the bit. The torque at the bit t_{bit} (see Eq. 3-31) is multiplied by 4 and then by 8. Figure 3.27(a) shows how the dimensionless ROP varies with the dimensionless parameter t_{bit}/t_{bitREF}, where t_{bitREF} is the

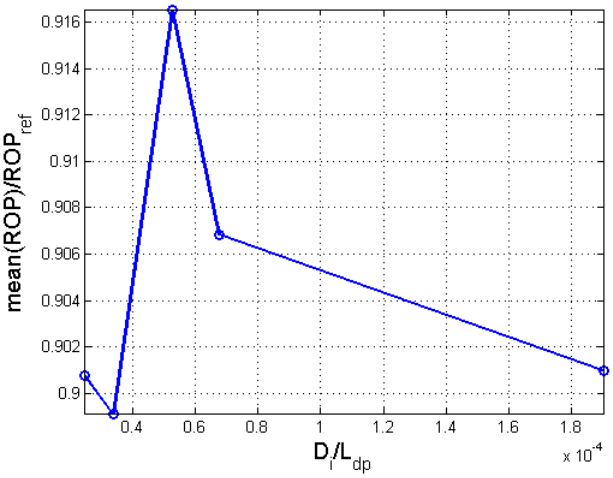

(a)

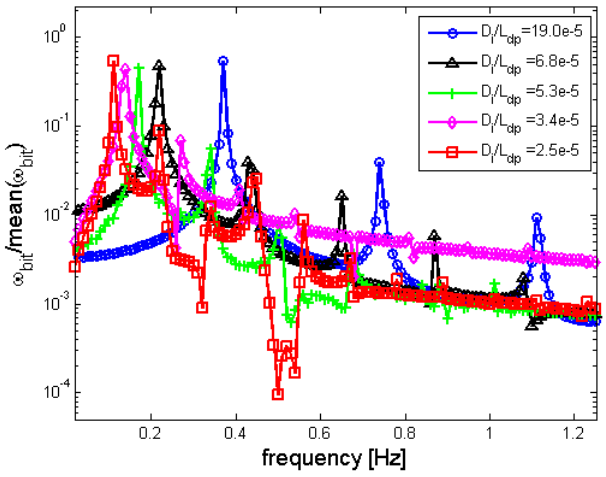

(b)

Figure 3.25: Results for different column lengths (a) dimensionless ROP and (b) frequency response of the dimensionless rotational speed of the bit

mean torque at the bit of the original simulation. The quantity $t_{\mathrm{bit}}/t_{\mathrm{bitREF}}$ represents a measure of the friction between the bit and the rock; if the friction gets higher this quantity increases. The dimensionless ROP decreases when $t_{\mathrm{bit}}/t_{\mathrm{bitREF}}$ increases, which means that if the friction is high it is more difficult to drill. Figure 3.27(b) shows the frequency spectrum of the dimensionless ω_{bit} . It can be noticed that the fundamental frequency decreases when the value of $t_{\mathrm{bit}}/t_{\mathrm{bitREF}}$ increases, which means that the movement is slower when the friction coefficient is higher.

Figure 3.28 shows the dynamical results for columns with different borehole diameters (D_{ch}), which are $D_{\mathrm{ch}} = \{250;\ 270;\ 312\}$ mm. Figure 3.28(a) shows how the dimensionless ROP varies with the dimensionless parameter $D_{\mathrm{o}}/D_{\mathrm{ch}}$. Note that if $D_{\mathrm{o}}/D_{\mathrm{ch}}$=1 there is no annulus. The dimensionless ROP assumes different values for different values of $D_{\mathrm{o}}/D_{\mathrm{ch}}$.

	Steel	Aluminium	Kevlar
Elasticity Modulus (GPa)	$E_{\text{steel}} = 210$	$E_{\text{al}} = 70$	$E_{\text{kevlar}} = 112$
Density (kg/m^3)	$\rho_{\text{steel}} = 7805$	$\rho_{\text{al}} = 2700$	$\rho_{\text{kevlar}} = 1440$
Poisson ration	ν_{steel}=0.29	$\nu_{\text{al}} = 0.35$	$\nu_{\text{kevlar}} = 0.36$

Table 3.9:

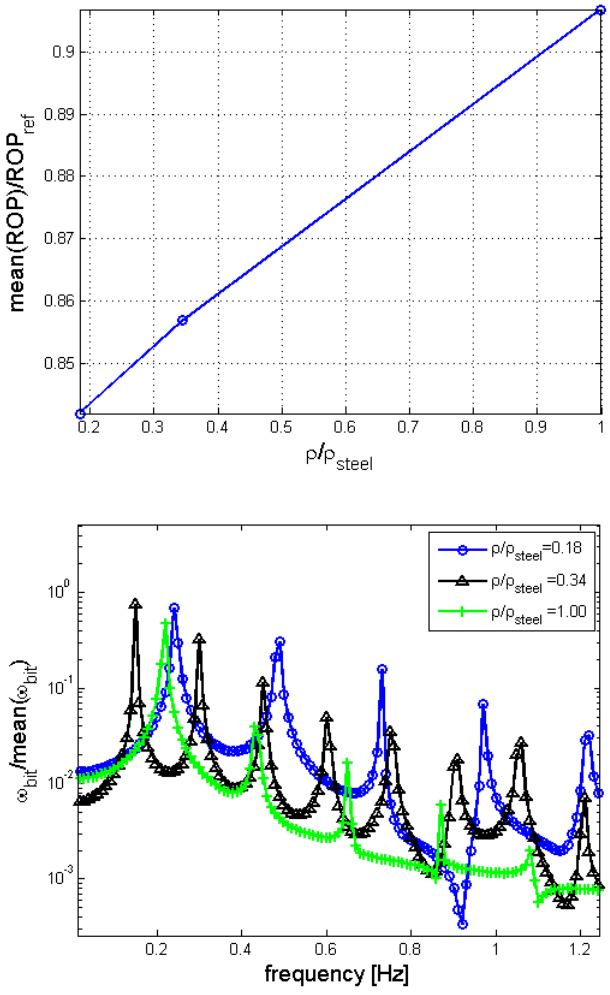

Figure 3.26: Results for different column materials (a) dimensionless ROP and (b) frequency response of the dimensionless rotational speed of the bit

For the points analyzed, $D_{\text{o}}/D_{\text{ch}} = 0.73$ presented the maximum dimensionless ROP=0.904, but the differences are lower than 1%. Figure 3.28(b) shows the frequency spectrum of the dimensionless ω_{bit} . It can be noticed that the results are only slightly different, since a change in D_{ch} will not affected considerably the fluid matrices and, consequently, will produce a small variation on the dynamical characteristics of the system. It should be observed that, for the cases analyzed, there were no impacts between the column and the borehole.

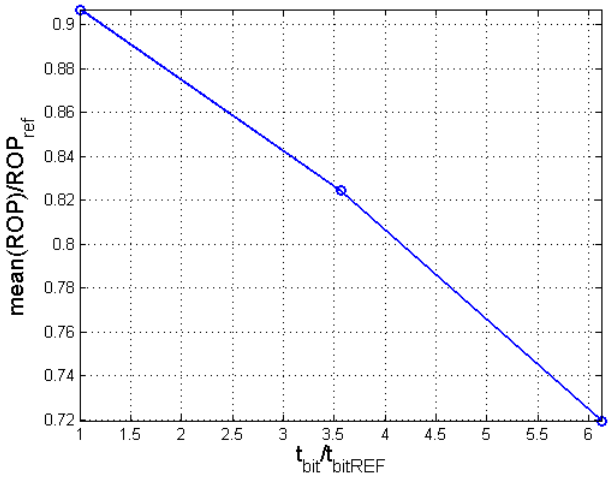

(a)

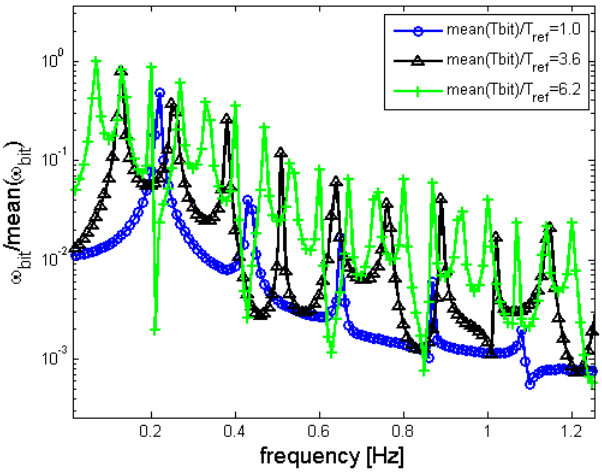

(b)

Figure 3.27: Results for different torques at the bit (a) dimensionless ROP and (b) frequency response of the dimensionless rotational speed of the bit

The analysis presented in this Section was not intended to be exhaustive. We will limit the analysis to these cases, since our goal is to model the uncertainties of the problem and investigate how these uncertainties propagate throughout the system. We leave further analysis for the future.

3.8 Summary of the Chapter

The drill-string dynamics accounting for the drilling fluid (mud) was analyzed in this Chapter. The column was modeled using the Timoshenko beam theory and discretized by means of the Finite Element Method. Finite strains (which couple axial, lateral and torsional vibrations) are considered

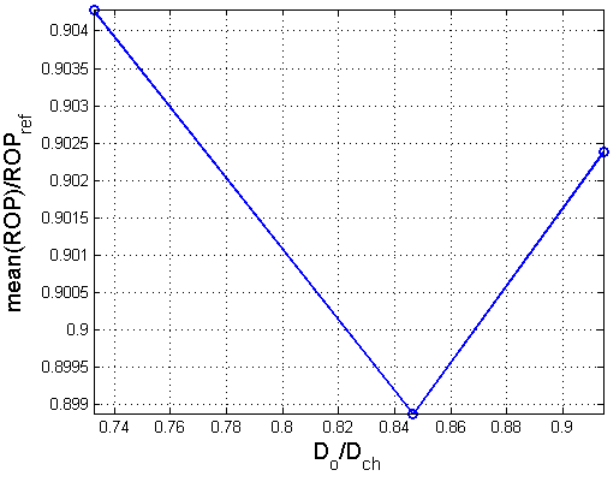

(a)

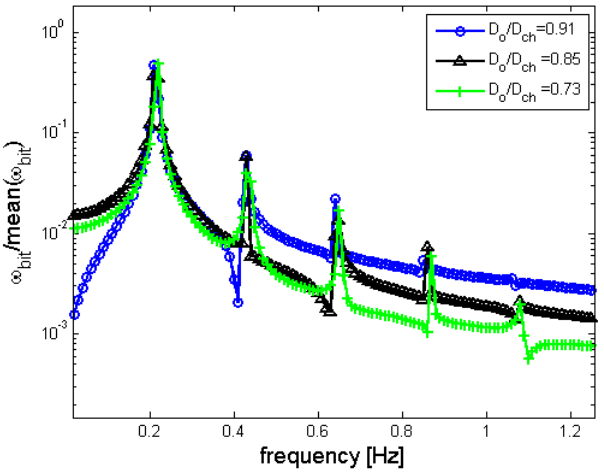

(b)

Figure 3.28: Results for different channel diameters (a) dimensionless ROP and (b) frequency response of the dimensionless rotational speed of the bit

with no simplifications and the dynamics is calculated in a prestressed configuration. A bit-rock interaction model [130] that describes how the bit penetrates the soil is used. The fluid-structure interaction model found in [81] was extended for the analyzed problem. It has been observed that the presence of the fluid changes the dynamical response of the system, especially the lateral vibration of the structure.

For future works, it should be considered to apply a more detailed model for the fluid. It is too computationally expensive to solve the whole fluid-dynamics problem, but if some terms are simplified, as it was done in [83] (see appendix G), the problem can be solved in a reasonable computational time.

4
Probabilistic model

With the discovery of new oil reservoirs, there is an increasing interest on the development of computational models to support engineer decisions. In this context, uncertainties should be taken into account in the computational model in order to improve the robustness of the numerical predictions. The dynamics of a drill-string is highly affected by the bit-rock interaction, hence, this interaction is of upmost importance for the drill-string dynamics. In addition, modeling the bit-rock interaction is not trivial, and simple models are usually considered in the analysis. This is an important constraint when uncertainties are to be taken into account, since the parametric probabilistic approach limits the analysis. Therefore, in Section 4.2, we propose to use the nonparametric probabilistic approach to model uncertainties in the bit-rock interaction model of a drill-string system. The nonparametric probabilistic approach is also applied to model the mass, stiffness and damping operators of the dynamical system (see Section 4.1).

Figure 4.1 summarizes the forces taken into account in the analysis: the motor torque (as a constant rotational speed at the top Ω_x), the supporting force f_{hook}, the torque t_{bit} and force f_{bit} at the bit, the weight of the column, the fluid forces, the impact and rubbing between the column and the borehole, the forces due to the stabilizer, and also the elastic and kinetic forces due to the deformation and to the motion of the structure.

The computational models used to describe the drill-string dynamics mentioned in Chapter 3 ([134, 23, 24, 129, 130, 54, 128, 55, 84, 101]) are able to quantify some effects that occur in a drilling operation (such as the stick-slip oscillations) but they cannot predict correctly the dynamical response of a real system. This can be explained, first because the above models are too simple compared to the real system and, second because uncertainties are not taken into account. In a drilling operation there are many sources of uncertainties such as material properties (column and drilling fluid), dimensions of the system (especially the borehole),

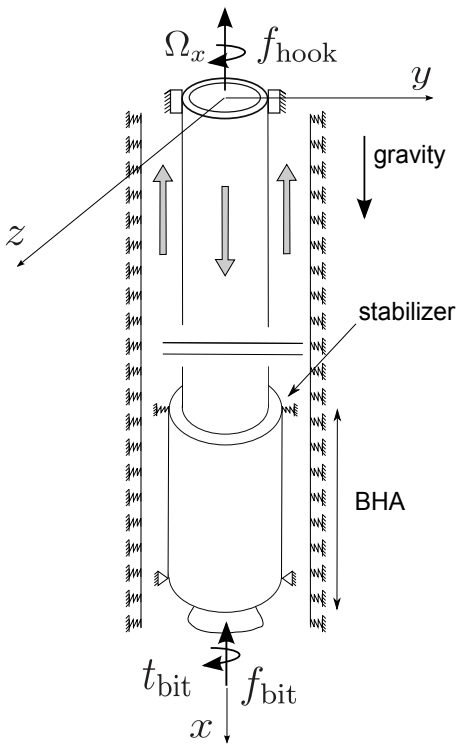

Figure 4.1: General scheme of the drill-string system.

fluid-structure interaction and bit-rock interaction. There are few articles treating the stochastic problem of the drill-string dynamics; in especial we may cite [87, 124, 123, 58]. Ritto et al. [87], propose a probabilistic model for the bit-rock interaction model (see Section 4.2), Spanos et al. [124, 123], analyze stochastic lateral forces at the bit, and Kotsonis and Spanos [58] analyze a random weight-on-bit using a simple two degrees of freedom drill-string model.

The deterministic model used is the one that was presented in Chapter 3. The present Chapter discusses a wide range of tools in stochastic modeling, but no detailed treatment is given. Readers are encouraged to go to the indicated references if they are willing to understand the details of the formulations presented. This Chapter also has the intention of covering from the construction of the probabilistic model for the random variables to the robust optimization of the problem (which is the ultimate goal of a stochastic analysis), passing through the identification of the probabilistic model. It is organized as follows. The probabilistic model is presented in Sections 4.1, 4.2, 4.3 and 4.4. The identification procedure to identify the probabilistic model is presented in Sections 4.5 and 4.6. Finally, the robust optimization problem is depicted in Sections 4.7 and 4.8.

4.1
Model uncertainties for the structure coupled with the fluid

The physical theory used to model the mechanical system (for instance, beam theory for the column, simple fluid-structure interaction, etc.) is a simplification of the real system. Therefore, it is necessary to take into account model uncertainties induced by the model errors. One way to take into account model uncertainties is to use the nonparametric probabilistic approach [112, 116, 72, 120] for which applications with experimental validation can be found in [22, 30, 32].

To construct the random reduced matrices, the ensemble SE^{+0} and SE^{+} of random matrices defined in [116] are used. The first step is to decompose the matrices of the deterministic model as:

$$\begin{aligned} [M_r] &= [\underline{L}_M]^T[\underline{L}_M], \\ [C_r] &= [\underline{L}_C]^T[\underline{L}_C], \\ [K_r] &= [\underline{L}_K]^T[\underline{L}_K], \end{aligned} \tag{4-1}$$

where $[\underline{L}]$ is an upper triangular matrix obtained using the Cholesky decomposition. Matrices $[M_r]$, $[C_r]$, $[K_r]$, $[\underline{L}_M]$ and $[\underline{L}_C]$ have dimension $n \times n$ and matrix $[\underline{L}_K]$ has dimension $p \times n$ in which p is equal to $(n - \mu_{\mathrm{rig}})$, where μ_{rig} is the dimension of the null space of $[K_r]$ (note that $\mu_{\mathrm{rig}} = 2$ for the problem considered). The nonparametric probabilistic approach consists in substituting the matrices of the reduced deterministic model by the following three independent random matrices

$$\begin{aligned} [\mathbf{M}_r] &= [\underline{L}_M]^T[\mathbf{G}_M][\underline{L}_M], \\ [\mathbf{C}_r] &= [\underline{L}_C]^T[\mathbf{G}_C][\underline{L}_C], \\ [\mathbf{K}_r] &= [\underline{L}_K]^T[\mathbf{G}_K][\underline{L}_K], \end{aligned} \tag{4-2}$$

in which $[\mathbf{G}_M]$, $[\mathbf{G}_C]$ and $[\mathbf{G}_K]$ are random matrices belonging to the ensemble SE^{+} defined in [116]. Matrices $[\mathbf{G}_M]$ and $[\mathbf{G}_C]$ have dimension $n \times n$ and matrix $[\mathbf{G}_K]$ has dimension $p \times p$.

The probability distribution of $[\mathbf{G}_A]$ (for $A \in \{M, C, K\}$) is constructed using the Maximum Entropy Principle [107, 49, 50], which yields an optimization problem:

$$p^*_{[\mathbf{G}_A]} = \arg \max_{p_{[\mathbf{G}_A]} \in \mathcal{C}^p} S(p_{[\mathbf{G}_A]})\,. \tag{4-3}$$

In other words, find the optimal probability density function $p^*_{[\mathbf{G}_A]}$, such that $\forall p_{[\mathbf{G}_A]} \in \mathcal{C}^p,\ S(p^*_{[\mathbf{G}_A]}) \geq S(p_{[\mathbf{G}_A]})$. In Eq. (4-3) $p_{[\mathbf{G}_A]}$ is the probability density function, $\mathcal{C}^p$ is the set of admissible probability density functions that respect the available information presented in the sequence. Before that, the Shannon entropy measure S is defined [107]:

$$S(p_{[\mathbf{G}_A]}) = -\int_{\mathbb{M}^+} p_{[\mathbf{G}_A]} \ln\left(p_{[\mathbf{G}_A]}\right) d[\mathbf{G}]\,, \tag{4-4}$$

where $\mathbb{M}^+$ is the set of all positive-defined matrices. Matrix $[\mathbf{G}_A]$ satisfies the following available information [112, 116]:

1. Random matrix $[\mathbf{G}_A]$ is positive-definite almost surely,
2. $\mathcal{E}\{[\mathbf{G}_A]\} = [\,I\,]$,
3. $\mathcal{E}\{||[\mathbf{G}_A]^{-1}||_F^2\} = \mathrm{c}_1\ ,\ |\mathrm{c}_1| < +\infty$,

in which $[\,I\,]$ is the identity matrix. Taking into account the above available information and using the Maximum Entropy Principle yield the following probability density function of $[\mathbf{G}_A]$ [116]

$$p^*_{[\mathbf{G}_A]}([G_A]) = \mathbb{1}_{\mathbb{M}_n^+(\mathbb{R})}([G_A]) C_{\mathbf{G}} \det([G_A])^{(n+1)\frac{(1-\delta^2)}{2\delta^2}} \exp\left\{-\frac{n+1}{2\delta^2}\mathrm{tr}([G_A])\right\}, \tag{4-5}$$

where $\det(\cdot)$ is the determinant, $\mathrm{tr}(\cdot)$ is the trace. The normalization constant is written as

$$C_{\mathbf{G}_A} = \frac{(2\pi)^{-n(n-1)/4}\left(\frac{n+1}{2\delta^2}\right)^{n(n+1)/(2\delta^2)}}{\prod_{j=1}^{n}\Gamma\left((n+1)/(2\delta^2)+(1-j)/2\right)}\,, \tag{4-6}$$

where $\Gamma(z)$ is the gamma function defined for $z > 0$ by $\Gamma(z) = \int_0^{+\infty} t^{z-1}e^{-t}dt$. The random generator of independent realizations of random matrix $[\mathbf{G}]$ for which the probability density function is defined by Eq. (4-5) is given next. Random $n \times n$ matrix $[\mathbf{G}_A]$ can be written as $[\mathbf{G}_A] = [\mathbf{L}_G]^T[\mathbf{L}_G]$, in which $[\mathbf{L}_G]$ is an upper triangular real random matrix such that:

1. The random variables $\{[\mathbf{L}_G]_{jj'}, j \leq j'\}$ are independent.
2. For $j < j'$ the real-valued random variable $[\mathbf{L}_G]_{jj'} = \sigma V_{jj'}$, in which $\sigma = \delta(n+1)^{-1/2}$ and $V_{jj'}$ is a real-valued gaussian random variable with zero mean and unit variance.

3. For $j = j'$ the real-valued random variable $[\mathbf{L}_G]_{jj} = \sigma(2V_j)^{1/2}$. In which V_j is a real-valued gamma random variable with probability density function written as

$$p_{V_j}(v) = \mathbb{1}_{\mathbb{R}^+}(v)\, \frac{1}{\Gamma\left(\frac{n+1}{2\delta^2} + \frac{1-j}{2}\right)}\; v^{\frac{n+1}{2\delta^2} - \frac{1+j}{2}}\; e^{-v}.$$

The level of statistical fluctuations of random matrix $[\mathbf{G}_A]$ is controlled by the dispersion parameter δ_A defined by

$$\delta_A = \left\{ \frac{1}{n} \mathcal{E}\{ |||[\mathbf{G}_A] - [I]||_F^2 \} \right\}^{\frac{1}{2}}, \tag{4-7}$$

where $\mathcal{E}\{\cdot\}$ denotes the mathematical expectation and $|||[A]||_F = (\text{trace}\{[A][A]^T\})^{1/2}$ denotes the Frobenius norm. Consequently, the level of uncertainties for quantity A is controlled by dispersion parameter δ_A.

4.2
Model uncertainties for the bit-rock interaction

The parametric probabilistic approach allows physical-parameter uncertainties to be modeled. It should be noted that the underlying deterministic model for the bit rock interaction defined by Eq. (3-31) exhibits parameters a_1, a_2, a_3, a_4 and a_5 which do not correspond to physical parameters. Consequently, it is difficult to construct an *a priori* probabilistic model using the parametric probabilistic approach. For instance, there is no available information concerning the statistical dependence of these parameters. Then, we propose to apply the nonparametric probabilistic approach to model uncertainties [112, 120] which consists in modeling the operator of the constitutive equation (Eq. (3-31)) by a random operator depending on the random state of the system. Such an approach allows both system-parameter uncertainties and modeling errors to be globally taken into account.

The nonparametric probabilistic approach has been applied for linear operators [116], then it was extended to nonlinear ones [73, 87, 120]. Let $\mathfrak{f}_{\text{bit}}(\dot{\mathbf{x}}(t))$ and $\dot{\mathbf{x}}(t)$ be such that

$$\mathfrak{f}_{\text{bit}}(\dot{\mathbf{x}}(t)) = \begin{pmatrix} f_{\text{bit}}(\dot{\mathbf{x}}(t)) \\ t_{\text{bit}}(\dot{\mathbf{x}}(t)) \end{pmatrix} \quad \text{and} \quad \dot{\mathbf{x}}(t) = \begin{pmatrix} \dot{u}_{\text{bit}}(t) \\ \omega_{\text{bit}}(t) \end{pmatrix}. \tag{4-8}$$

where f_{bit} is the force at the bit, t_{bit} is the torque at the bit, $\dot{u}_{\text{bit}}$ is the axial speed of the bit and ω_{bit} is the rotational speed of the bit. In the first step of the methodology proposed, we look for a symmetric positive-definite matrix $[A_b(\dot{\mathbf{x}}(t))]$ depending on $\dot{\mathbf{x}}(t)$ such that the virtual power of the bit-rock interactions be written as

$$\delta\mathcal{P}_{\text{bit}}(\dot{\mathbf{x}}(t)) = \quad < \mathfrak{f}_{\text{bit}}(\dot{\mathbf{x}}(t)), \delta\dot{\mathbf{x}}(t) > \quad = \quad - < [A_b(\dot{\mathbf{x}}(t))]\dot{\mathbf{x}}, \delta\dot{\mathbf{x}}(t) > , \quad (4\text{-}9)$$

and such that force $\mathfrak{f}_{\text{bit}}(\dot{\mathbf{x}}(t))$ be given by:

$$\mathfrak{f}_{\text{bit}}(\dot{\mathbf{x}}(t)) = \nabla_{\delta\dot{\mathbf{x}}(t)}\ \delta\mathcal{P}_{\text{bit}}(\dot{\mathbf{x}}(t))\,, \quad (4\text{-}10)$$

Equation (3-31) can be rewritten as

$$\mathfrak{f}_{\text{bit}}(\dot{\mathbf{x}}(t)) = -[A_b(\dot{\mathbf{x}}(t))]\dot{\mathbf{x}}(t) = -\begin{pmatrix} \dfrac{a_1}{a_2} + \dfrac{\dot{u}_{\text{bit}}(t)}{a_2 Z(\omega_{\text{bit}}(t))^2} - \dfrac{a_3\omega_{\text{bit}}(t)}{a_2 Z(\omega_{\text{bit}}(t))} \\ \dfrac{a_4 Z(\omega_{\text{bit}}(t))^2\dot{u}_{\text{bit}}(t)}{\omega_{\text{bit}}(t)} + a_5 Z(\omega_{\text{bit}}(t)) \end{pmatrix}. \quad (4\text{-}11)$$

From Eqs. (4-9) to (4-11) it can be deduced that

$$\begin{aligned} [A_b(\dot{\mathbf{x}})]_{11} &= \frac{a_1}{a_2\dot{u}_{\text{bit}}(t)} + \frac{1}{a_2 Z(\omega_{\text{bit}}(t))^2} - \frac{a_3\omega_{\text{bit}}(t)}{a_2 Z(\omega_{\text{bit}}(t))\dot{u}_{\text{bit}}(t)}\,, \\ [A_b(\dot{\mathbf{x}}(t))]_{22} &= \frac{a_4 Z(\omega_{\text{bit}}(t))^2\dot{u}_{\text{bit}}(t)}{\omega^2_{\text{bit}(t)}} + \frac{a_5 Z(\omega_{\text{bit}}(t))}{\omega_{\text{bit}}(t)}\ , \\ [A_b(\dot{\mathbf{x}}(t))]_{12} &= [A_b(\dot{\mathbf{x}}(t))]_{21} = 0\,. \end{aligned} \quad (4\text{-}12)$$

For all $\dot{\mathbf{x}}(t)$ belonging to its admissible space $\mathcal{C}$, $[A_b(\dot{\mathbf{x}}(t))]$ is positive-definite.

The second step consists, for all deterministic vector $\dot{\mathbf{x}}(t)$ belonging to $\mathcal{C}$, in modeling matrix $[A_b(\dot{\mathbf{x}}(t))]$ by a random matrix $[\mathbf{A}_b(\dot{\mathbf{x}}(t))]$ with values in the set $\mathbb{M}_2^+(\mathbb{R})$ of all positive-definite symmetric (2×2) real matrices. Note that $\{[\mathbf{A}_b(\dot{\mathbf{x}}(t))], t > 0\}$ is a stochastic process with values in $\mathbb{M}_2^+(\mathbb{R})$. Thus, for all $\dot{\mathbf{x}}(t)$ in $\mathcal{C}$, the constitutive equation defined by Eq. (4-11) becomes a

random constitutive equation which can be written as

$$\mathfrak{F}_{\text{bit}}(\dot{\mathbf{x}}(t)) = -[\mathbf{A}_b(\dot{\mathbf{x}}(t))]\dot{\mathbf{x}}(t)\,. \tag{4-13}$$

The third step consists in constructing the probability distribution of random variable $[\mathbf{A}_b(\dot{\mathbf{x}}(t))]$ for all fixed vector $\dot{\mathbf{x}}(t)$ in $\mathcal{C}$. The available information is [116]:

1. Random matrix $[\mathbf{A}_b(\dot{\mathbf{x}}(t))]$ is positive-definite almost surely,
2. $\mathcal{E}\{[\mathbf{A}_b(\dot{\mathbf{x}}(t))]\} = [A_b(\dot{\mathbf{x}}(t))]$,
3. $\mathcal{E}\{||[\mathbf{A}_b(\dot{\mathbf{x}}(t))]^{-1}||_F^2\} = \mathrm{c}_2\ ,\ |\mathrm{c}_2| < +\infty$,

in which $\mathcal{E}\{\cdot\}$ is the mathematical expectation and $[A_b(\dot{\mathbf{x}}(t))]$ is the matrix of the deterministic model. Following the methodology of the nonparametric probabilistic approach and using the Cholesky decomposition, the mean value of $[A_b(\dot{\mathbf{x}}(t))]$ is written as

$$[A_b(\dot{\mathbf{x}}(t))] = [L_b(\dot{\mathbf{x}}(t))]^T[L_b(\dot{\mathbf{x}}(t))]\,. \tag{4-14}$$

The random matrix $[\mathbf{A}_b(\dot{\mathbf{x}}(t))]$ is defined by

$$[\mathbf{A}_b(\dot{\mathbf{x}}(t))] = [L_b(\dot{\mathbf{x}}(t))]^T[\mathbf{G}_b][L_b(\dot{\mathbf{x}}(t))]\,. \tag{4-15}$$

In the above equation, $[\mathbf{G}_b]$ is a random matrix of the same class of $[\mathbf{G}_A]$, see Eq. (4-5). It should be noted that, in the construction proposed, random matrix $[\mathbf{G}_b]$ neither depends on $\dot{\mathbf{x}}$ nor on t. Let the dispersion parameter δ be such that

$$\delta = \left\{\frac{1}{2}\mathcal{E}\{||[\mathbf{G_b}] - [I]||_F^2\}\right\}^{\frac{1}{2}}\,. \tag{4-16}$$

4.3
Stochastic system of equations

If the only uncertainty is related to the bit-rock interaction, the stochastic system of equations is such that

$$\begin{aligned} &[M_r]\ddot{\mathbf{Q}}(t) + [C_r]\dot{\mathbf{Q}}(t) + [K_r]\mathbf{Q}(t) = \\ &= [\Phi]^T(\mathbf{g}(t) + \mathbf{F}_{\rm br}(\dot{\mathbf{Q}}(t)) + \mathbf{f}_{\rm ip}(\mathbf{Q}(t)) - \mathbf{f}_{\rm NL}(\mathbf{Q}(t), \dot{\mathbf{Q}}(t), \ddot{\mathbf{Q}}(t)))\,, \\ &\overline{\mathbf{U}}(t) = [\Phi]\mathbf{Q}(t) \quad , \quad \mathbf{q}(0) = \mathbf{q}_0 \quad , \quad \dot{\mathbf{q}}(0) = \mathbf{v}_0\,, \end{aligned} \tag{4-17}$$

where $\mathbf{Q}$ is the random response of the reduced stochastic system and the only source of uncertainty is related to the bit-rock interaction $\mathbf{F}_{\rm br}$ whose probabilistic model is defined by Eq. (4-13).

When the structure coupled with the fluid is also taken as uncertain, the stochastic system of equations is such that

$$\begin{aligned} &[\mathbf{M}_r]\ddot{\mathbf{Q}}(t) + [\mathbf{C}_r]\dot{\mathbf{Q}}(t) + [\mathbf{K}_r]\mathbf{Q}(t) = \\ &= [\Phi]^T(\mathbf{g}(t) + \mathbf{F}_{\rm br}(\dot{\mathbf{Q}}(t)) + \mathbf{f}_{\rm ip}(\mathbf{Q}(t)) - \mathbf{f}_{\rm NL}(\mathbf{Q}(t), \dot{\mathbf{Q}}(t), \ddot{\mathbf{Q}}(t)))\,, \\ &\overline{\mathbf{U}}(t) = [\Phi]\mathbf{Q}(t) \quad , \quad \mathbf{q}(0) = \mathbf{q}_0 \quad , \quad \dot{\mathbf{q}}(0) = \mathbf{v}_0\,, \end{aligned} \tag{4-18}$$

where $[\mathbf{M}_r]$, $[\mathbf{K}_r]$ and $[\mathbf{C}_r]$ are the random matrices defined by Eq. (4-2).

4.4
Numerical results of the stochastic analysis (uncertain bit-rock interaction model)

In this Section, we consider just the uncertainties related to the bit-rock interaction model; in Section 4.7 the complete probabilistic model is used. All the numerical results presented below correspond to the forced response (deterministic case) and to the stationary response (stochastic case) for which the transient part of the response induced by the initial conditions has vanished. The results presented are the time response and the frequency spectrum, which is defined as the modulus of the Fourier transform of the steady state time response.

4.4.1 Convergence of the stochastic solution

Let $[\overline{\mathbf{U}}(t, s_j)]$ be the response of the stochastic dynamical system calculated for each realization s_j. The mean-square convergence analysis with respect to the number n_s of independent realizations is carried out studying the function $\text{conv}(n_s)$ defined by

$$\text{conv}(n_s) = \frac{1}{n_s} \sum_{j=1}^{n_s} \int_{t_0}^{t_1} ||\overline{\mathbf{U}}(t, s_j)||^2 dt \,. \tag{4-19}$$

where t_f is the simulation time. Figure 4.2 shows that the mean-square convergence is reached for 150 simulations.

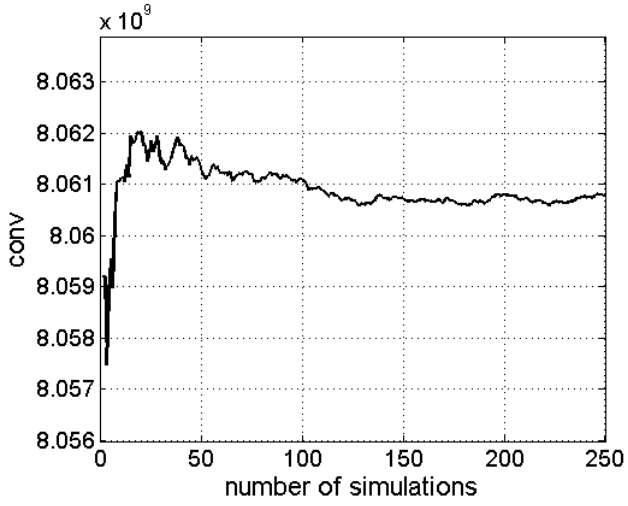

Figure 4.2: Typical mean square convergence curve.

4.4.2 Stochastic response

The stochastic response is computed for three values of the dispersion parameter δ that controls the uncertainties of the bit-rock interaction model, which are 0.001, 0.01, 0.1. Figure 4.3 displays the random ROP for $\delta = 0.001$. This figure shows the response of the deterministic model together with the mean response of the stochastic model and the 95% envelope (which means that the confidence region is constructed with a probability level of 0.95). The upper and lower envelopes of the confidence region are calculated using the method of quantiles [106].

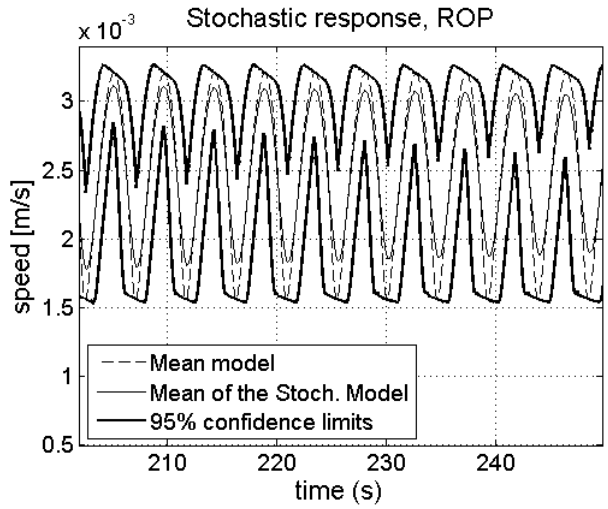

(a)

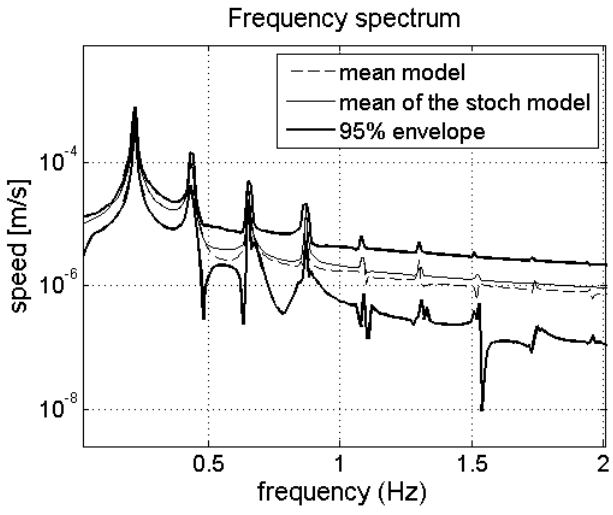

(b)

Figure 4.3: Stochastic response for $\delta = 0.001$. ROP (a) and its frequency spectrum (b).

Figure 4.3(b) shows that the dispersion of the random ROP is already significant in the high part of the frequency band. However, the stochastic response in the low part of the frequency band is robust for the level of uncertainties considered. Figure 4.4 shows the random weight-on-bit and torque-on-bit. It should be noted that, for each time t, the coefficients of variation of the random weight-on-bit and of the random torque-on-bit are small ($\sim 5 \times 10^{-3}$). Nevertheless, although this dispersion is small, it induces a significant dispersion on the stochastic response (~ 0.15 for the coefficient of variation of the random ROP, for instance). Figure 4.5 shows the random rotational speed of the bit and Fig. 4.6 shows the random radial displacement at $x = 700$ m (middle point of the drill pipe). It can be seen that the lateral vibrations are also affected by the probabilistic model of the bit-rock interaction.

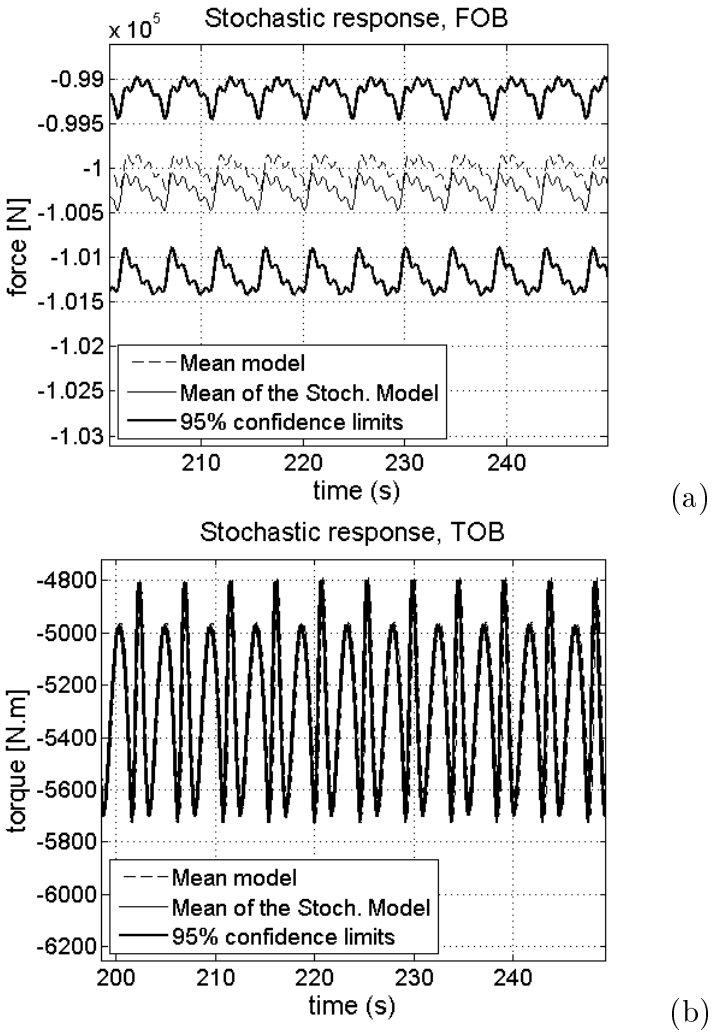

Figure 4.4: Stochastic response for $\delta = 0.001$. (a) weight-on-bit, (b) torque-on-bit.

As δ increases the stochastic response gets more uncertain with wider statistical envelopes. Figure 4.7 shows the random ROP and Fig. 4.8 shows the random rotational speed of the bit (ω_{bit}) for $\delta = 0.01$. Note that some other peaks appear in the frequency spectrum. Figure 4.9 shows the random radial displacement; there are some realizations where impacts occur between the column and the borehole (see Fig. 4.9(a)).

Figure 4.10 shows the random rotational speed of the bit for $\delta = 0.1$. It can be noted that, for this level of uncertainty, the dispersion of the stochastic response is significant for all frequency band analyzed. Figure 4.11 shows some Monte Carlo realizations of the stochastic ROP. The arrows in Fig. 4.11 indicate that, for some realizations, the bit loses contact with the soil. The phenomenon bit-bounce is not included in our computational model, so the simulation is stopped if the bit looses contact with the soil.

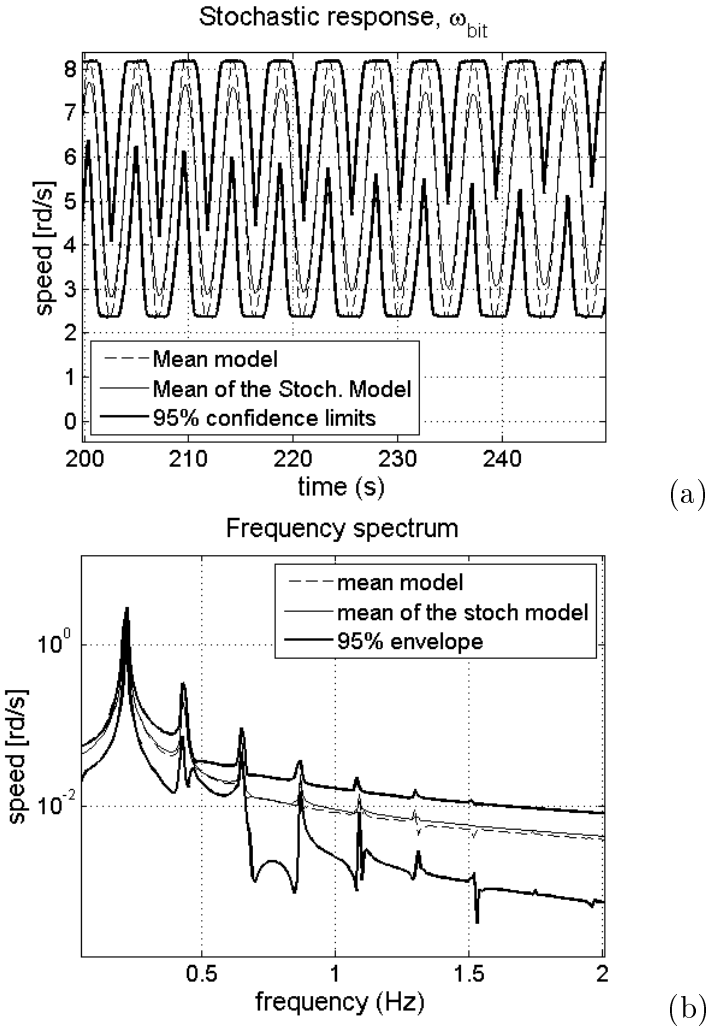

Figure 4.5: Stochastic response for $\delta = 0.001$. Rotational speed of the bit (a) and its frequency spectrum (b).

The probabilistic model proposed for the bit-rock interaction model allows us to simulate cases such as the bit losing contact with the soil and the column impacting the borehole. The nonparametric probabilistic approach permits both system-parameter and modeling errors to be taken into account for the bit-rock interaction model.

4.5 Identification procedure

In the last Section, a sensitivity analysis was performed with parameter δ (see Eq. (4-16)). This parameter is a measure of the uncertainty of the bit-rock interaction model and its value should be identified by means of field data (or experimental responses). Unfortunately, we do not

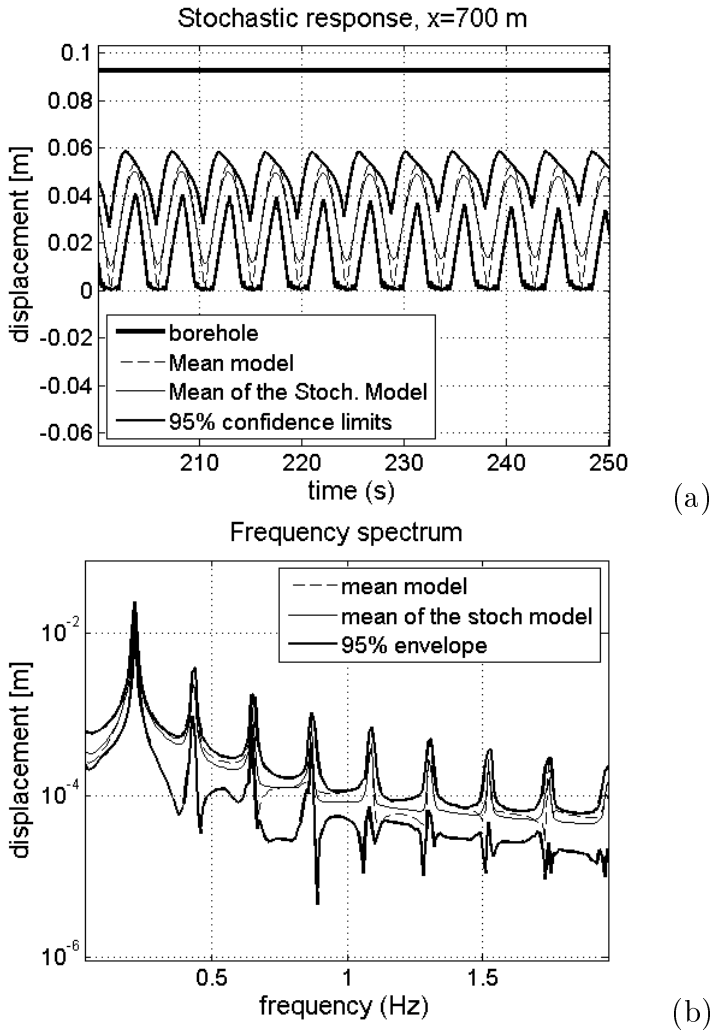

Figure 4.6: Stochastic response for $\delta = 0.001$. Radial displacement at $x = 700$ m (a) and its frequency spectrum (b).

have field data to identify this parameter, nevertheless, an identification procedure will be presented in this Section. The identification of parameter δ of the probabilistic model of the bit-rock interaction is carried out using the maximum likelihood method for the random observations. In order to implement it, a statistical reduction of the random observations is performed.

In the context of drill-string dynamics identification, Berzi et al. [14] do the identification of the nonlinear dissipative spring mass model of a coupling sleeve joint, where the identification is done minimizing the distance (calculated using the Euclidean norm) between numerical and experimental responses. At the best of our knowledge, a probabilistic drill-string dynamics identification has not yet been investigated in the literature. Recently, Soize [118] presents some strategies for probabilistic

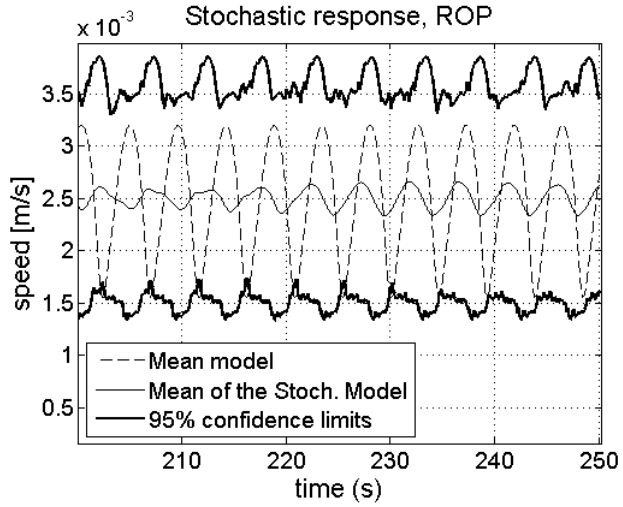

(a)

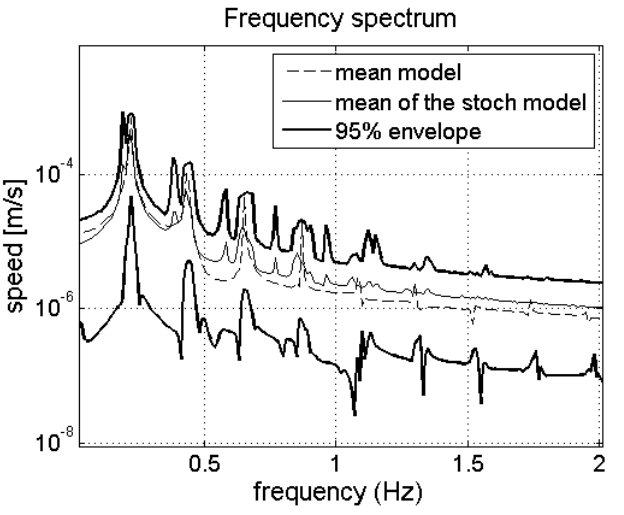

(b)

Figure 4.7: Stochastic response for $\delta = 0.01$. ROP (a) and its frequency spectrum (b).

identification in uncertain computational models for dynamical systems; in particular, this work presents the use of the maximum likelihood method ([3, 106, 126]) in the case for which the output observation vector of the dynamical system is a correlated stochastic process indexed by an uncountable set. For such a case, it is proposed [118] to apply the maximum likelihood method to the uncorrelated random variables corresponding to the coordinates of the Principal Component Analysis (PCA) of the correlated stochastic process modeling the output observation. Below, we propose to reuse such an approach to identify the probabilistic model parameter δ (which measures the uncertainty level of the bit-rock interaction nonparametric probabilistic model) in the context of nonlinear dynamics. The correlated stochastic process which models the time dependent output observation vector (which is obtained by solving the nonlinear stochastic

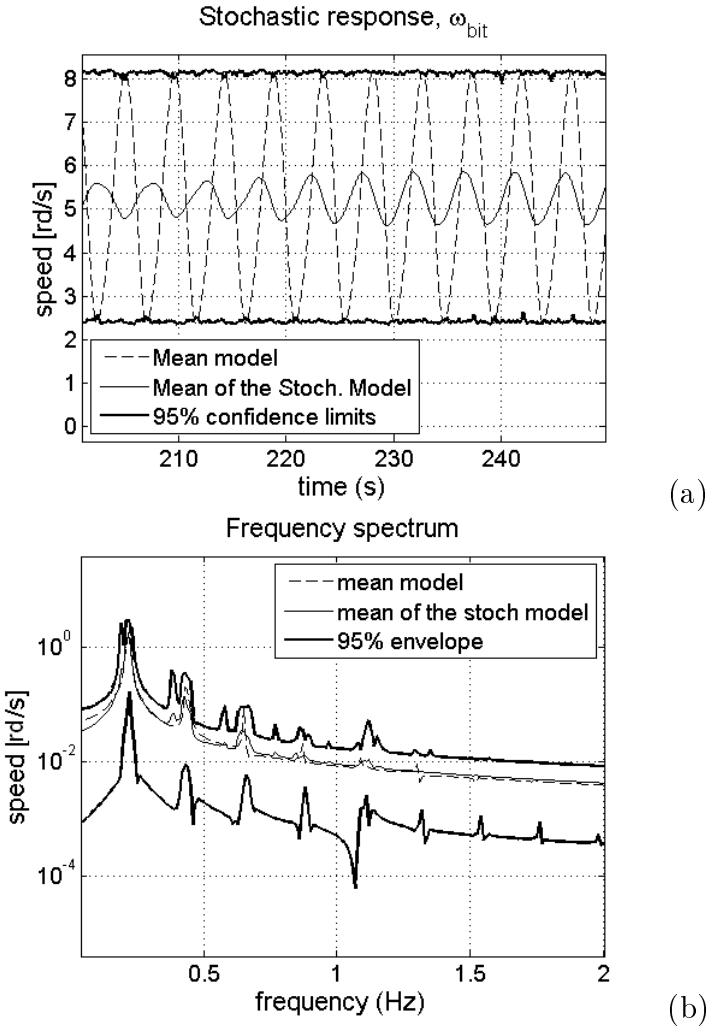

Figure 4.8: Stochastic response for $\delta = 0.01$. Rotational speed of the bit ω_{bit} (a) and its frequency spectrum (b).

dynamical equation of the drill-string system) is reduced using the PCA. Then, the maximum likelihood method is used to identify the uncertainties of a nonlinear constitutive equation (bit-rock interaction model). In the present analysis, we aim to validate this procedure with an experimental response that is actually generated numerically (such a procedure could then be applied using the experimental response of a real drill-string system).

4.5.1 Maximum Likelihood Method

Let $\{W(t,\delta), t > 0\}$ be a stochastic process of the dynamical system deduced from the random response $\{\mathbf{U}(t), t > 0\}$ of the stochastic dynamical system defined by Eq. (4-17). For the identification of parameter δ of the probabilistic model, we use the response in the frequency domain. We then

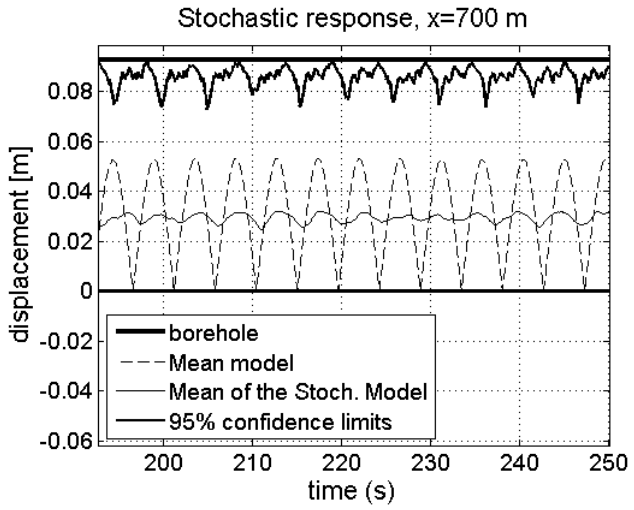

(a)

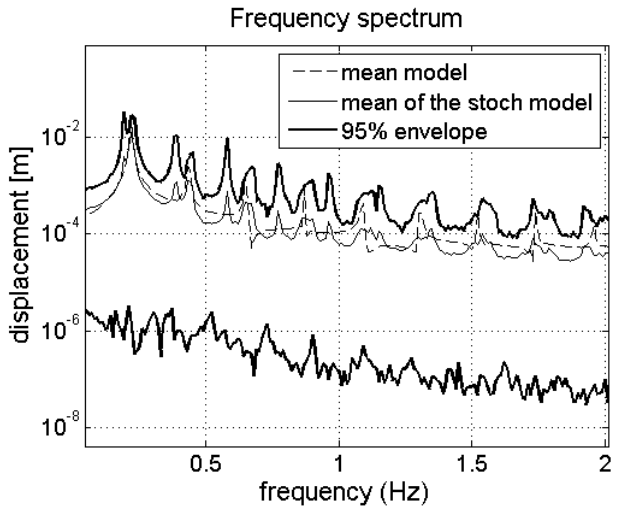

(b)

Figure 4.9: Stochastic response for $\delta = 0.01$. Radial displacement at $x = 700$ m and its frequency spectrum (b).

introduce the random frequency spectrum $\widehat{W}(\omega, \delta)$ as the modulus of the Fourier transform of $W(t, \delta)$ with the time window $[t_i\,, t_f]$, such that

$$\widehat{W}(\omega, \delta) = \left| \int_{t_i}^{t_f} e^{-i\omega t}\, W(t, \delta)\, dt \right| , \tag{4-20}$$

with $i = \sqrt{-1}$. The time interval $[t_i\,, t_f]$ only includes the random forced response of $W(t, \delta)$ (transient part induced by the initial condition is vanished at time t_i) and ω belongs to the frequency band of the analysis B. This random spectrum is calculated using the stochastic model with a frequency sampling $\{\omega_1, \ldots, \omega_{n_\omega}\}$ yielding the dependent random variables $\widehat{W}(\omega_1), \ldots, \widehat{W}(\omega_{n_\omega})$. It is assumed that only one experimental observation is available (which is generally the case for such a complex dynamical system). The frequency-sampled experimental observation corresponding to the

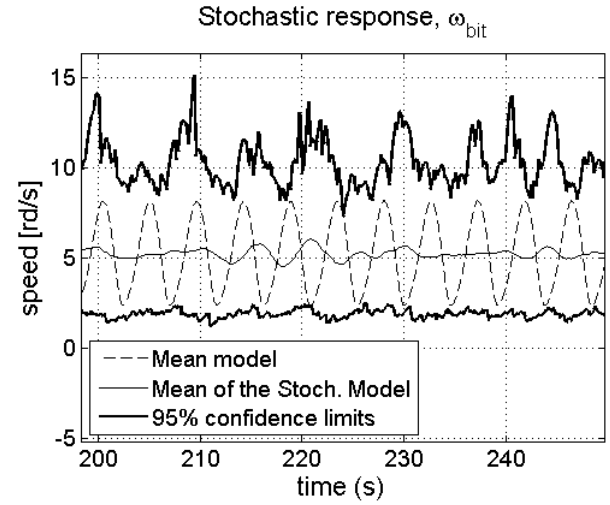

(a)

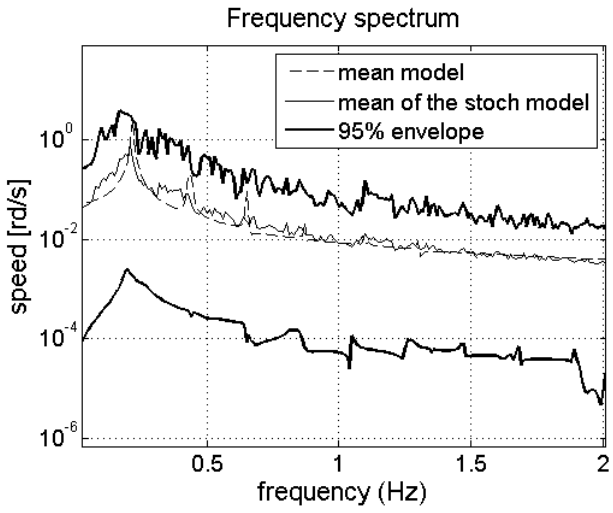

(b)

Figure 4.10: Stochastic response for $\delta = 0.1$. Rotational speed of the bit ω_{bit} (a) and its frequency spectrum (b).

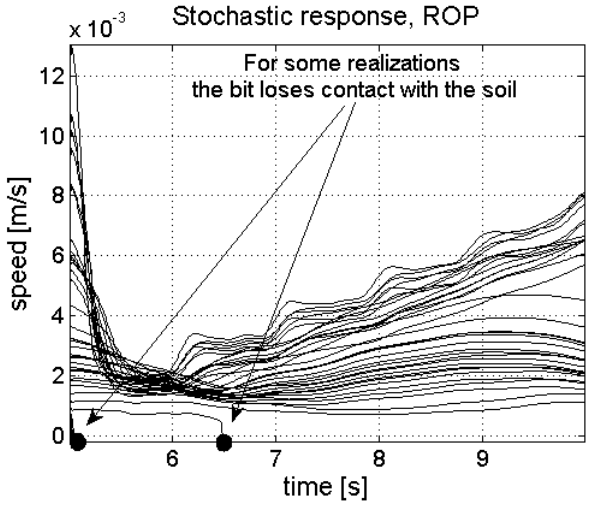

Figure 4.11: Random ROP for $\delta = 0.1$.

frequency sampling of $\widehat{W}(\omega,\delta)$ is then denoted by $\widehat{w}^{\exp}(\omega_1),\ldots,\widehat{w}^{\exp}(\omega_{n_\omega})$. The log-likelihood function $\mathrm{L}(\delta)$ is such that (see for instance [106, 126]),

$$\mathrm{L}(\delta) = \log_{10} p(\widehat{w}^{\exp}(\omega_1),\ldots,\widehat{w}^{\exp}(\omega_{n_\omega});\delta)\,, \tag{4-21}$$

in which $p(w_1,\ldots,w_{n_\omega};\delta)$ is the joint probability density function of the dependent random variables $\widehat{W}(\omega_1),\ldots,\widehat{W}(\omega_{n_\omega})$ which is estimated with the stochastic model. Parameter δ belongs to an admissible set $\mathcal{C}_\delta$ and consequently, the maximum likelihood method allows the optimal value δ^{opt} of δ to be calculated solving the following optimization problem,

$$\delta^{\mathrm{opt}} = \arg\max_{\delta\,\in\,\mathcal{C}_\delta}\ \mathrm{L}(\delta)\,. \tag{4-22}$$

If n_ω is not small, which is generally the case, the numerical cost for solving this optimization problem can be prohibitive. If the random variables $\widehat{W}(\omega_1),\ldots,\widehat{W}(\omega_{n_\omega})$ were not correlated, the following approximation of the log-likelihood function could be introduced

$$\mathrm{L}(\delta) = \sum_{k=1}^{n_\omega} \log_{10} p_{\widehat{W}(\omega_k)}(\widehat{w}^{\exp}(\omega_k);\delta)\,, \tag{4-23}$$

in which $p_{\widehat{W}(\omega_k)}(w_k;\delta)$ would be the probability density function of the random variable $\widehat{W}(\omega_k)$. Since the dependent random variables $\widehat{W}(\omega_1),\ldots,\widehat{W}(\omega_{n_\omega})$ are correlated, such an approximation would not be correct. We then introduce a statistical reduction allowing the maximum likelihood method to be applied to uncorrelated random variables as explained in [118].

Appendix H presents a simple application of the maximum likelihood method.

4.5.2 Statistical reduction

Let $\mathbb{W}(\delta) = (\widehat{W}(\omega_1,\delta),\ldots,\widehat{W}(\omega_{n_\omega},\delta))$ be the $\mathbb{R}^{n_\omega}$-valued random variable whose mean value is $\mathbb{M}(\delta) = \mathcal{E}\{\mathbb{W}(\delta)\}$ and for which the positive $n_\omega \times n_\omega$ covariance matrix is

$$[\mathbb{C}(\delta)] = \mathcal{E}\{(\mathbb{W}(\delta)-\mathbb{M}(\delta))\,(\mathbb{W}(\delta)-\mathbb{M}(\delta))^T\}. \tag{4-24}$$

These second-order moments are usually estimated using mathematical statistics with the stochastic dynamical model. The statistical reduction is then usually obtained by performing a Principal Component Analysis (see for instance [52]). If applied to a continuous process, PCA is known as Karhunen-Loève decomposition. It is named after K. Karhunen [53] and M. Loève [67]. KL-decomposition is also employed to image processing and to many engineering applications [45], and, in mechanical engineering, the first applications have been in turbulence [68]. In structural dynamics, this technique can be used to extend modal analysis and model reduction, see, for instance [10, 11, 102].

Back to our problem, we then introduce the following eigenvalue problem using the covariance matrix

$$[\mathbb{C}(\delta)]\,\mathbb{X}(\delta) = \lambda(\delta)\mathbb{X}(\delta)\,. \tag{4-25}$$

Let $\lambda_1(\delta) \geq \ldots \geq \lambda_{N_{\rm red}}(\delta) > 0$ be the $N_{\rm red} < n_\omega$ largest and strictly positive eigenvalues. Let $\mathbb{X}^1(\delta), \ldots, \mathbb{X}^{N_{\rm red}}(\delta)$ be the associated eigenvectors which constitute an orthonormal family for the Euclidean inner product $< \cdot, \cdot >$. Therefore the approximation $\mathbb{W}^{N_{\rm red}}(\delta)$ of $\mathbb{W}(\delta)$ is written as

$$\mathbb{W}^{N_{\rm red}}(\delta) = \mathbb{M}(\delta) + \sum_{k=1}^{N_{\rm red}} \sqrt{\lambda_k(\delta)}\, Y_k(\delta)\, \mathbb{X}^k(\delta)\,. \tag{4-26}$$

The random variables $Y_1(\delta), \ldots, Y_{N_{\rm red}}(\delta)$ are defined by

$$Y_k(\delta) = \frac{1}{\sqrt{\lambda_k(\delta)}} < (\mathbb{W}(\delta) - \mathbb{M}(\delta))\,, \mathbb{X}^k(\delta) > \tag{4-27}$$

and are uncorrelated, centered, second-order, real-valued random variables, that is to say, are such that

$$\mathcal{E}\{Y_k(\delta)\} = 0 \quad \text{and} \quad \mathcal{E}\{Y_j(\delta)\, Y_k(\delta)\} = \delta_{jk}\,, \tag{4-28}$$

where δ_{jk} is the Kronecker delta. The reduction is effective if $N_{\rm red} << n_\omega$, and it is chosen in order that

$$|||\mathbb{W}(\delta) - \mathbb{W}^{N_{\rm red}}(\delta)||| \leq \sqrt{\epsilon}\, |||\mathbb{W}(\delta)]|||\,, \tag{4-29}$$

in which ϵ is a given accuracy, where $|||\cdot|||$ is such that $|||\mathbb{W}|||^2 = \mathcal{E}\{||\mathbb{W}||^2\}$ and where $\|\cdot\|$ is the Euclidean norm. Therefore, $|||\mathbb{W}(\delta) - \mathbb{W}^{N_{\text{red}}}(\delta)|||^2 = \text{tr}([\mathbb{C}(\delta)]) - \sum_{k=1}^{N_{\text{red}}} \lambda_k(\delta)$, where $\text{tr}(\cdot)$ is the trace of a matrix. It can then be deduced that N_{red} has to be chosen such that

$$N_{\text{red}} = \arg \left\{ \max_{N \in \{1,2,..,n_\omega\}} \left(1 - \frac{\sum_{k=1}^{N} \lambda_k(\delta)}{\text{tr}([\mathbb{C}(\delta)])} \right) \leq \epsilon \right\} , \tag{4-30}$$

Let $\mathbb{W}^{\text{exp}} = (\widehat{w}^{\text{exp}}(\omega_1), \ldots, \widehat{w}^{\text{exp}}\omega_{n_\omega})$. The experimental observations $y_1^{\text{exp}}(\delta), \ldots, y_{N_{\text{red}}}^{\text{exp}}(\delta)$ corresponding to the random variables $Y_1(\delta), \ldots, Y_{N_{\text{red}}}(\delta)$ are then obtained using the projection defined by Eq. (4-27), that is to say, they are written as

$$y_k^{\text{exp}}(\delta) = \frac{1}{\sqrt{\lambda_k(\delta)}} < (\mathbb{W}^{\text{exp}} - \mathbb{M}(\delta)) , \mathbb{X}^k(\delta) > . \tag{4-31}$$

Let $p_{Y_1,\ldots,Y_{N_{\text{red}}}}(y_1, \ldots, y_{N_{\text{red}}} ; \delta)$ be the joint probability density function of the random variables $Y_1, \ldots, Y_{N_{\text{red}}}$. The log-likelihood function is such that

$$\text{L}^{\text{red}}(\delta) = \log_{10} p_{Y_1,\ldots,Y_{N_{\text{red}}}}(y_1^{\text{exp}}(\delta), \ldots, y_{N_{\text{red}}}^{\text{exp}}(\delta) ; \delta) . \tag{4-32}$$

Random variables $Y_1, \ldots, Y_{N_{\text{red}}}$ are uncorrelated. Assuming that they are independent, the following simplification can be introduced for the log-likelihood function which is then rewritten as

$$\text{L}^{\text{red}}(\delta) = \sum_{k=1}^{N_{\text{red}}} \log_{10} p_{Y_k}(y_k^{\text{exp}}(\delta) ; \delta) , \tag{4-33}$$

in which $p_{Y_k}(y_k ; \delta)$ is the probability density function of random variable $Y_k(\delta)$ which is estimated with the statistical reduction model. The optimization problem is then rewritten as

$$\delta^{\text{opt}} = \arg \max_{\delta \in \mathcal{C}_\delta} \text{L}^{\text{red}}(\delta) . \tag{4-34}$$

4.6 Numerical results of the identification procedure

All the numerical results presented below correspond to the forced response for which the transient part of the response induced by the initial conditions has vanished. The time window is $[t_i, t_f] = [150, 250]$ s. The frequency band of analysis is $B = [0\,, 1.5]$ Hz. The frequency and the time samplings correspond to $n_\omega = 250$ and $n_t = 10\,000$.

Figure 4.12 shows the forced dynamical response of the system without uncertainties (deterministic). Figure 4.12(a) shows the rotation of the bit versus the rotational speed of the bit and Fig. 4.12(b) shows the frequency spectrum of the rotational speed of the bit. This frequency spectrum is going to be used in the stochastic analysis, as explained latter.

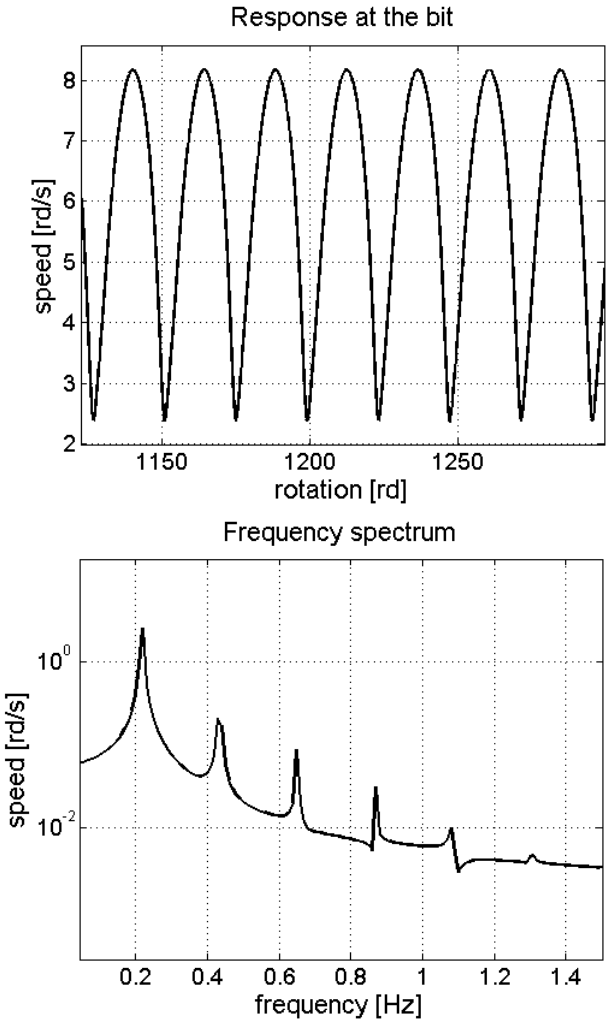

Figure 4.12: (a) rotation of the bit versus rotational speed of the bit and (b) frequency spectrum of the rotational speed of the bit.

There are some measurement equipment that might measure the

dynamics of a real drill-string system, while drilling. Among the measurements, one that is important for the analysis is the rotational speed of the bit. Therefore, this dynamical response is used as observation for the identification procedure and then the frequency spectrum observed $\widehat{W}(\omega,\delta)$ is the frequency spectrum $\widehat{\mathcal{W}}_{\rm bit}(\omega,\delta)$ of the random rotational speed of the bit. The corresponding experiments $\widehat{\mathcal{W}}^{\rm exp}_{\rm bit}(\omega,\delta)$ has been generated numerically for the present analysis. Figure 4.13(a) shows the convergence of the stochastic analysis, where $\mathrm{conv}(n_s) = \frac{1}{n_s}\sum_{i=1}^{n_s}\int_{t_0}^{t_1}||\overline{\mathbf{U}}(t,s_i)||^2 dt$ in which n_s is the number of Monte Carlo simulations.

The trial method is used to solve the optimization problem defined by Eq. (4-34). The stochastic nonlinear dynamical model is solved for δ in $\{0.01, 0.02, 0.03, 0.04, 0.05, 0.06, 0.07, 0.08, 0.09, 0.10\}$. The value of ϵ is set $\epsilon = 1\times 10^{-4}$ yielding $N_{\rm red}$=40 (see Eq. (4-30)). Figure 4.13(b) shows how the log-likelihood $\mathrm{L}^{\rm red}$ (see Eq. (4-33)) varies with the dispersion parameter δ. We conclude that the most likely value for the dispersion parameter $\delta^{\rm opt}$ is 0.06.

Figures 4.14 and 4.15 show the response of the stochastic system for the identified value 0.06 of δ. Figure 4.14(a) shows random realizations of the rotational speed of the bit $\mathcal{W}_{\rm bit}$ and Fig. 4.14(b) shows the coefficient of variation $\delta_W(t) = \sigma_W(t)/\mu_W(t)$ of the random rotational speed of the bit at each time t in which $\sigma_W(t)$ is the standard deviation and $\mu_W(t)$ is the mean value of $\mathcal{W}_{\rm bit}(t)$ at each instant t. Although δ is small (0.06), the coefficient of variation of the response is significant ($\delta_W \sim 0.4$). Figure 4.15 shows the statistical envelope of the frequency spectrum $\widehat{\mathcal{W}}_{\rm bit}$ of the random rotational speed of the bit together with the response of the deterministic system and the mean response of the stochastic system.

4.7 Robust optimization

The aim of this Section is to propose an optimization procedure for the nonlinear dynamics of a drill-string taken into account the uncertainties inherent in the problem. An optimization procedure that considers uncertainties is called robust optimization and its application to dynamical systems is quite recent see, for instance, [12, 136, 20, 119], and also [42]. In a drilling operation, the goal is to drill as fast as possible preserving the integrity of the system, *i.e.*, avoiding failures. In the optimization strategy proposed, the objective function is the mean rate of penetration, and the constraint of the problem is its integrity limits. For

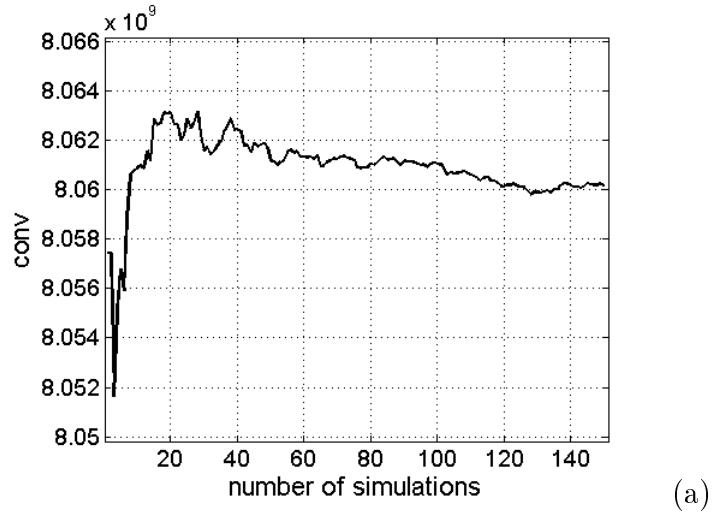

(a)

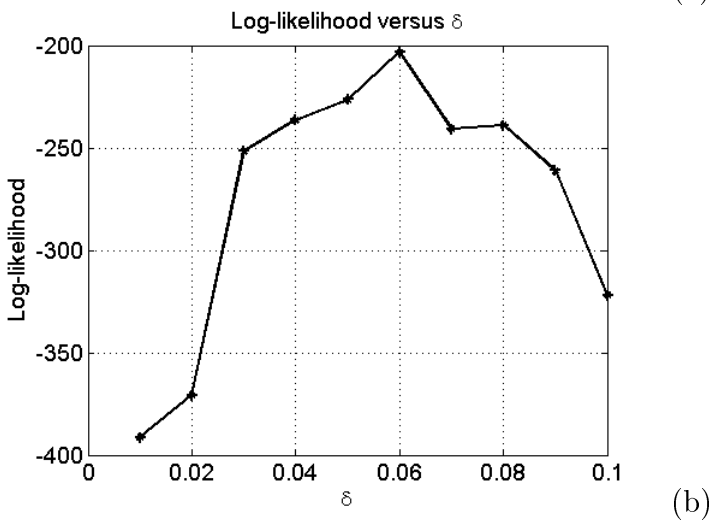

(b)

Figure 4.13: (a) convergence function and (b) log-likelihood function.

the integrity limits of the structure, we use the Von Mises stress, the damage due to fatigue and a stick-slip stability factor. Fatigue is an important factor of failure in a drilling process [70, 131]. The idea is to consider fatigue as a constraint to the optimization analysis without taking into account all the details (for fatigue analysis of a drill-string, see [15, 74]). Thus, the analysis done here is more qualitative than quantitative.

The three parameters that are usually employed to control the drilling process are the rotational speed of the rotary table, the reaction force at the bottom (known as the weight-on-bit) and the fluid pump flow (less important, therefore neglected in the analysis). The value of the weight-on-bit f_{bit} fluctuates; hence it would be difficult to use f_{bit} in the optimization procedure. We propose then to use the initial reaction force at the bit f_c, which is used to calculate the initial prestressed state. The drilling process is stopped after every 10 meters of penetration to assemble another

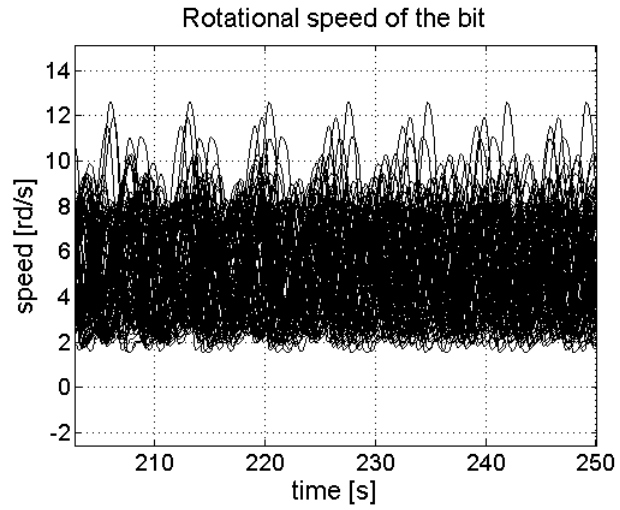

(a)

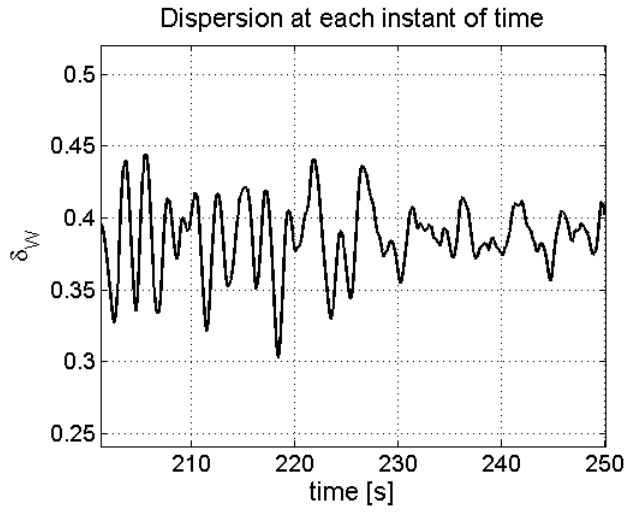

(b)

Figure 4.14: (a) random realizations of the rotational speed of the bit for $\delta = 0.06$ and (b) coefficient of variation of $\mathcal{W}_{\text{bit}}$ at each instant for $\delta = 0.06$.

tube. When the operation is going to re-start, we can choose two parameters: the top speed and the static reaction force at the bit f_c (adjusting the supporting force at the top). Then, the drilling process re-starts and the value of the f_{bit} (which was initially f_c, when there was no movement of the column) now fluctuates. Therefore, the optimization variables used in the robust optimization problem are the rotational speed at the top ω_{RPM} and the initial reaction force at the bit f_c.

Since the goal of this Section is the robust optimization problem, we decided to use a simplified dynamical system to focus the analysis in the robust optimization problem. The simplified model analyzed is discussed in the next subsection. Then, the objective function of the optimization problem is defined, the constraints related to the integrity limits are presented, and the robust optimization is formalized.

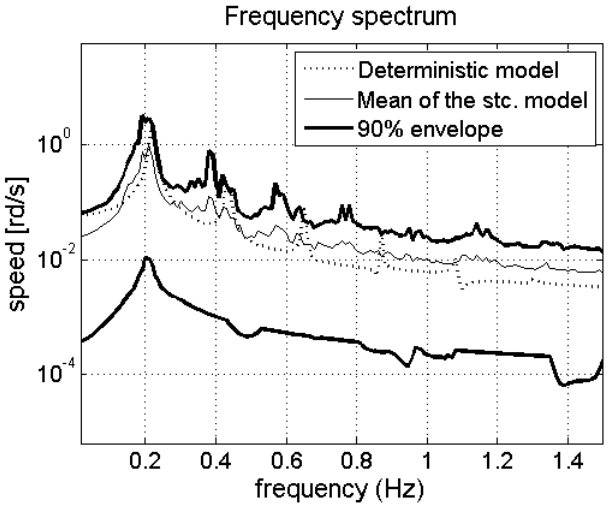

Figure 4.15: 90% statistical envelope of $\widehat{\mathcal{W}}_{\text{bit}}$ for $\delta = 0.06$ together with the deterministic response and the mean of the stochastic response.

4.7.1 Simplified drill-string system

In the simplified model, the fluid-structure interaction model is not taken into account and the computational model is constructed using two-node elements with two degrees of freedom per node (axial and torsional). The finite element approximation of the displacements are then written as

$$u(\xi,t) = \mathbf{N}_u(\xi)\mathbf{u}_e(t)\ ,\ \theta_x(\xi,t) = \mathbf{N}_{\theta_x}(\xi)\mathbf{u}_e(t)\ , \tag{4-35}$$

where u is the axial displacement, θ_x is the rotation about the x-axis, $\xi = x/l_e$ is the element coordinate, $\mathbf{N}$ are the shape function

$$\begin{aligned} \mathbf{N}_u &= [(1-\xi) \quad 0 \quad \xi \quad 0]\,, \\ \mathbf{N}_{\theta_x} &= [0 \quad (1-\xi) \quad 0 \quad \xi]\,, \end{aligned} \tag{4-36}$$

and

$$\mathbf{u}_e = [u_1 \quad \theta_{x1} \quad u_2 \quad \theta_{x2}]^T\,, \tag{4-37}$$

where exponent T means transposition.

The element matrices have dimension 4×4, instead of 12×12. The

element mass matrix is written as:

$$[M]^{(e)} = \int_0^1 \left[\rho A(\mathbf{N}_u^T \mathbf{N}_u + \rho I_p(\mathbf{N}_{\theta_x}^T \mathbf{N}_{\theta_x})\right] l_e d\xi \,. \tag{4-38}$$

The displacement field has to be redefined. The position $\mathbf{X}$ of the reference configuration, the position $\mathbf{x}$ of the deformed configuration, and the displacement field $\mathbf{p}$, all written in the inertial frame of reference, are such that

$$\mathbf{p} = \begin{bmatrix} u_x \\ u_y \\ u_z \end{bmatrix} = \mathbf{x} - \mathbf{X} = \begin{bmatrix} x + u \\ ycos(\theta_x) - zsin(\theta_x) \\ ysin(\theta_x) + zcos(\theta_x) \end{bmatrix} - \begin{bmatrix} x \\ y \\ z \end{bmatrix} \tag{4-39}$$

then,

$$\begin{bmatrix} u_x \\ u_y \\ u_z \end{bmatrix} = \begin{bmatrix} u \\ ycos(\theta_x) - zsin(\theta_x) - y \\ ysin(\theta_x) + zcos(\theta_x) - z \end{bmatrix} . \tag{4-40}$$

Figure 4.16 shows that u_y and u_z are related to the torsion of the drill-string; the lateral displacements of the neutral line of the column are zero ($v = w = 0$).

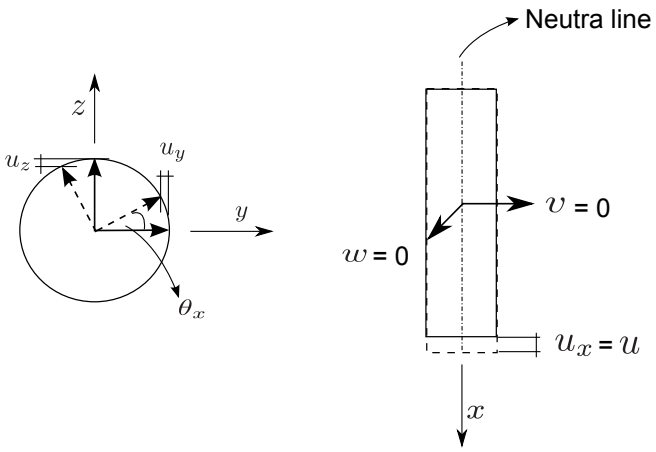

Figure 4.16: Displacement field.

As done before, finite strains are considered, thus the components of

the Green-Lagrange strain tensor, in the simplified model, are written as

$$\begin{aligned}
\epsilon_{xx} &= u_{x,x} + \frac{1}{2}\left(u_{x,x}^2 + u_{y,x}^2 + u_{z,x}^2\right) , \\
\epsilon_{xy} &= \frac{1}{2}\left(u_{y,x} + u_{x,y} + u_{x,x}u_{x,y} + u_{y,x}u_{y,y} + u_{z,x}u_{z,y}\right) , \\
\epsilon_{xz} &= \frac{1}{2}\left(u_{z,x} + u_{x,z} + u_{x,x}u_{x,z} + u_{y,x}u_{y,z} + u_{z,x}u_{z,z}\right) ,
\end{aligned} \tag{4-41}$$

where $u_{x,y} = \partial u_x/\partial y$ and so on. The linear terms yield the stiffness matrix $[K]$ and the higher order terms yield the geometric stiffness matrix $[K_{\mathrm{g}}]$. The element stiffness matrix is written as

$$[K]^{(e)} = \int_0^1 \left[\frac{EA}{l_e}\left(\mathbf{N}_u'^T\mathbf{N}_u'\right) + \frac{GI_p}{l_e}\left(\mathbf{N}_{\theta_x}'^T\mathbf{N}_{\theta_x}'\right)\right] d\xi \,, \tag{4-42}$$

The element geometric stiffness matrix is written as

$$\begin{aligned}
[K_{\mathrm{g}}]^{(e)} = \int_0^1 &\left[\left(\mathbf{N}_u'^T\mathbf{N}_u'\right)\left(3EAu' + 1.5EAu'^2 + \right.\right. \\
&+0.5EI_p\theta_x'^2\big) + \left(\mathbf{N}_u'^T\mathbf{N}_{\theta_x}'\right)\left(EI_p\theta_x' + EI_p\theta_x'u'\right) + \\
&+ \left(\mathbf{N}_{\theta_x}'^T\mathbf{N}_u'\right)\left(EI_p\theta_x' + EI_p\theta_x'u'\right) + \left(\mathbf{N}_{\theta_x}'^T\mathbf{N}_{\theta_x}'\right)\left(EI_pu' + \right. \\
&\left.\left.+0.5EI_pu'^2 + 1.5EI_{p4}\theta_x'^2 + 3EI_{22}\theta_x'^2\right)\right]\frac{1}{l_e}d\xi \,,
\end{aligned} \tag{4-43}$$

where $u' = \mathbf{N}_u'\mathbf{u}_e/l_e$, $\theta_x' = \mathbf{N}_{\theta_x}'\mathbf{u}_e/l_e$, $I_{22} = \int_A (y^2z^2)dA$ and $I_{p4} = \int_A (y^4 + z^4)dA$.

To calculate the initial prestressed state, the fluid force vector is not taken into account,

$$\mathbf{u}_{\mathrm{S}} = [K]^{-1}(\mathbf{f}_{\mathrm{g}} + \mathbf{f}_c) \,. \tag{4-44}$$

Small vibrations about the initial prestressed configuration defined by $\mathbf{u}_{\mathrm{S}}$ are assumed. Therefore, the geometric stiffness matrix $[K_{\mathrm{g}}(\mathbf{u}_{\mathrm{S}})]$ is constant. Introducing $\overline{\mathbf{u}} = \mathbf{u} - \mathbf{u}_{\mathrm{S}}$, the computational dynamical model for

the simplified system is then written as

$$\begin{gathered}[M]\ddot{\overline{\mathbf{u}}}(t)+[C]\dot{\overline{\mathbf{u}}}(t)+([K]+[K_{\mathrm{g}}(\mathbf{u}_{\mathrm{S}})])\overline{\mathbf{u}}(t)= \\ =\mathbf{g}(t)+\mathbf{f}_{\mathrm{bit}}(\dot{\overline{\mathbf{u}}})\,, \\ \overline{\mathbf{u}}(0)=\overline{\mathbf{u}}_0 \quad , \quad \dot{\overline{\mathbf{u}}}(0)=\overline{\mathbf{v}}_0\,,\end{gathered} \tag{4-45}$$

in which $[M]$ and $[K]$ are the mass and stiffness matrices. The proportional damping matrix $[C]=\alpha\,[M]+\beta\,([K]+[K_{\mathrm{g}}(\mathbf{u}_{\mathrm{S}})])$ (α and β are positive constants) is added *a posteriori* in the computational model. The initial conditions are defined by $\overline{\mathbf{u}}_0$ and $\overline{\mathbf{v}}_0$. The force vector related to the bit-rock interaction is $\mathbf{f}_{\mathrm{bit}}$ and the imposed rotation at the top (dirichlet boundary condition) is expressed by $\mathbf{g}$.

As done for the complete model, the system is reduced using the normal modes calculated in the prestressed configuration. The reduced model is written as

$$\begin{gathered}\overline{\mathbf{u}}(t)=[\Phi]\,\mathbf{q}(t)\,, \\ [M_r]\ddot{\mathbf{q}}(t)+[C_r]\dot{\mathbf{q}}(t)+[K_r]\mathbf{q}(t)=[\Phi]^T(\mathbf{g}(t)+\mathbf{f}_{\mathrm{bit}}([\Phi]\,\dot{\mathbf{q}}))\,, \\ \mathbf{q}(0)=\mathbf{q}_0 \quad , \quad \dot{\mathbf{q}}(0)=\mathbf{v}_0\,,\end{gathered} \tag{4-46}$$

in which $\mathbf{q}_0$ and $\mathbf{v}_0$ are the initial conditions and where $[\Phi]$ is the $(m\times n)$ real matrix composed by n normal modes and

$$[M_r]=[\Phi]^T[M][\Phi], \quad [C_r]=[\Phi]^T[C][\Phi]\,,$$

$$[K_r]=[\Phi]^T([K]+[K_{\mathrm{g}}(\mathbf{u}_{\mathrm{S}})])[\Phi] \tag{4-47}$$

are the reduced matrices.

This deterministic reduced computational model defined by Eq. (4-46) has to be replaced by the following stochastic reduced computational model

$$\begin{gathered}\overline{\mathbf{U}}(t)=[\Phi]\,\mathbf{Q}(t)\,, \\ [\mathbf{M}_r]\ddot{\mathbf{Q}}(t)+[\mathbf{C}_r]\dot{\mathbf{Q}}(t)+[\mathbf{K}_r]\mathbf{Q}(t)= \\ =[\Phi]^T\{\mathbf{g}(t)+\mathbf{F}_{\mathrm{bit}}([\Phi]\,\dot{\mathbf{Q}}(t))\}\,, \\ \mathbf{Q}(0)=\mathbf{q}_0 \quad , \quad \dot{\mathbf{Q}}(0)=\mathbf{v}_0\,,\end{gathered} \tag{4-48}$$

where $[\mathbf{M}_r]$, $[\mathbf{K}_r]$ and $[\mathbf{C}_r]$ are the random matrices defined by Section (4.1), $\mathbf{Q}$ is the stochastic process of the generalized coordinates, $\overline{\mathbf{U}}$ is the stochastic

process of the response of the system and $\mathbf{F}_{\text{bit}}$ is the random force related to the bit-rock interaction probabilistic model defined in Section 4.2.

4.7.2 Objective function

The goal of the optimization problem is to find the set of values $\mathbf{s} = (\omega_{\text{RPM}}, f_c)$ that maximizes the expected mean rate of penetration (time average), respecting the integrity limits of the mechanical system. The objective function is defined by

$$J(\mathbf{s}) = \mathcal{E}\left\{\mathcal{R}(\mathbf{s})\right\} , \tag{4-49}$$

where J is the mathematical expectation of the random mean rate $\mathcal{R}$ of penetration which is such that

$$\mathcal{R}(\mathbf{s}) = \frac{1}{t_1 - t_0}\int_{t_0}^{t_1} \dot{U}_{\text{bit}}(\mathbf{s})dt , \tag{4-50}$$

in which (t_0, t_1) is the time interval analyzed and $\dot{U}_{\text{bit}}$ is the random rate of penetration. The constraints related to the integrity limits of the mechanical system are discussed in the next section.

4.7.3 Constraints of the problem (integrity limits)

Three constraints are proposed to represent the integrity of the mechanical system. The first one is the maximum stress value that the structure may resist. If the structure is submitted to a stress greater than the maximum admissible stress, it will fail. The second constraint is the damage cumulated by fatigue. If the damage is greater than one, a crack will occur, what is not desired. The third constraint is a stick-slip factor, since we want to avoid torsional instability and stick-slip.

The first constraint is the maximum Von Mises stress σ (see Appendix I) that must be below the ultimate stress σ_{max} of the material,

$$\max_{\mathbf{x},t}\{\sigma(\mathbf{s}, \mathbf{x}, t)\} \leq \sigma_{\text{max}} , \tag{4-51}$$

where $\mathbf{x} = (x, y, z)$ belongs to the domain Ω_c of the problem (the column). For the stochastic problem this constraint must be true with probability $(1 - P_{\text{risk}})$.

$$\text{Prob}\left\{\max_{\mathbf{x},t}\{\mathfrak{S}(\mathbf{s}, \mathbf{x}, t)\} \leq \sigma_{\max}\right\} \geq 1 - P_{\text{risk}}\,, \tag{4-52}$$

where $\mathfrak{S}$ is the random variable modeling the stress σ in presence of uncertainties in the computational model and P_{risk} represents the risk we are willing to take. The more conservative we are, the lower we set P_{risk}. The second constraint is the damage cumulated due to fatigue d that must be below a given limit $d_{\max}$.

$$\max_{\mathbf{x}}\{d(\mathbf{s}, \mathbf{x})\} \leq d_{\max}\,, \tag{4-53}$$

where d is the cumulated damage related to p_r meters of penetration. The damage $\tilde{d}$ is computed for (t_0, t_1) (see Appendix J) and then, this damage is extrapolated to consider p_r meters of penetration,

$$d = \tilde{d}\left(\frac{p_r}{p_d}\right)\,, \tag{4-54}$$

where p_d is how much it was drilled in (t_0, t_1). For the stochastic problem this constraint must be true with probability $(1 - P_{\text{risk}})$.

$$\text{Prob}\left\{\max_{\mathbf{x}}\{D(\mathbf{s}, \mathbf{x})\} \leq d_{\max}\right\} \geq 1 - P_{\text{risk}}\,. \tag{4-55}$$

where $D(\mathbf{s}, \mathbf{x})$ is the random variable modeling $d(\mathbf{s}, \mathbf{x})$. Sometimes, in the field, engineers use a constraint related to the stick-slip instability. So, finally, the third constraint is the stick-slip stability factor $\mathfrak{ss}$ that must be below a given limit $\mathfrak{ss}_{\max}$,

$$\mathfrak{ss}(\mathbf{s}) \leq \mathfrak{ss}_{\max}\,. \tag{4-56}$$

Factor $\mathfrak{ss}$ is defined by

$$\mathfrak{ss}(\mathbf{s}) = \frac{\omega_{b\max}(\mathbf{s}) - \omega_{b\min}(\mathbf{s})}{\omega_{b\max}(\mathbf{s}) + \omega_{b\min}(\mathbf{s})}\,. \tag{4-57}$$

where $\omega_{b\max}$ is the maximum rotational speed of the bit and $\omega_{b\min}$ is the

minimum rotational speed of the bit for a given time period (t_0, t_1):

$$\begin{aligned} \omega_{b\min}(\mathbf{s}) &= \min_{t\in(t_0,t_1)}\{\omega_{\text{bit}}(\mathbf{s},t)\}\,, \\ \omega_{b\max}(\mathbf{s}) &= \max_{t\in(t_0,t_1)}\{\omega_{\text{bit}}(\mathbf{s},t)\}\,. \end{aligned} \tag{4-58}$$

where ω_{bit} is the rotational speed of the bit. As the amplitude of the torsional vibrations increases, $\mathfrak{ss}$ increases, augmenting the risk of stick-slip (when $\omega_{\text{bit}} = 0$ and then the bit slips). This type of oscillations must be avoided. For the stochastic problem this constraint must be true with probability $(1 - P_{\text{risk}})$.

$$\text{Prob}\left\{\mathcal{S}(\mathbf{s}) \leq \mathfrak{ss}_{\max}\right\} \geq 1 - P_{\text{risk}}\,, \tag{4-59}$$

where $\mathcal{S}(\mathbf{s})$ is the random variable modeling $\mathfrak{ss}(\mathbf{s})$.

In the present analysis, the lateral displacement of the column is neglected. If lateral vibrations were taken into account, a constraint to the radial displacement $r = \sqrt{v^2 + w^2}$ should be considered in which v and w would be the lateral displacements of the neutral line. For example, the column should have radial displacements below a given limit $r_{\max}$, thus $\max_{\mathbf{x},t}\{r(\mathbf{s},\mathbf{x},t)\} \leq r_{\max}$. For the stochastic problem, this constraint should be true with probability $(1 - P_{\text{risk}})$, hence we would have $\text{Prob}\left\{\max_{\mathbf{x},t}\{R(\mathbf{s},\mathbf{x},t)\} \leq r_{\max}\right\} \geq (1 - P_{\text{risk}})$, where R would be the random variable modeling r.

4.7.4 Robust optimization problem

The proposed robust optimization problem aims to maximize the expected mean rate of penetration of the drill-string (see Section 4.7.2), respecting the integrity limits of the mechanical system (see Section 4.7.3). It is written as

$$\begin{aligned} \mathbf{s}^{\text{optm}} &= \arg\ \max_{\mathbf{s}\ \in\ \mathcal{C}}\ J(\mathbf{s})\,, \\ \text{s.t.}\quad &\text{Prob}\left\{\max_{j,t}\{\mathfrak{S}_j(\mathbf{s},t)\} \leq \sigma_{\max}\right\} \geq 1 - P_{\text{risk}}\,, \\ &\text{Prob}\left\{\max_{j}\{D_j(\mathbf{s})\} \leq d_{\max}\right\} \geq 1 - P_{\text{risk}}\,, \\ &\text{Prob}\left\{\mathcal{S}(\mathbf{s}) \leq \mathfrak{ss}_{\max}\right\} \geq 1 - P_{\text{risk}}\,, \end{aligned} \tag{4-60}$$

where the admissible set $\mathcal{C} = \{\mathbf{s} = (\omega_{\mathrm{RPM}}, f_c) : \omega_{\min} \leq \omega_{\mathrm{RPM}} \leq \omega_{\max}\,,\ f_{\min} \leq f_c \leq f_{\max}\}$. The index j represents the points (x_j, y_j, z_j) chosen for the analysis.

This robust optimization problem is not convex and there is no algorithm which allows the global optimum to be surely reached with a finite number of operations. For such an optimization problem, the objective is to improve a given initial solution with an appropriate algorithm and the level of improvement obtained is proportional to the CPU time spent. Several techniques can be used such as random search algorithms [121] (for instance, Latin hypercube sampling type), genetic algorithms [41], local search with random restart points, etc.). Presently, since the dimension of the parameter space is small (2 parameters), a trial approach (which surely allows the initial solution to be improved) is used and is very efficient. The algorithm is then the following. A grid is generated in the parameter space and the stochastic problem is solved for each point of the grid. The points of the grid that do not satisfy the constraints of the optimization problem are eliminated. Then, the optimal point is chosen in the set of all the retained points. The identified region containing this first optimum point can be reanalyzed introducing a new refined grid around this point to improve the solution.

4.8 Numerical results of the robust optimization

The data used in this application are given in the table below.

$L_{\mathrm{dp}} = 1400$ m	length of the drill pipe
$L_{\mathrm{dc}} = 200$ m	length of the drill collar
$D_i = 0.095$ m	inside diameter of the column
$D_{\mathrm{odp}} = 0.12$ m	outside diameter of the drill pipe
$D_{\mathrm{odc}} = 0.15$ m	outside diameter of the drill collar
$E = 210$ GPa	elasticity modulus of the drill string material
$\rho = 7850$ kg/m^3	density of the drill string material
$\nu = 0.29$	poisson coefficient of the drill string material
$g = 9.81$ m/s^2	gravity acceleration

Table 4.1: Data used in this application

The damping matrix is constructed using $[C] = \alpha[M] + \beta([K] + [K_{\mathrm{g}}(\mathbf{u}_{\mathrm{S}})])$ with $\alpha = 0.1$ and $\beta = 0.00008$. The integrity limits are given by $\sigma_{\max} = 650$ MPa, $d_{\max} = 1$ and $\mathfrak{SS}_{\max} = 1.20$. The damage d and the maximum stress value σ are calculated in the critical region of the

drill-pipe, close to the drill-collar: $x = 1400$ m and $y = z = r_0 \cos(\pi/4)$ (where r_0 is the outer radius of the drill-pipe). The damage d is calculated using $p_r = 2000$ m, which means that we allow damage equals to one after 2000 m of penetration. The nonlinear dynamical system analyzed is sensitive to model uncertainties [87], therefore, the probabilistic model is fixed with $\delta_G = 0.005$ and $\delta_M = \delta_C = \delta_K = 0.001$. The drill-string is discretized with 120 finite elements. For the construction of the reduced dynamical model, 7 torsional modes, 4 axial modes and also the two rigid body modes of the structure (axial and torsional) are used. For the time integration procedure, the implicit Newmark integration scheme has been implemented with a predictor and a fix point procedure to equilibrate the system response at each time step. All the numerical results presented below correspond to the stationary response for which the transient part of the response induced by the initial conditions has vanished, $(t_0, t_1) = (60, 100)$ s.

4.8.1 Deterministic response

Some deterministic responses are presented in this Section. Figure 4.17(a) shows the axial displacement of the bit and Fig. 4.17(b) shows the rate of penetration for ω_{RPM}=100 RPM and f_c=100 kN. Figure 4.18 shows the rotational speed of the bit for f_c=100 kN, comparing ω_{RPM}=80 RPM with ω_{RPM}=120 RPM. No stick phase is observed (when ω_{bit}=0), but there are significant oscillations on the rotational speed of the bit that can be dangerous for the system, since it might cause stick-slip and crack initiation due to fatigue. Figure 4.19 shows the force at the bit for ω_{RPM}=100 RPM, comparing f_c=100 kN with f_c=105 kN. Note that the force at the bit fluctuates about the value of f_c. The last result presented is the Von Misses stress for f_c=100 kN and ω_{RPM}=100 RPM (see Fig. 4.20).

In the next two sections the deterministic and the stochastic responses are going to be used to solve the deterministic and the robust optimization problem, respectively.

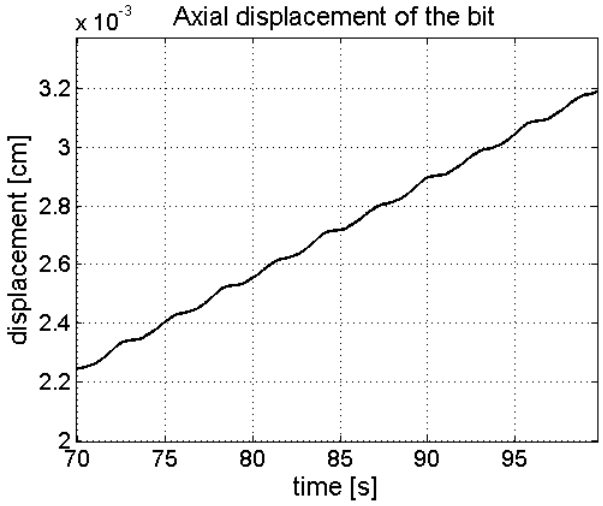

(a)

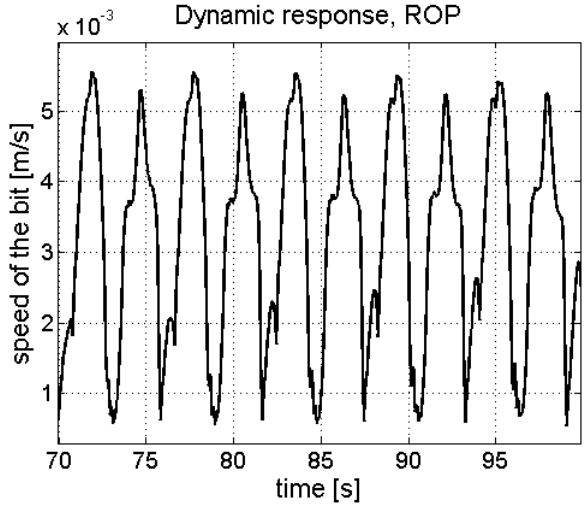

(b)

Figure 4.17: (a) axial displacement of the bit and (b) rate of penetration, for ω_{RPM}=100 RPM and f_c=100 kN.

4.8.2 Results of the deterministic optimization problem

In this section, the deterministic optimization problem is analyzed. For the deterministic problem, Eq. (4-60) is written as

$$\begin{aligned} \mathbf{s}^{\mathrm{optm}} &= \arg \max_{\mathbf{s} \in \mathcal{C}} \; J^{\mathrm{det}}(\mathbf{s}) \,, \\ \text{s.t.} \quad & \max_{j,t}\{\sigma_j(\mathbf{s},t)\} \leq \sigma_{\max} \,, \\ & \max_{j}\{d_j(\mathbf{s})\} \leq d_{\max} \,, \\ & \mathfrak{SS}(\mathbf{s}) \leq \mathfrak{SS}_{\max} \,, \end{aligned} \tag{4-61}$$

where the admissible set $\mathcal{C} = \{\mathbf{s} = (\omega_{\mathrm{RPM}}, f_c) : 80RPM \leq \omega_{\mathrm{RPM}} \leq$

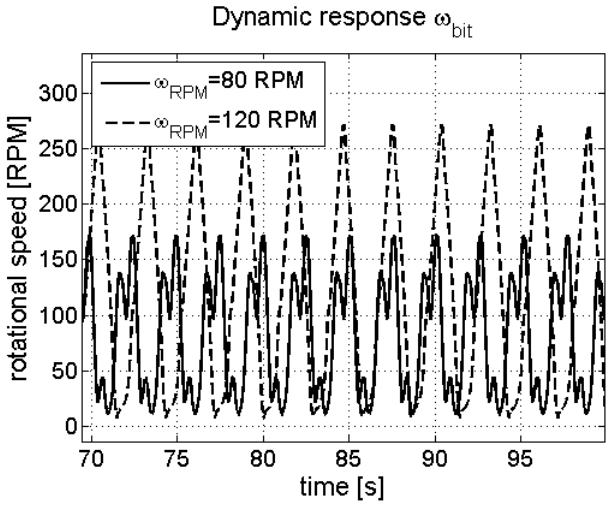

Figure 4.18: Rotational speed of the bit for f_c=100 kN, comparing ω_{RPM}=80 RPM and ω_{RPM}=120 RPM.

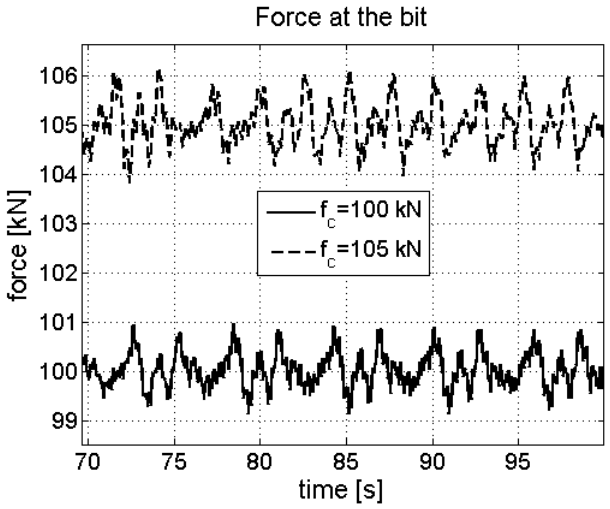

Figure 4.19: Force at the bit for ω_{RPM}=100 RPM, comparing f_c=100 kN and f_c=105 kN.

$120RPM$, $90kN \leq f_c \leq 110kN\}$ and

$$J^{\mathrm{det}}(\mathbf{s}) = \frac{1}{t_1 - t_0} \int_{t_0}^{t_1} \dot{u}_{\mathrm{bit}}(\mathbf{s})\, dt\,, \tag{4-62}$$

where $\dot{u}_{\mathrm{bit}}$ is the deterministic rate of penetration.

Figure 4.21 shows the variation of J^{det} with ω_{RPM} for some values of f_c which are 90, 95, 100, 105 and 110 kN. When ω_{RPM} and f_c increase, J^{det} also increases. Of course, there are side effects: (1) the neutral point will move upwards, (2) the column will be more flexible and (3) the dynamical response is more likely to be unstable.

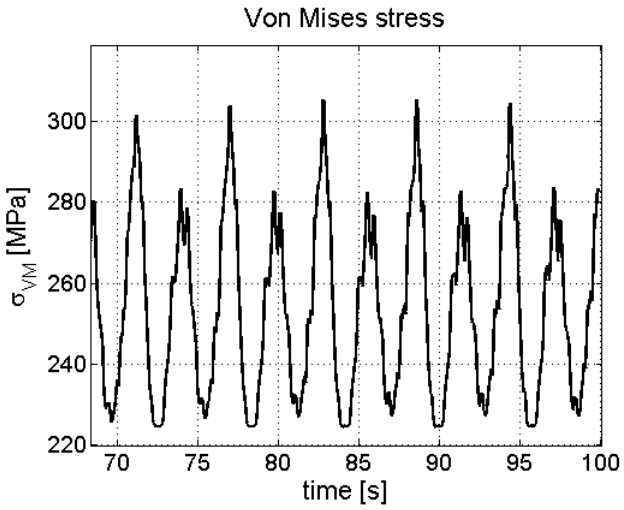

Figure 4.20: Von Misses stress for ω_{RPM}=100 RPM and f_c=100 kN.

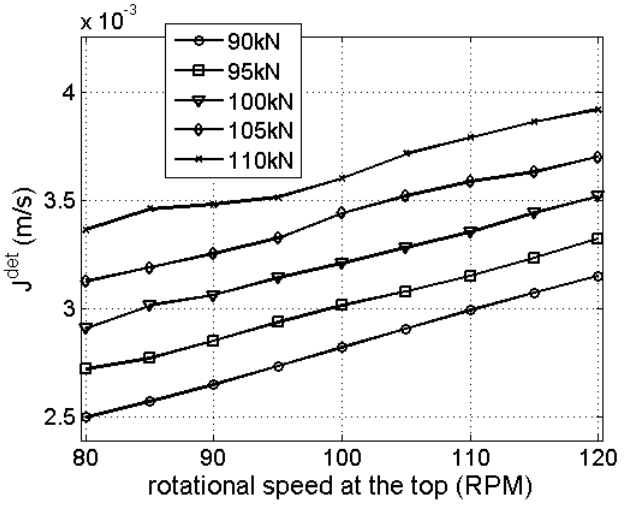

Figure 4.21: Rotational speed at the top versus J^{det} for different f_c (90, 95, 100, 105 and 110 kN).

To proceed with the optimization problem, we eliminate the points $(\omega_{\mathrm{RPM}}, f_c)$ that do not satisfy the integrity limits of the system. For the points simulated, the maximum stress is always below the established limit of $\sigma_{\max} = 650$ MPa. Figure 4.22 shows ω_{RPM} versus the value of the stick-slip factor $\mathfrak{ss}$ and Fig. 4.23 shows ω_{RPM} versus the damage cumulated due to fatigue d for some values of f_c. It can be seen that some points present values greater than the established limits of $\mathfrak{ss}_{\max} = 1.20$ and $d_{\max} = 1$.

The points that do not respect the integrity limits of the system are eliminated. Figure 4.24 summarizes the analysis. The points that are crossed are the ones that do not respect the constraint limits and the best point of the deterministic analysis is identified: $\mathbf{s}^{\mathrm{optm}} = (\omega_{\mathrm{RPM}}$ =120 RPM, f_c =110

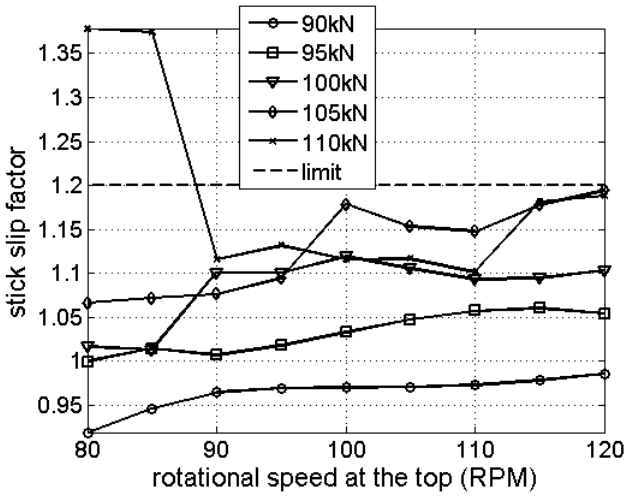

Figure 4.22: Rotational speed at the top versus $\mathfrak{ss}$ for different f_c (90, 95, 100, 105 and 110 kN). The dashed line shows the limit $\mathfrak{ss}_{\max} = 1.20$.

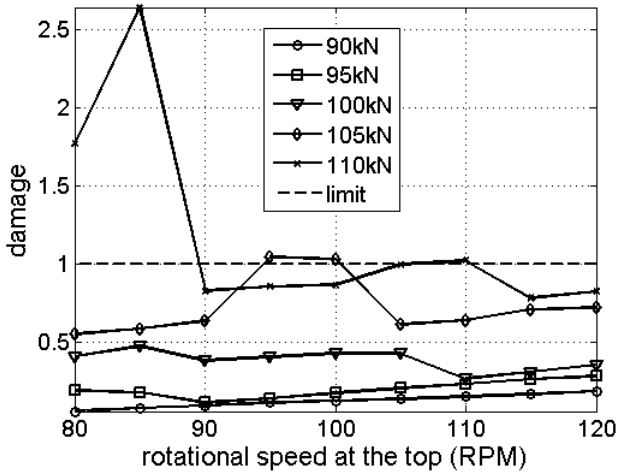

Figure 4.23: Rotational speed at the top versus d for different f_c (90, 95, 100, 105 and 110 kN). The dashed line shows the limit $d_{\max} = 1$.

kN), which gives $J^{\text{det}}_{\text{optm}} = 3.92 \times 10^{-3}$ m/s ~ 14.11 m/h.

In the next section, the results of the robust optimization problem are presented. It will be seen that the results are quite different from the ones presented in this section. The robust analysis considers the 90% percentile of the stick-slip factor, for instance. Therefore, we expect more points to be eliminated in the robust analysis, for example points (ω_{RPM} =120 RPM, f_c =105 kN) and (ω_{RPM} =120 RPM, f_c =110 kN) (see Fig. 4.22), because they are already bearing the limit in the deterministic analysis.

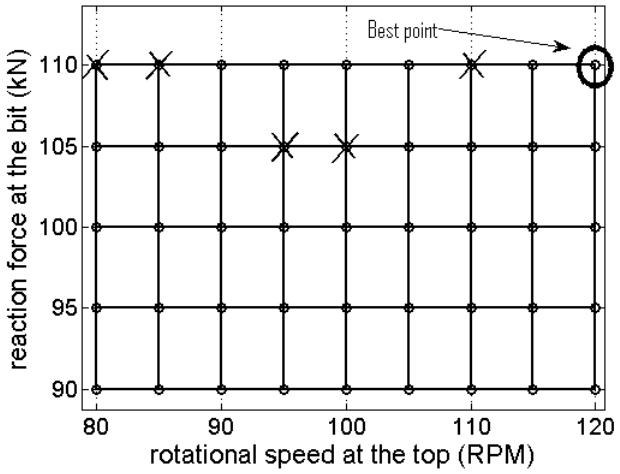

Figure 4.24: Graphic showing the best point $(\omega_{\mathrm{RPM}}, f_c)$ (circle); the crossed points do not respect the integrity limits.

4.8.3 Results of the robust optimization problem

Figure 4.25 shows the convergence of the stochastic analysis, where $\mathrm{conv}(n_s) = \frac{1}{n_s}\sum_{j=1}^{n_s}\int_{t_0}^{t_1}||\overline{\mathbf{U}}(t,s_j)||^2 dt$ (n_s is the number of Monte Carlo simulations).

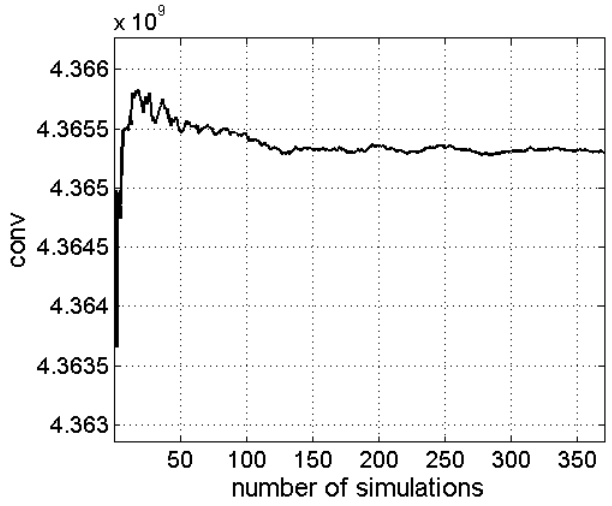

Figure 4.25: Convergence function.

Figure 4.26 shows some random realizations of the rotational speed of the bit.

Figure 4.27 shows the variation of J with ω_{RPM} for some values of f_c which are 90, 95, 100, 105 and 110 kN. As in deterministic case, when ω_{RPM} and f_c increase, J also increases, but the results are different.

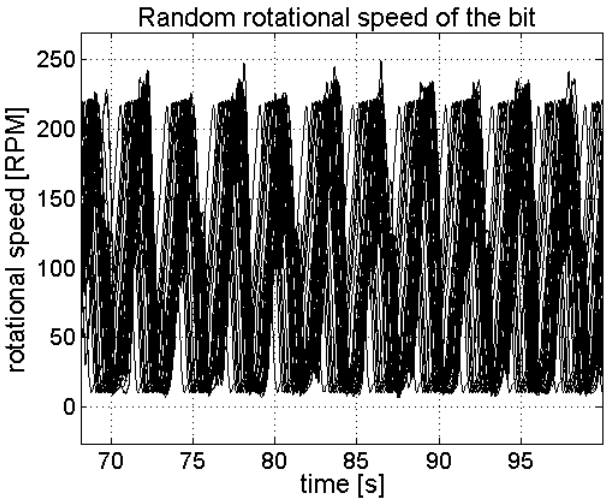

Figure 4.26: Random rotation speed of the bit for ω_{RPM}=100 RPM and f_c=100 kN.

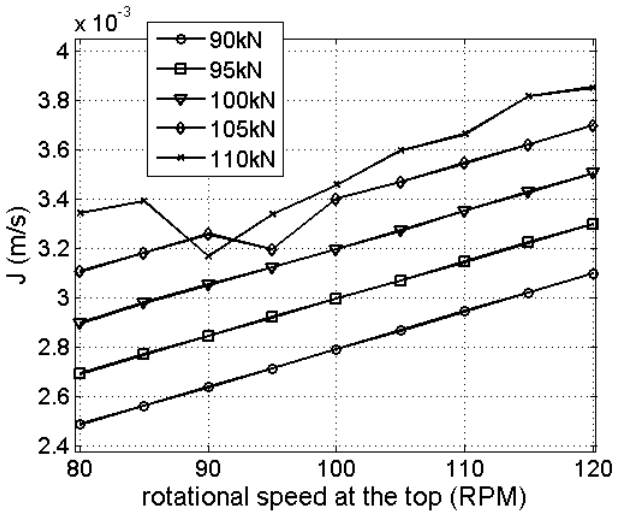

Figure 4.27: Rotational speed at the top versus J for different f_c (90, 95, 100, 105 and 110 kN).

To proceed with the optimization problem, we eliminate the points $(\omega_{\mathrm{RPM}}, f_c)$ that do not satisfy the integrity limits of the system. The constraints are considered in the analysis with $P_{\mathrm{risk}} = 10\%$. For the points simulated, the maximum stress is always below the established limit of $\sigma_{\max} = 650$ MPa. Figure 4.28 shows ω_{RPM} versus the value of the stick-slip factor $\mathcal{S}_{90\%}$ for some values of f_c, where $\mathcal{S}_{90\%}$ is the 90% percentile of random variable $\mathcal{S}$. Figure 4.29 shows ω_{RPM} versus the damage cumulated due to fatigue $D_{90\%}$, where $D_{90\%}$ is the 90% percentile of random variable D. As in the deterministic analysis, it can be seen that some points present values greater than the established limits, but now there are more points in this

situation.

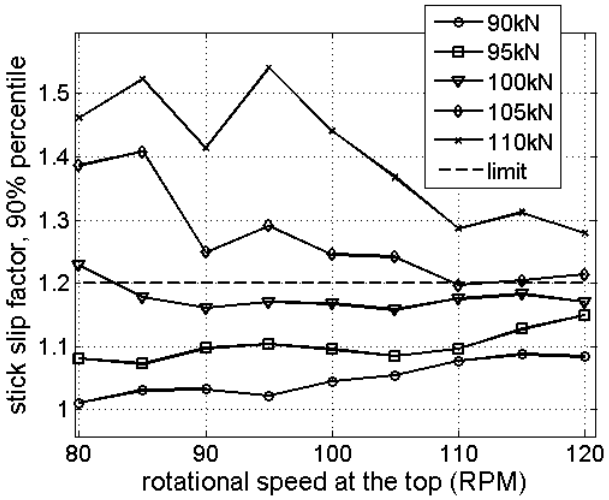

Figure 4.28: Rotational speed at the top versus $\mathcal{S}_{90\%}$ for different f_c (90, 95, 100, 105 and 110 kN). The dashed line shows the limit $\mathfrak{ss}_{\max} = 1.20$.

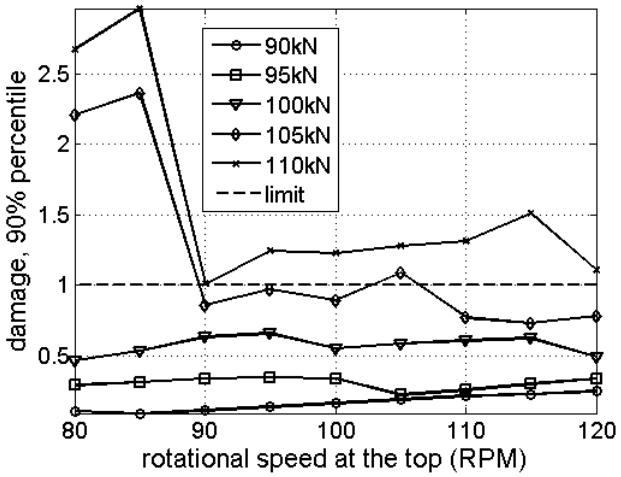

Figure 4.29: Rotational speed at the top versus $D_{90\%}$ for different f_c (90, 95, 100, 105 and 110 kN). The dashed line shows the limit $d_{\max} = 1$.

It can be seen (Figs. 4.28 and 4.29) that the constraints are not respected for high values of ω_{RPM} and f_c. Note that we would like to increase ω_{RPM} and f_c to have a higher J, but to respect the integrity limits these parameters are constrained.

The points that do not respect the integrity limits of the system are eliminated. Figure 4.30 summarizes the analysis. The points that are crossed are the ones that do not respect the constraint limits and the best point of

the robust analysis is identified: $\mathbf{s}^{\mathrm{optm}} = (\omega_{\mathrm{RPM}} = 110$ RPM, $f_c = 105$ kN), which gives $J^{\mathrm{optm}} = 3.54 \times 10^{-3}$ m/s ~ 12.76 m/h.

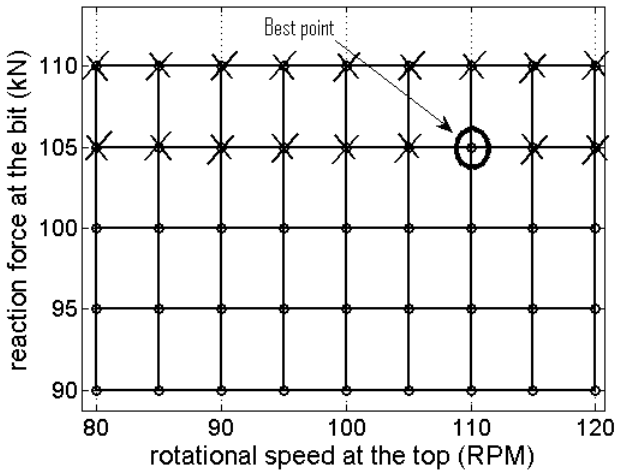

Figure 4.30: Graphic showing the best point $(\omega_{\mathrm{RPM}}, f_c)$ (circle).

It can be concluded that the robust optimization generates different results comparing to the deterministic optimization. If uncertainties are important in the dynamical analysis, we should always proceed with the robust optimization problem, instead of the deterministic optimization problem.

4.9 Summary of the Chapter

A computational nonlinear dynamical model taking into account uncertainties has been developed to simulate the drill-string dynamics. A probabilistic model has been proposed to model uncertainties in the bit-rock interaction model. Since the parameters of the deterministic model of the bit-rock interaction do not correspond to physical parameters, these parameters are not adequate to the use of the parametric probabilistic approach. Then, the nonparametric probabilistic approach has been used. This corresponds to a novel approach to take into account model uncertainties in a nonlinear constitutive equation. Since the dynamical system is globally nonlinear, an adapted strategy has been developed to implement a stochastic solver. The parametric numerical analysis performed shows that the nonlinear dynamical responses of this type of mechanical system is very sensitive to uncertainties in the bit-rock interaction model. In addition, these uncertainties play an important role in the coupling between

the axial responses and the torsional one, and consequently, play a role in the lateral responses.

The nonparametric probabilistic approach has been used as well to model uncertainties in the mass, stiffness and damping operators. This approach takes into account both system-parameter and model uncertainties, which is is an important feature since a simplified mechanical model is employed in the analysis.

With the stochastic model in hands, a procedure has been developed to identify the probabilistic model related to the uncertainties of the bit-rock interaction model. The Maximum Likelihood has been used together with a statistical reduction in the frequency domain using the Principal Component Analysis.

Finally, a methodology for the robust optimization (the ultimate goal of the stochastic model) of the nonlinear dynamics of a drill-string system has been proposed. Applications of robust optimization in dynamical systems are quite recent. The aim of this optimization problem is to maximize the expected mean rate of penetration of the drill-string, respecting the integrity limits. Three constraints have been proposed to represent the integrity of the system: (1) the ultimate stress of the material, (2) the damage cumulated by fatigue and (3) a stick-slip factor. The parameters of the optimization problem, which are the initial reaction force at the bit and the rotational speed at the top, have been considered deterministic. A trial approach has been applied for the optimization problem and the best combination of these two parameters has been found.

5
Summary, future works and publications

We have analyzed the nonlinear dynamics of a drill-string taking into account uncertainties. We may summarize what has been done:

1. Development of a mathematical-mechanical model for the drill-string dynamics. It includes nonlinear Timoshenko beam theory, bit-rock interaction, fluid-structure interaction, impact and rubbing.

2. Development of a computational code using the software MATLAB®. Discretization by means of the Finite Element Method and numerical integration of the discretized system of equations in time.

3. Modeling of uncertainties of the system operators and of the nonlinear constitutive equations of the bit-rock interaction model using the nonparametric probabilistic approach. (Maximum Entropy Principle to construct the probabilistic model).

4. Stochastic simulation using the Monte Carlo method.

5. Development of a procedure to identify the probabilistic model of the uncertain bit-rock interaction model. The Maximum Likelihood Method has been applied together with a statistical reduction (using the Principal Component Analysis).

6. Robust optimization of the operational variables of the drilling process, considering uncertainties and integrity constraints.

However, there is still much work to be done, such as:

1. Experimental identification. Use the field dynamical response to identify the model parameters (deterministic and probabilistic models).

2. Experimental validation. Use data from a real drill-string and compare experimental and numerical dynamical responses.

3. Use data to update the probabilistic model.

4. Control strategy. Develop a control strategy for the drilling process.

5. Directional drilling. Analyze, for instance, a curved drill-string or an horizontal drilling (in our model we consider only a vertical well).

Concerning publications, we have published eight conference papers: [85, 88, 89, 90, 91, 92, 93, 94]. During the period of the thesis I had the chance to present papers in several international conferences, such as ECCOMAS/WCCM (Venice, Italy), COMPDYN (Rhodes, Greece), USD (Sheffield, England), IDETC (San Diego, United States of America), COBEM (Gramados RS, Brazil) and PACAM (Foz do Iguaçu PR, Brazil).

We have published three journal papers, see [87, 95, 96]:

"Nonlinear dynamics of a drill-string with uncertain model of the bit-rock interaction"; T. G. Ritto, C. Soize and R. Sampaio. International Journal of Non-Linear Mechanics, 44(8), pp. 865–876, 2009.

"Robust optimization of the rate of penetration of a drill-string using a stochastic nonlinear dynamical model"; T. G. Ritto, C. Soize and R. Sampaio. Computational Mechanics, 45(5), pp. 415–427, 2010.

"Stochastic dynamics of a drill-string with uncertain weight-on-hook"; T. G. Ritto, C. Soize and R. Sampaio. Journal of the Brazilian Society of Mechanical Sciences and Engineering, 2010. *Accepted*.

We are still working on other publications. It should be remarked that during the period of this thesis other works have been developed besides the work of the thesis, which have originated five journal papers, see [86, 99, 19, 38, 97]:

"Timoshenko beam with uncertainty on the boundary conditions"; T. G. Ritto, R. Sampaio and E. Cataldo. Journal of the Brazilian Society of Mechanical Sciences and Engineering, 30(4) pp. 295–303, 2008.

"Reduced model of a bar impacting an obstacle using the Karhunen-Loève basis"; F. S. Buezas, T. G. Ritto and R. Sampaio. Mecánica Computacional, XXVII, pp. 2195–2219, 2008.

"Comparison and evaluation of two approaches of uncertainty modeling in dynamical systems"; R. Sampaio, T. G. Ritto and E. Cataldo. Mecánica Computacional, XXVI, pp. 3078–3094, 2007.

"Stochastic analysis of a cracked rod modeled via the spectral element method"; A. T. Fabro, T. G. Ritto, R. Sampaio and J. R. F. Arruda. Mechanics Research Communications, 37 pp. 326–331, 2010.

"Robust optimization of a flexible rotor-bearing system using the Campbell diagram"; T. G. Ritto, R. H. Lopez, R. Sampaio and J. E. Souza de Cursi. Engineering Optimization, 2010. *Accepted*.

A
Shape functions

Linear shape functions are used for the axial and torsional displacements, and the shape functions for the lateral displacements are derived by calculating the static response of the beam [77, 8]:

$$\mathbf{N}_u = [(1-\xi) \quad 0 \quad 0 \quad 0 \quad 0 \quad 0 \quad \xi \quad 0 \quad 0 \quad 0 \quad 0 \quad 0]\,,$$

$$\mathbf{N}_v = [0 \quad N_{w1} \quad -N_{w2} \quad 0 \quad 0 \quad 0 \quad 0 \quad N_{w3} \quad -N_{w4} \quad 0 \quad 0 \quad 0]\,,$$

$$\mathbf{N}_w = [0 \quad 0 \quad 0 \quad N_{w1} \quad N_{w2} \quad 0 \quad 0 \quad 0 \quad 0 \quad N_{w3} \quad N_{w4} \quad 0]\,,$$

$$\mathbf{N}_{\theta_x} = [0 \quad 0 \quad 0 \quad 0 \quad 0 \quad (1-\xi) \quad 0 \quad 0 \quad 0 \quad 0 \quad 0 \quad \xi]\,,$$

$$\mathbf{N}_{\theta_y} = [0 \quad 0 \quad 0 \quad N_{\theta1} \quad N_{\theta2} \quad 0 \quad 0 \quad 0 \quad 0 \quad N_{\theta3} \quad N_{\theta4} \quad 0]\,,$$

$$\mathbf{N}_{\theta_z} = [0 \quad -N_{\theta1} \quad N_{\theta2} \quad 0 \quad 0 \quad 0 \quad 0 \quad -N_{\theta3} \quad N_{\theta4} \quad 0 \quad 0 \quad 0]\,,$$

where ξ is the element coordinate ($\xi = x/l_e$) and:

$$N_{w1} = \tfrac{1}{1+\varphi}\left(1 - 3\xi^2 + 2\xi^3 + \varphi\,(1-\xi)\right)\,,$$

$$N_{w2} = \tfrac{l_e}{1+\varphi}\left(-\xi + 2\xi^2 - \xi^3 + \tfrac{\varphi}{2}\,(\xi^2 - \xi)\right)\,,$$

$$N_{w3} = \tfrac{1}{1+\varphi}\left(3\xi^2 - 2\xi^3 + \varphi\xi\right)\,,$$

$$N_{w4} = \tfrac{l_e}{1+\varphi}\left(\xi^2 - \xi^3 + \tfrac{\varphi}{2}\,(\xi - \xi^2)\right)\,,$$

$$N_{\theta1} = \tfrac{1}{(1+\varphi)l_e}\left(6\xi - 6\xi^2\right)\,,$$

$$N_{\theta2} = \tfrac{1}{1+\varphi}\left(1 - 4\xi + 3\xi^2 + \varphi\,(1-\xi)\right)\,,$$

$$N_{\theta3} = \tfrac{1}{(1+\varphi)l_e}\left(-6\xi + 6\xi^2\right)\,,$$

$$N_{\theta4} = \tfrac{1}{1+\varphi}\left(-2\xi + 3\xi^2 + \varphi\xi\right)\,.$$

with $\varphi = \dfrac{12EI}{k_s GA(l_e)^2}$. Where E is the elasticity modulus, I is the area moment of inertia (y-z plane), k_s is shearing factor, G is the shear modulus, A is the cross-sectional area and l_e is the length of an element.

These shape functions are such that shear locking [76] is avoided.

B
Strain

This appendix presents a brief explanation of the deduction of the strain tensor. A more de tailed material can be found in, for instance, [100].

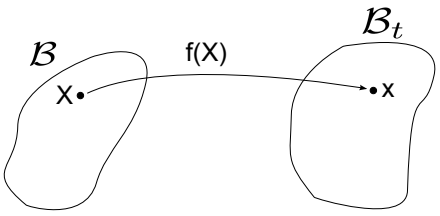

Figure B.1: The position $\mathbf{X}$ maps to $\mathbf{x}$.

Figure B.1 shows the function $\mathbf{f}$ that maps points in the configuration $\mathcal{B}$ (non-deformed configuration) to the configuration $\mathcal{B}_t$. We can write $\mathbf{X} \mapsto \mathbf{x} = \mathbf{f}(\mathbf{X})$, where $\mathbf{X}$ is the position in the non-deformed configuration and $\mathbf{x}$ is the position in the deformed configuration. The displacement field relative to the configuration $\mathcal{B}$ is defined as:

$$\mathbf{p}(\mathbf{X}) = \mathbf{f}(\mathbf{X}) - \mathbf{X} \quad \text{or} \quad \mathbf{f}(\mathbf{X}) = \mathbf{X} + \mathbf{p}(\mathbf{X})\,. \tag{B-1}$$

The deformation gradient tensor is defined as:

$$[F(\mathbf{X})] = \nabla \mathbf{f}(\mathbf{X})\,. \tag{B-2}$$

Then,

$$[F(\mathbf{X})] = \nabla \mathbf{X} + \nabla \mathbf{p}(\mathbf{X}) = [I] + \nabla \mathbf{p}(\mathbf{X})\,, \tag{B-3}$$

where $[I]$ is the identity matrix. The displacement gradient is given by:

$$[\nabla \mathbf{p}(\mathbf{X})] = \begin{pmatrix} \frac{\partial u_x}{\partial x} & \frac{\partial u_x}{\partial y} & \frac{\partial u_x}{\partial z} \\ \frac{\partial u_y}{\partial x} & \frac{\partial u_y}{\partial y} & \frac{\partial u_y}{\partial z} \\ \frac{\partial u_z}{\partial x} & \frac{\partial u_z}{\partial y} & \frac{\partial u_z}{\partial z} \end{pmatrix} . \tag{B-4}$$

Considering a point $\mathbf{X} + d\mathbf{X}$ in the configuration $\mathcal{B}$ and linearizing $\mathbf{f}$ about $\mathbf{X}$, we can write

$$\mathbf{f}(\mathbf{X} + d\mathbf{X}) = \mathbf{f}(\mathbf{X}) + \nabla \mathbf{f}(\mathbf{X})(\mathbf{X} + d\mathbf{X} - \mathbf{X}) , \tag{B-5}$$

$$\mathbf{f}(\mathbf{X} + d\mathbf{X}) - \mathbf{f}(\mathbf{X}) = [F(\mathbf{X})]d\mathbf{X} , \tag{B-6}$$

$$\mathbf{x} + d\mathbf{x} - \mathbf{x} = [F(\mathbf{X})]d\mathbf{X} , \tag{B-7}$$

Finally,

$$d\mathbf{x} = [F(\mathbf{X})]d\mathbf{X} . \tag{B-8}$$

One possible measure for the deformation of the fiber $d\mathbf{X}$, when it is deformed to $d\mathbf{x}$, can be calculated as

$$d\mathbf{x}\cdot d\mathbf{x} - d\mathbf{X}\cdot d\mathbf{X} = ([F]^T[F])d\mathbf{X}\cdot d\mathbf{X} - d\mathbf{X}\cdot d\mathbf{X} = ([F]^T[F] - [I])d\mathbf{X}\cdot d\mathbf{X} = 2[E]d\mathbf{X}\cdot d\mathbf{X} , \tag{B-9}$$

where $[E]$ is the strain tensor, which is given by

$$[E] = \frac{1}{2}([F]^T[F] - [I]) . \tag{B-10}$$

Using $[F] = [I] + \nabla \mathbf{p}$, we have

$$[E] = \frac{1}{2}[([I] + \nabla \mathbf{p})^T([I] + \nabla \mathbf{p}) - [I]] = \frac{1}{2}[\nabla \mathbf{p} + \nabla \mathbf{p}^T + \nabla \mathbf{p}^T \nabla \mathbf{p}] , \tag{B-11}$$

and the components are given by

$$[E]_{ij} = \frac{1}{2}\left(\frac{\partial u_i}{\partial \mathbf{X}_j} + \frac{\partial u_j}{\partial \mathbf{X}_i} + \frac{\partial u_k}{\partial \mathbf{X}_i}\frac{\partial u_k}{\partial \mathbf{X}_j}\right) . \tag{B-12}$$

For example, $[E]_{12} = \frac{1}{2}\left(\frac{\partial u_x}{\partial y} + \frac{\partial u_y}{\partial x} + \frac{\partial u_x}{\partial x}\frac{\partial u_x}{\partial y} + \frac{\partial u_y}{\partial x}\frac{\partial u_y}{\partial y} + \frac{\partial u_z}{\partial x}\frac{\partial u_z}{\partial y}\right)$.

C
Nonlinear forces due to the strain energy

The nonlinear force element vector due to the strain energy is written as shown in Eq. (3-26):

$$(\mathbf{f}_{se})^{(e)} = \int_0^1 \Big[\mathbf{N}_u'^T f_1 + \mathbf{N}_v'^T f_2 + \mathbf{N}_w'^T f_3 + \mathbf{N}_{\theta_x}'^T f_4 + \mathbf{N}_{\theta_y}'^T f_5 + \\ + \mathbf{N}_{\theta_z}'^T f_6 + \mathbf{N}_{\theta_x}^T f_7 + \mathbf{N}_{\theta_y}^T f_8 + \mathbf{N}_{\theta_z}^T f_9\Big]\, l^e d\xi \,,$$

where this organization is chosen in a way that its computation is fast. $f_1, .., f_9$ are written as:

$$\begin{aligned} f_1 &= k_s GA\left(((\theta_y^e)^2 + (\theta_z^e)^2)(1 + (u^e)') + \theta_y^e((w^e)'\cos(\theta_x^e) - (v^e)'\sin(\theta_x^e)) + \right. \\ &- \theta_z^e((v^e)'\cos(\theta_x^e) + (w^e)'\sin(\theta_x^e))) + EI\left((\theta_x^e)'^2(1 + (u^e)') + \right. \\ &+ \frac{3}{2}(\theta_y^e)'^2(1 + (u^e)') + \frac{3}{2}(\theta_z^e)'^2(1 + (u^e)') + (\theta_x^e)'((v^e)'((\theta_z^e)'\sin(\theta_x^e)) + \\ &\left.\left. - (\theta_y^e)'\cos(\theta_x^e)) - (w^e)'((\theta_z^e)'\cos(\theta_x^e) + (\theta_y^e)'\sin(\theta_x^e)))\right) + \right. \\ &+ AE\left(\frac{3}{2}(u^e)'^2 + \frac{1}{2}(u^e)'^3 + \frac{1}{2}(v^e)'^2(1 + (u^e)') + \frac{1}{2}(w^e)'^2(1 + (u^e)')\right), \end{aligned} \tag{B1}$$

$$\begin{aligned} f_2 &= k_s GA\left(-\theta_z^e\cos(\theta_x^e)(1 + (u^e)') - \theta_y^e\sin(\theta_x^e)(1 + (u^e)')\right) + \\ &+ EI\left((v^e)'(2(\theta_x^e)'^2 + \frac{1}{2}(\theta_y^e)'^2 + \frac{1}{2}(\theta_z^e)'^2) - (\theta_x^e)'(\theta_y^e)'\cos(\theta_x^e)(1 + (u^e)') + \right. \\ &+ (\theta_x^e)'(\theta_z^e)'\sin(\theta_x^e)(1 + (u^e)')) + AE(v^e)'\left((u^e)' + \frac{1}{2}(u^e)'^2 + \frac{1}{2}(w^e)'^2 + \right. \\ &\left.\left. + \frac{1}{2}(v^e)'^2\right)\right), \end{aligned}$$

(B2)

$$f_3 = k_s GA\left(\theta_y^e \cos(\theta_x^e)(1+(u^e)') - \theta_z^e \sin(\theta_x^e)(1+(u^e)')\right) +$$
$$+EI\left((w^e)'(2(\theta_x^e)'^2 + \frac{1}{2}(\theta_y^e)'^2 + \frac{1}{2}(\theta_z^e)'^2) - (\theta_x^e)'(\theta_z^e)'\cos(\theta_x^e)(1+(u^e)') + \right.$$
$$\left. -(\theta_x^e)'(\theta_y^e)'\sin(\theta_x^e)(1+(u^e)')\right) + AE(w^e)'\left((u^e)' + \frac{1}{2}(u^e)'^2 + \frac{1}{2}(v^e)'^2 + \right.$$
$$\left. +\frac{1}{2}(w^e)'^2\right),$$

(B3)

$$f_4 = k_s GI\left(-\theta_y^e(\theta_z^e)' + \theta_z^e(\theta_y^e)'\right) + (EI_2 + EI_4)(\theta_x^e)'\left((\theta_x^e)'^2 + \frac{1}{2}(\theta_z^e)'^2 + \right.$$
$$\left. + \frac{1}{2}(\theta_y^e)'^2\right) + EI\left((\theta_x^e)'(2(u^e)' + (u^e)'^2 + 2(v^e)'^2 + 2(w^e)'^2) + \right.$$
$$+(v^e)'(\theta_z^e)'\sin(\theta_x^e)(1+(u^e)') - (v^e)'(\theta_y^e)'\cos(\theta_x^e)(1+(u^e)') +$$
$$\left. -(w^e)'(\theta_y^e)'\sin(\theta_x^e)(1+(u^e)') - (w^e)'(\theta_z^e)'\cos(\theta_x^e)(1+(u^e)')\right).$$

(B4)

At this point we should define the area moments of inertia I_2 and I_4.

$$I_2 = \int_A y^2 z^2 dA\,,$$

$$I_4 = \int_A y^4 dA = \int_A z^4 dA\,.$$

Back to the functions:

$$f_5 = k_s GI\left((\theta_x^e)'\theta_z^e + (\theta_y^e)'(\theta_y^e)^2 + (\theta_y^e)'(\theta_z^e)^2\right) + EI_2(\theta_y^e)'\left(\frac{1}{2}(\theta_x^e)'^2 + \frac{3}{2}(\theta_z^e)'^2\right) +$$
$$+EI_4(\theta_y^e)'\left(\frac{1}{2}(\theta_x^e)'^2 + \frac{1}{2}(\theta_y^e)'^2\right) + EI\left(-(v^e)'(\theta_x^e)'\cos(\theta_x^e)(1+(u^e)') + \right.$$
$$\left. -(w^e)'(\theta_x^e)'\sin(\theta_x^e)(1+(u^e)') + (\theta_y^e)'(3(u^e)' + \frac{3}{2}(u^e)'^2 + \frac{1}{2}(v^e)'^2 + \frac{1}{2}(w^e)'^2)\right),$$

(B5)

$$f_6 = k_s GI\left((\theta_x^e)'\theta_y^e + (\theta_z^e)'(\theta_z^e)^2 + (\theta_z^e)'(\theta_y^e)^2\right) + EI_2(\theta_z^e)'\left(\frac{1}{2}(\theta_x^e)'^2 + \frac{3}{2}(\theta_y^e)'^2\right) +$$
$$+EI_4(\theta_z^e)'\left(\frac{1}{2}(\theta_x^e)'^2 + \frac{1}{2}(\theta_z^e)'^2\right) + EI\left(-(w^e)'(\theta_x^e)'\cos(\theta_x^e)(1+(u^e)')+\right.$$
$$\left.+(v^e)'(\theta_x^e)'\sin(\theta_x^e)(1+(u^e)') + (\theta_z^e)'(3(u^e)' + \frac{3}{2}(u^e)'^2 + \frac{1}{2}(v^e)'^2 + \frac{1}{2}(w^e)'^2)\right) ,$$

(B6)

$$f_7 = k_s GA\left(-(w^e)'\theta_z^e\cos(\theta_x^e)(1+(u^e)') - (w^e)'\theta_y^e\sin(\theta_x^e)(1+(u^e)') +\right.$$
$$+(v^e)'\theta_z^e\sin(\theta_x^e)(1+(u^e)') - (v^e)'\theta_z^e\cos(\theta_x^e)(1+(u^e)')) +$$
$$+EI(\theta_x^e)'\left((v^e)'(\theta_z^e)'\cos(\theta_x^e)(1+(u^e)') + (v^e)'(\theta_y^e)'\sin(\theta_x^e)(1+(u^e)') +\right.$$
$$\left.-(w^e)'(\theta_y^e)'\cos(\theta_x^e)(1+(u^e)') + (w^e)'(\theta_z^e)'\sin(\theta_x^e)(1+(u^e)')\right) ,$$

(B7)

$$f_8 = k_s GI\left(\theta_y^e(\theta_y^e)'^2 + \theta_y^e(\theta_z^e)'^2 - (\theta_z^e)'(\theta_x^e)'\right) + k_s GA\left(\theta_y^e(u^e)'(2+(u^e)') +\right.$$
$$\left.-(v^e)'\sin(\theta_x^e)(1+(u^e)') + (w^e)'\cos(\theta_x^e)(1+(u^e)')\right) ,$$

(B8)

$$f_9 = k_s GI\left(\theta_z^e(\theta_z^e)'^2 + \theta_z^e(\theta_y^e)'^2 + (\theta_y^e)'(\theta_x^e)'\right) + k_s GA\left(\theta_z^e(u^e)'(2+(u^e)') +\right.$$
$$\left.-(w^e)'\sin(\theta_x^e)(1+(u^e)') - (v^e)'\cos(\theta_x^e)(1+(u^e)')\right) .$$

(B9)

D
Time integration

An implicit Newmark scheme with a fix point procedure is used for the numerical integration in time. The following assumption is used [6]:

$$\begin{aligned} \frac{\dot{\mathbf{q}}^{(t+\Delta t)} - \dot{\mathbf{q}}^{(t)}}{\Delta t} &= (1-\delta_{\mathrm{NM}})\ddot{\mathbf{q}}^{(t)} + \delta_{\mathrm{NM}}\ddot{\mathbf{q}}^{(t+\Delta t)}\,, \\ \dot{\mathbf{q}}^{(t+\Delta t)} &= \dot{\mathbf{q}}^{(t)} + [(1-\delta_{\mathrm{NM}})\ddot{\mathbf{q}}^{(t)} + \delta_{\mathrm{NM}}\ddot{\mathbf{q}}^{(t+\Delta t)}]\Delta t\,, \end{aligned} \tag{D-1}$$

and

$$\begin{aligned} \frac{\mathbf{q}^{(t+\Delta t)} - \mathbf{q}^{(t)}}{\Delta t} &= \dot{\mathbf{q}}^{(t)} + [(0.5-\alpha_{\mathrm{NM}})\ddot{\mathbf{q}}^{(t)} + \alpha_{\mathrm{NM}}\ddot{\mathbf{q}}^{(t+\Delta t)}]\Delta t \\ \mathbf{q}^{(t+\Delta t)} &= \mathbf{q}^{(t)} + \dot{\mathbf{q}}^{(t)}\Delta t + [(0.5-\alpha_{\mathrm{NM}})\ddot{\mathbf{q}}^{(t)} + \alpha_{\mathrm{NM}}\ddot{\mathbf{q}}^{(t+\Delta t)}]\Delta t^2\,. \end{aligned} \tag{D-2}$$

For an unconditionally stable scheme, we set $\delta_{\mathrm{NM}} = 0.5$ and $\alpha_{\mathrm{NM}} = 0.25$. The first step of the numerical integration is to do the preliminary computations:

$$\begin{aligned} &b_0 = \frac{1}{\alpha_{\mathrm{NM}}\Delta t^2}\,, \qquad b_1 = \frac{\delta_{\mathrm{NM}}}{\alpha_{\mathrm{NM}}\Delta t}\,, \quad b_2 = \frac{1}{\alpha_{\mathrm{NM}}\Delta t}\,, \\ &b_3 = \frac{1}{2+\alpha_{\mathrm{NM}}} - 1\,, \quad b_4 = \frac{\delta_{\mathrm{NM}}}{\alpha_{\mathrm{NM}}} - 1\,, \quad b_5 = \frac{\Delta t}{2}\left(\frac{\delta_{\mathrm{NM}}}{\alpha_{\mathrm{NM}}} - 2\right)\,, \\ &b_6 = \Delta t(1-\delta_{\mathrm{NM}})\,, \quad b_7 = \delta_{\mathrm{NM}}\Delta t\,. \end{aligned} \tag{D-3}$$

and calculate the effective stiffness matrix

$$[K_{\mathrm{eff}}] = [K_r] + b_0[M_r] + b_1[C_r]\,. \tag{D-4}$$

The second step of the numerical integration is to perform the Newmark

scheme to calculate the predictor that will be used in the fix point procedure. The algorithm is given as following.

1. Enter $\mathbf{q}^{(t)}$, $\dot{\mathbf{q}}^{(t)}$, $\ddot{\mathbf{q}}^{(t)}$.

2. Calculate the effective loads at time $(t+\Delta t)$:

$\mathbf{f}_{\text{eff}}^{(t+\Delta t)} = \mathbf{f}_{\text{lin}}{}^{(t+\Delta t)} + [M_r](b_0\mathbf{q}^{(t)} + b_2\dot{\mathbf{q}}^{(t)} + b_3\ddot{\mathbf{q}}^{(t)}) + [C_r](b_1\mathbf{q}^{(t)} + b_4\dot{\mathbf{q}}^{(t)} + b_5\ddot{\mathbf{q}}^{(t)})$.

3. Solve for displacements at $(t+\Delta t)$:

$[K_{\text{eff}}]\mathbf{q}^{(t+\Delta t)} = \mathbf{f}_{\text{eff}}^{(t+\Delta t)}$.

4. Calculate accelerations and velocities at $(t+\Delta t)$:

$\ddot{\mathbf{q}}^{(t+\Delta t)} = b_0(\mathbf{q}^{(t+\Delta t)} - \mathbf{q}^{(t)}) - b_2\dot{\mathbf{q}}^{(t)} - b_3\ddot{\mathbf{q}}^{(t)}$

$\dot{\mathbf{q}}^{(t+\Delta t)} = \dot{\mathbf{q}}^{(t)} + b_6\ddot{\mathbf{q}}^{(t)} + b_7\ddot{\mathbf{q}}^{(t+\Delta t)}$,

where $\mathbf{f}_{\text{lin}}$ (step 2) represents the external forces that do not depend on $\mathbf{q}$ (in our case $\mathbf{f}_{\text{lin}} = \mathbf{g}$, see Chapter 3, Eq. (3-46)). Now we set the predictor $\mathbf{q}^{(i)} = \mathbf{q}^{(t+\Delta t)}$, $\dot{\mathbf{q}}^{(i)} = \dot{\mathbf{q}}^{(t+\Delta t)}$, $\ddot{\mathbf{q}}^{(i)} = \ddot{\mathbf{q}}^{(t+\Delta t)}$. The third step of the numerical integration is to do the fix point procedure until convergence is reached:

1. Enter $\mathbf{q}^{(i)}$, $\dot{\mathbf{q}}^{(i)}$, $\ddot{\mathbf{q}}^{(i)}$.

2. Solve for displacements $(i+1)$:

$[K_{\text{eff}}]\mathbf{q}^{(i+1)} = \mathbf{f}_{\text{eff}}^{(t+\Delta t)} + \mathbf{f}_{\text{nonlin}}(\mathbf{q}^{(i)}, \dot{\mathbf{q}}^{(i)}, \ddot{\mathbf{q}}^{(i)})$.

3. Calculate accelerations and velocities $(i+1)$:

$\ddot{\mathbf{q}}^{(i+1)} = b_0(\mathbf{q}^{(i+1)} - \mathbf{q}^{(t)}) - b_2\dot{\mathbf{q}}^{(t)} - b_3\ddot{\mathbf{q}}^{(t)}$

$\dot{\mathbf{q}}^{(i+1)} = \dot{\mathbf{q}}^{(t)} + b_6\ddot{\mathbf{q}}^{(t)} + b_7\ddot{\mathbf{q}}^{(i+1)}$.

4. Check convergence:

$$\text{error} = 2\frac{||\mathbf{q}^{(i+1)} - \mathbf{q}^{(t)}||}{||\mathbf{q}^{(i+1)} + \mathbf{q}^{(t)}||}\,.$$

5. If error $> e$ (where e is the error allowed) we set:

$\mathbf{q}^{(i)} = \mathbf{q}^{(i+1)}$, $\dot{\mathbf{q}}^{(i)} = \dot{\mathbf{q}}^{(i+1)}$, $\ddot{\mathbf{q}}^{(i)} = \ddot{\mathbf{q}}^{(i+1)}$ and we go to step 1.

6. If error $< e$ (convergence is achieved) we set:

$\mathbf{q}^{(t+\Delta t)} = \mathbf{q}^{(i+1)}$, $\dot{\mathbf{q}}^{(t+\Delta t)} = \dot{\mathbf{q}}^{(i+1)}$, $\ddot{\mathbf{q}}^{(t+\Delta t)} = \ddot{\mathbf{q}}^{(i+1)}$.

7. When convergence is achieved, we go to step 1 of the Newmark scheme moving forwards Δt and setting:

$\mathbf{q}^{(t)} = \mathbf{q}^{(t+\Delta t)}$, $\dot{\mathbf{q}}^{(t)} = \dot{\mathbf{q}}^{(t+\Delta t)}$, $\ddot{\mathbf{q}}^{(t)} = \ddot{\mathbf{q}}^{(t+\Delta t)}$,

where $\mathbf{f}_{\text{nonlin}}$ (step 2) represents the forces that depend on $\mathbf{q}$ (in our case $\mathbf{f}_{\text{nonlin}} = (\mathbf{f}_{\text{br}} + \mathbf{f}_{\text{ip}} - \mathbf{f}_{\text{NL}})$, see Chapter 3, Eq. (3-46)).

The MATLAB® functions (*ode*) are also used for the numerical integrations. To do the numerical integration using MATLAB®, the system is written in the state space:

$$\begin{bmatrix} [M_r] & [0] \\ [0] & [M_r] \end{bmatrix} \begin{pmatrix} \dot{\mathbf{q}} \\ \ddot{\mathbf{q}} \end{pmatrix} + \begin{bmatrix} [0] & -[M_r] \\ [K_r] & [C_r] \end{bmatrix} \begin{pmatrix} \mathbf{q} \\ \dot{\mathbf{q}} \end{pmatrix} = \begin{pmatrix} \mathbf{0} \\ \mathbf{f}_r \end{pmatrix} , \tag{D-5}$$

then,

$$\begin{pmatrix} \dot{\mathbf{q}} \\ \ddot{\mathbf{q}} \end{pmatrix} = \begin{bmatrix} [0] & [I] \\ -[M_r]^{-1}[K_r] & -[M_r]^{-1}[C_r] \end{bmatrix} \begin{pmatrix} \mathbf{q} \\ \dot{\mathbf{q}} \end{pmatrix} + \begin{pmatrix} \mathbf{0} \\ \mathbf{f}_r \end{pmatrix} . \tag{D-6}$$

E
Convergence

For the convergence analysis, we use the norm in the Sobolev space [59]:

$$\|f\|_{k,p} = \left(\sum_{i=0}^{k} \left\| f^{(i)} \right\|_p^p \right)^{1/p}, \tag{E-1}$$

where $f^{(i)}$ represents the i-th derivative of function f. In our case, we are in $\mathcal{H}^1$, thus $k = 1$ and $p = 2$:

$$\|f\|_{1,2} = \left(\|f\|_2^2 + \left\| f^{(1)} \right\|_2^2 \right)^{1/2}. \tag{E-2}$$

In our convention, the norm associated with the Euclidian inner product $\|f\|$ is the same as $\|f\|_2$, so the subscript might be dropped. Our function f is the difference between the approximation with a certain number of finite elements (m) and the approximation with less finite elements ($m-1$). Therefore, $\mathbf{f}(t) = \mathbf{u}_r^m(t) - \mathbf{u}_r^{m-1}(t)$, where r stands for any dynamical response (displacement in the axial direction, displacement in the lateral directions, and rotation about the x-axis, y-axis, and z-axis). The relative error is computed as shown in Eq. (E-3).

$$\begin{aligned} \text{error}_r(m,t) &= \frac{\|\mathbf{u}_r^m(t) - \mathbf{u}_r^{m-1}(t)\|_{1,2}}{\|\mathbf{u}_r^m(t)\|_{1,2}} = \\ &= \frac{\left(\|\mathbf{u}_r^m(t) - \mathbf{u}_r^{m-1}(t)\|^2 + \left\| \frac{\partial \mathbf{u}_r^m}{\partial x}(t) - \frac{\partial \mathbf{u}_r^{m-1}}{\partial x}(t) \right\|^2 \right)^{1/2}}{\left(\|\mathbf{u}_r^m(t)\|^2 + \left\| \frac{\partial \mathbf{u}_r^m}{\partial x}(t) \right\|^2 \right)^{1/2}}, \end{aligned} \tag{E-3}$$

Note that the above error depends on time t, since the dynamical response

$\mathbf{u}(t)$ is a function of time. We calculate the mean value

$$\mathrm{ER}(m) = \frac{1}{n_t} \sum_{i=1}^{n_t} \mathrm{error}(m, t_i)\,, \tag{E-4}$$

where n_t is the number of time instants analyzed. The criteria for convergence is

$$\mathrm{ER}(m) < 10^{-3}\,, \tag{E-5}$$

The error of the reduced order model is calculated using the finite element response as the reference. Let n be the number of modes used in the approximation.

$$\begin{aligned} \mathrm{error}_r(n,t) &= \frac{\left\|\mathbf{u}_r^{\mathrm{fe}}(t) - \mathbf{u}_r^n(t)\right\|_{1,2}}{\left\|\mathbf{u}_r^{\mathrm{fe}}(t)\right\|_{1,2}} = \\ &= \frac{\left(\left\|\mathbf{u}_r^{\mathrm{fe}}(t) - \mathbf{u}_r^n(t)\right\|^2 + \left\|\dfrac{\partial \mathbf{u}_r^{\mathrm{fe}}}{\partial x}(t) - \dfrac{\partial \mathbf{u}_r^n}{\partial x}(t)\right\|^2\right)^{1/2}}{\left(\left\|\mathbf{u}_r^{\mathrm{fe}}(t)\right\|^2 + \left\|\dfrac{\partial \mathbf{u}_r^{\mathrm{fe}}}{\partial x}(t)\right\|^2\right)^{1/2}}\,, \end{aligned} \tag{E-6}$$

where $\mathbf{u}_r^{\mathrm{fe}}(t)$ is the response calculated using the Finite Element method. The error independent of time t is given by

$$\mathrm{ER}_r(n) = \frac{1}{n_t} \sum_{i=1}^{n_t} \mathrm{error}_r(n, t_i)\,. \tag{E-7}$$

The criteria for convergence is

$$\mathrm{ER}_r(n) < 10^{-3}\,, \tag{E-8}$$

To choose the number of modes, we take into account this convergence analysis and also the information about the excitation frequency of the system. Which means that if the system is excited with a frequency of 0.83 Hz, then, modes with corresponding natural frequencies of 2.5 Hz ($= 3 \times 0.83$) or less are chosen for the analysis.

F
Data used in the simulation

$L_{\mathrm{dp}} = 1400$ m (length of the drill pipe),
$L_{\mathrm{dc}} = 200$ m (length of the drill collar),
$D_{o\mathrm{dp}} = 0.127$ m (outside diameter of the drill pipe),
$D_{o\mathrm{dc}} = 0.2286$ m (outside diameter of the drill collar),
$D_{i\mathrm{dp}} = 0.095$ m (inside diameter of the drill pipe),
$D_{i\mathrm{dc}} = 0.0762$ m (inside diameter of the drill collar),
$D_{\mathrm{ch}} = 0.3$ m (diameter of the borehole (channel)),
$x_{\mathrm{stab}} = 1400$ m (location of the stabilizer),
$k_{\mathrm{stab}} = 17.5$ MN/m (stiffness of the stabilizer per meter),
$E = 210$ GPa (elasticity modulus of the drill string material),
$\rho = 7850$ kg/m^3 (density of the drill string material),
$\nu = 0.29$ (poisson coefficient of the drill string material),
$k_s = 6/7$ (shearing correcting factor),
$k_{\mathrm{ip}} = 1 \times 10^8$ N/m (stiffness per meter used for the impacts),
$\mu_{\mathrm{ip}} = 0.0005$ (frictional coefficient between the string and the borehole),
$U_{i0} = 4$ m/s (inlet flow velocity),
$\rho_{\mathrm{f}} = 1200$ kg/m^3 (density of the fluid),
$C_{\mathrm{f}} = 0.0125$ (fluid viscous damping coefficient),
$k = 0$ (fluid viscous damping coefficient),
$g = 9.81$ m/s^2 (gravity acceleration),
$a_1 = 3.429 \times 10^{-3}$ m/s (constant of the bit-rock interaction model),
$a_2 = 5.672 \times 10^{-8}$ m/(N.s) (constant of the bit-rock interaction model),
$a_3 = 1.374 \times 10^{-4}$ m/rd (constant of the bit-rock interaction model),
$a_4 = 9.537 \times 10^6$ N.rd (constant of the bit-rock interaction model),
$a_5 = 1.475 \times 10^3$ N.m (constant of the bit-rock interaction model),
$e = 2$ rd/s (regularization parameter).
The damping matrix is constructed using the relationship $[C] = \alpha([M] + [M_{\mathrm{f}}]) + \beta([K] + [K_{\mathrm{f}}] + [K_{\mathrm{g}}(\mathbf{u}_{\mathrm{S}})])$ with $\alpha = 0.01$ and $\beta = 0.0003$.

G
Fluid dynamics

To formulate the fluid-dynamical problem, we first write the continuity equation in cylindrical coordinates

$$\int_{R_i}^{R_o} \left\{ \frac{1}{r}\frac{\partial v_t}{\partial \theta} + \frac{\partial v_x}{\partial x} \right\} dr = 0\,, \tag{G-1}$$

where v_t is the tangential velocity and v_x is the axial velocity of the fluid, and R_i and R_o are the inner and outer radius of the column. The momentum conservation equations in cylindrical coordinates are written as

v_x-momentum

$$\rho_f \left\{ v_x \frac{\partial v_x}{\partial x} + v_r \frac{\partial v_x}{\partial r} + v_t \frac{1}{r}\frac{\partial v_x}{\partial \theta} \right\} =$$

$$-\frac{\partial p}{\partial x} + \rho_f g_x + \mu_f \left[\frac{\partial^2 v_x}{\partial^2 x} + \frac{1}{r}\frac{\partial}{\partial r}\left(r\frac{\partial v_x}{\partial r} \right) + \frac{1}{r^2}\frac{\partial^2 v_x}{\partial \theta^2} \right], \tag{G-2}$$

v_r-momentum

$$\rho_f \left\{ v_x \frac{\partial v_r}{\partial x} + v_r \frac{\partial v_r}{\partial r} + v_t \frac{1}{r}\frac{\partial v_r}{\partial \theta} - \frac{v_t^2}{r} \right\} =$$

$$-\frac{\partial p}{\partial r} + \rho_f g_r + \mu_f \left[\frac{\partial^2 v_r}{\partial^2 x} + \frac{\partial}{\partial r}\left(\frac{1}{r}\frac{\partial}{\partial r}(r v_r) \right) + \frac{1}{r^2}\frac{\partial^2 v_r}{\partial \theta^2} - \frac{2}{r^2}\frac{\partial v_t}{\partial \theta} \right], \tag{G-3}$$

v_t-momentum

$$\rho_f \left\{ v_x \frac{\partial v_t}{\partial x} + v_r \frac{\partial v_t}{\partial r} + v_t \frac{1}{r}\frac{\partial v_t}{\partial \theta} + \frac{v_x v_t}{r} \right\} =$$

$$-\frac{1}{r}\frac{\partial p}{\partial \theta}+\rho_f g_\theta+\mu_f\left[\frac{\partial^2 v_t}{\partial^2 x}+\frac{\partial}{\partial r}\left(\frac{1}{r}\frac{\partial}{\partial r}(rv_t)\right)+\frac{1}{r^2}\frac{\partial^2 v_t}{\partial \theta^2}+\frac{2}{r^2}\frac{\partial v_r}{\partial \theta}\right], \quad \text{(G-4)}$$

where v_r is the radial velocity; ρ_f is the fluid density; and μ_f is the fluid viscosity. Following the ideas found in [83], these equations can be simplified with the following assumptions:

$$v_x, v_t \gg v_r\,, \quad \text{(G-5)}$$

$$\frac{\partial^2 v_x}{\partial r^2} \gg \frac{\partial^2 v_x}{\partial x^2}, \frac{\partial^2 v_x}{\partial \theta^2}\,, \quad \text{(G-6)}$$

and

$$\frac{\partial^2 v_t}{\partial r^2} \gg \frac{\partial^2 v_t}{\partial x^2}, \frac{\partial^2 v_t}{\partial \theta^2}\,. \quad \text{(G-7)}$$

Which means that the radial velocity is much smaller than the axial and tangential velocities because the flow is in the axial direction. And also that the variation of the velocity in the radial direction is much higher than in the other directions, since the drill-string is long and the angle between the column and the borehole along the flow direction is small. The Navier-Stokes equations become:

v_x-momentum

$$0=-\frac{\partial p}{\partial x}+\mu_f\left[\frac{1}{r}\frac{\partial}{\partial r}\left(r\frac{\partial v_x}{\partial r}\right)\right], \quad \text{(G-8)}$$

v_r-momentum

$$0=-\frac{\partial p}{\partial r}\,, \quad \text{(G-9)}$$

v_t-momentum

$$0=-\frac{1}{r}\frac{\partial p}{\partial \theta}+\mu_f\left[\frac{\partial}{\partial r}\left(\frac{1}{r}\frac{\partial}{\partial r}(rv_t)\right)\right]. \quad \text{(G-10)}$$

The eccentricity of the column inside the borehole, depends on x (see Fig. G.1):

$$e(x)=\sqrt{e_1(x)^2+e_2(x)^2}\,, \quad \text{(G-11)}$$

where e_1 and e_2 are the eccentricity in y and z directions. β is the direction

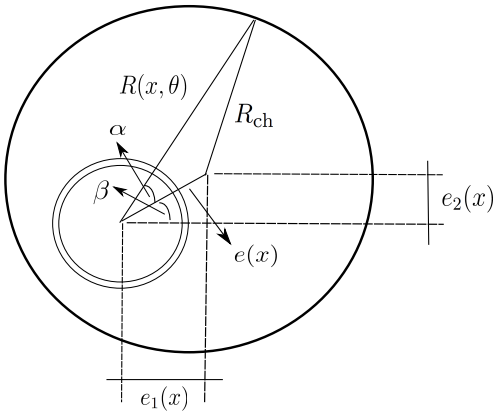

Figure G.1: Eccentricity of the column inside the borehole.

of the eccentricity, $\beta = arctan(e_1/e_2)$, and $\alpha = \theta - \beta$. The radial coordinate of the borehole $R(x,\theta)$ is:

$$R(x,\theta) = e(x)cos\alpha + \sqrt{R_{\text{ch}}^2 + (e(x)sin\alpha)^2}\,. \tag{G-12}$$

For the flow in the annuli, we can use the boundary conditions:

$$v_x|_{r=R_o} = v_x|_{r=R_{\text{ch}}} = v_t|_{r=R_{\text{ch}}} = 0 \quad , \quad v_t|_{r=R_o} = \Omega R_o\,, \tag{G-13}$$

The borehole is fixed but the drill-string rotates at Ω rd/s. For the flow inside the drill-string, we can use the boundary conditions:

$$v_x|_{r=R_i} = 0 \quad , \quad v_t|_{r=R_i} = \Omega R_i\,. \tag{G-14}$$

H
Maximum Likelihood example

To understand what is done in the maximum likelihood method, let X be a real random variable with Normal probability density function and mean $\mu = 0$. Suppose we have one experimental observation x^{exp} and we want to identify the standard deviation σ of the probabilistic model. Figure H.1 illustrates what is done in the maximum likelihood method. We search for the standard deviation σ^* that maximizes the likelihood; for so, we vary the parameter σ. In this simple example is can be noticed that σ^* is between 2 and 4.

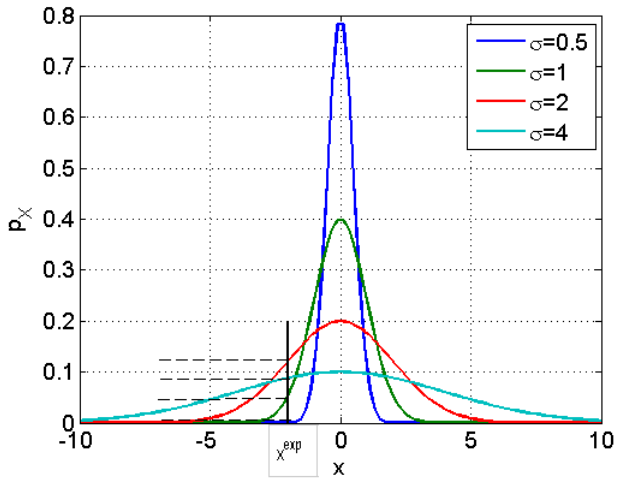

Figure H.1: Simple illustration of the maximum likelihood method.

Of course that if the probabilistic model is that simple a close expression can be found. For the Normal probability density function, the log-likelihood function is written as:

$$L = \log\left[p(x_1^{\text{exp}}, x_2^{\text{exp}}, ..., x_n^{\text{exp}}|\mu, \sigma^2)\right] = \log\left[\prod_{i=1}^{n} p(x_i^{\text{exp}}|\mu, \sigma^2)\right], \qquad \text{(H-1)}$$

where $x_1^{\exp}, x_2^{\exp}, ..., x_n^{\exp}$ is the sample used. Simplifying the above expression

$$L = \log\left[\left(\frac{1}{2\pi\sigma^2}\right)^{n/2} \times \exp\left(-\frac{\sum_{i=1}^{n}(x_i^{\exp}-\mu)^2}{2\sigma^2}\right)\right], \tag{H-2}$$

$$L = \log\left(\frac{1}{2\pi\sigma^2}\right)^{n/2} - \left(\frac{\sum_{i=1}^{n}(x_i^{\exp}-\mu)^2}{2\sigma^2}\right). \tag{H-3}$$

The maximum is calculated setting the first derivative equals to zero.

$$\frac{\partial L}{\partial \mu} = 0 = \underbrace{\frac{\partial}{\partial \mu}\left(\log\left(\frac{1}{2\pi\sigma^2}\right)^{n/2}\right)}_{=0} + \frac{\sum_{i=1}^{n}(\mu - x_i^{\exp})}{\sigma^2}, \tag{H-4}$$

$$\sum_{i=1}^{n}(\mu - x_i^{\exp}) = \mu n - \sum_{i=1}^{n}(x_i^{\exp}) = 0. \tag{H-5}$$

The maximum likelihood estimator for the mean of a Normal random variable is given by

$$\widehat{\mu} = \frac{\sum_{i=1}^{n}(x_i^{\exp})}{n}. \tag{H-6}$$

The same is done for the standard deviation.

$$\frac{\partial L}{\partial \sigma} = 0 = \frac{n}{2}2\pi\sigma^2\frac{-2}{2\pi\sigma^3} + \frac{\sum_{i=1}^{n}(\mu - x_i^{\exp})^2}{2\sigma^3}2, \tag{H-7}$$

$$-\frac{n}{\sigma} + \frac{\sum_{i=1}^{n}(x_i^{\exp}-\mu)^2}{\sigma^3} = 0, \tag{H-8}$$

$$\frac{n}{\sigma} = \frac{\sum_{i=1}^{n}(x_i^{\exp}-\mu)^2}{\sigma^3} = 0. \tag{H-9}$$

The maximum likelihood estimator for the variance of a Normal random variable is given by

$$\widehat{\sigma^2} = \frac{\sum_{i=1}^{n}(x_i^{\exp}-\mu)^2}{n}. \tag{H-10}$$

If the maximum likelihood estimator of the mean is used in the estimation of the variance, there is a correction (to avoid bias).

$$\widehat{\sigma^2} = \frac{\sum_{i=1}^{n}(x_i^{\exp} - \widehat{\mu})^2}{n-1}\,. \tag{H-11}$$

Back to the example, since it was used $\mu = 0$ and $x^{\exp} = -2$, the maximum likelihood estimator for the variance is $\widehat{\sigma^2} = (-2)^2 = 4$ and the standard deviation is $\widehat{\sigma} = 2$.

I
Stress calculation

The numerical simulations give the displacements u, v and w of the neutral line and the section area rotations θ_x, θ_y and θ_z. The displacements written in the non-deformed configuration are

$$\begin{aligned} u_x &= u - y\theta_z + z\theta_y \,, \\ u_y &= v + y(\cos(\theta_x) - 1) - z\sin(\theta_x) \,, \\ u_z &= w + z(\cos(\theta_x) - 1) + y\sin(\theta_x) \,. \end{aligned} \tag{I-1}$$

The components of the Green-Lagrange strain tensor are given by

$$\begin{aligned} \epsilon_{xx} &= \frac{\partial u_x}{\partial x} + \frac{1}{2}\left(\frac{\partial u_x}{\partial x}\frac{\partial u_x}{\partial x} + \frac{\partial u_y}{\partial x}\frac{\partial u_y}{\partial x} + \frac{\partial u_z}{\partial x}\frac{\partial u_z}{\partial x}\right) , \\ \epsilon_{xy} &= \frac{1}{2}\left(\frac{\partial u_y}{\partial x} + \frac{\partial u_x}{\partial y} + \frac{\partial u_x}{\partial x}\frac{\partial u_x}{\partial y} + \frac{\partial u_y}{\partial x}\frac{\partial u_y}{\partial y} + \frac{\partial u_z}{\partial x}\frac{\partial u_z}{\partial y}\right) , \\ \epsilon_{xz} &= \frac{1}{2}\left(\frac{\partial u_z}{\partial x} + \frac{\partial u_x}{\partial z} + \frac{\partial u_x}{\partial x}\frac{\partial u_x}{\partial z} + \frac{\partial u_y}{\partial x}\frac{\partial u_y}{\partial z} + \frac{\partial u_z}{\partial x}\frac{\partial u_z}{\partial z}\right) . \end{aligned} \tag{I-2}$$

Finally, the stress components are computed by

$$\begin{aligned} \sigma_{xx} &= \epsilon_{xx} E \ , \\ \tau_{xy} &= G(2\epsilon_{xy}) \,, \\ \tau_{xz} &= G(2\epsilon_{xz}) \,. \end{aligned} \tag{I-3}$$

The Von Mises stress is calculated as:

$$\sigma(t) = \sqrt{(k_f \sigma_{xx}(t))^2 + 3((k_f \tau_{xy}(t))^2 + (k_f \tau_{xz}(t))^2))} \ , \tag{I-4}$$

where k_f is the stress concentration factor for fatigue. The value of k_f might vary a lot depending on several factors, such as the type of joint, tip radius, etc, [131]. In this work the value used is $k_f = 5$.

J
Damage calculation

In this Section we explain how the damage caused by fatigue is calculated. We use the Goodman-Wohler-Miner model.
(1) Goodman to calculate the equivalent alternate stress (σ_{eq}) that causes a crack initiation.

$$\frac{\sigma_a}{\sigma_{\text{eq}}} + \frac{\sigma_m}{\sigma_{\max}} = 1 \quad \longrightarrow \quad \sigma_{\text{eq}} = \frac{\sigma_a}{1 - \dfrac{\sigma_m}{\sigma_{\max}}} \tag{J-1}$$

where $\sigma_{\max}$ is the ultimate stress limit of the material, σ_a is the alternate Von Mises stress and σ_m is the mean Von Mises stress, calculated as:

$$\sigma_a = \frac{\max\{\sigma\} - \min\{\sigma\}}{2} \quad , \quad \sigma_m = \frac{\max\{\sigma\} + \min\{\sigma\}}{2} \, . \tag{J-2}$$

(2) Wohler (or $\sigma_{\text{eq}} N$) to model the relationship between the stress (σ_{eq}) and the number of cycles (N) that cause a crack initiation.

$$N \sigma_{\text{eq}}^b = c \, , \tag{J-3}$$

where b and c are two positive constants that are obtained fitting experiments. We use $c = 4.16 \times 10^{11}$ and $b = 3$, [78]. Note that the stress value is written in MPa (b and c will have different values for different units).
(3) Miner to calculate the damage cumulation.

$$\tilde{d} = \frac{n}{N} = \frac{n}{c} (\sigma_{\text{eq}})^b \, . \tag{J-4}$$

where n is the number of cycles that the structure has been subjected to.

K
Program structure

Figure K.1 shows a scheme of the program structure. The code was developed using MATLAB® and it has a main file (PRINCIPAL.m) that calls the subroutines. The input parameters, such as material properties and geometry of the structure, are defined in the main file. First, the input parameters are used to compute the mass, damping and stiffness matrices of the system, as well as the natural frequencies and the normal modes. The subroutine sub_beamelement.m is used to compute the element matrices and then sub_normalmodes.m computes the global matrices, the normal modes and the natural frequencies. Using the global matrices and the normal modes (together with the initial conditions) as input, the subroutine sub_dynamics.m does the numerical integration in time and returns the response of the system. Finally, the subroutine sub_pospro.m does the pos-processing returning the graphics, which are used to analyze the response of the computational model.

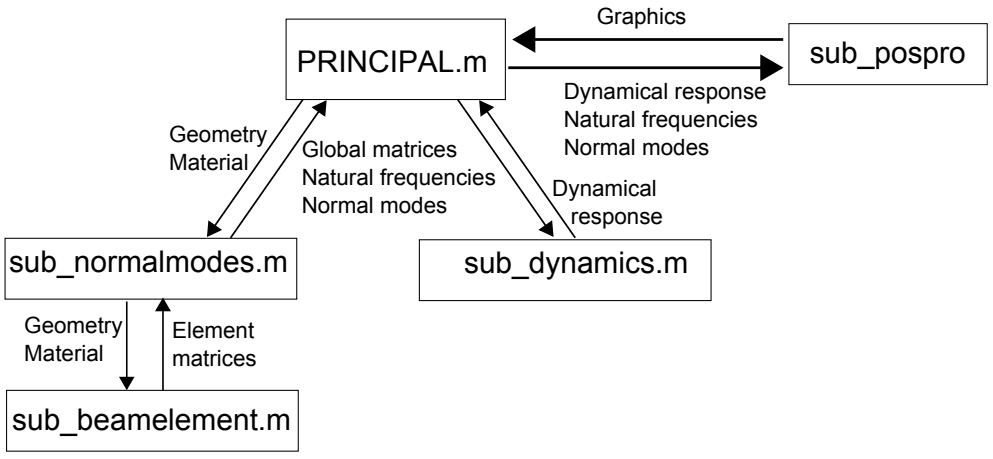

Figure K.1: Scheme of the program structure.

This main file is also used in the stochastic simulation as shown in Fig. K.2. Each random input generates a random output.

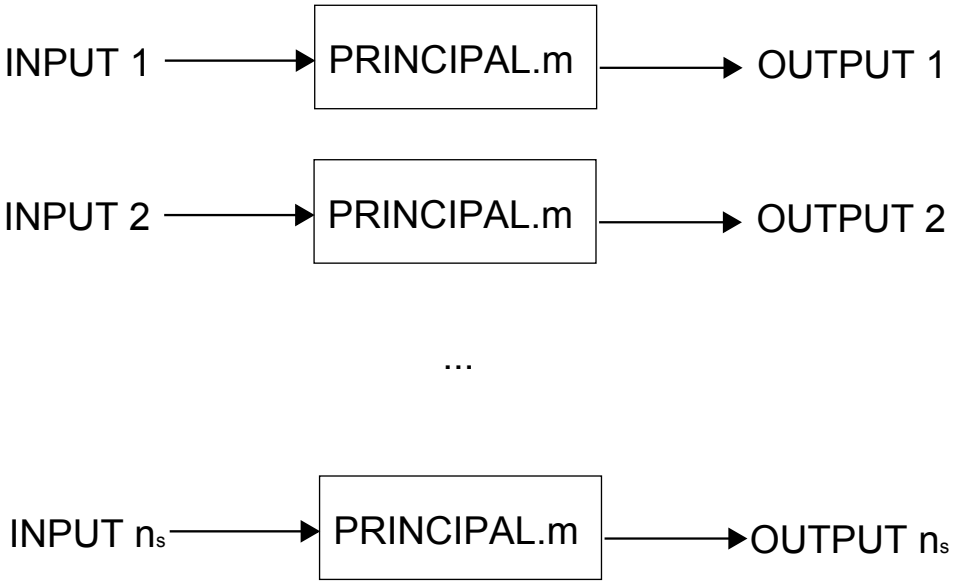

Figure K.2: Stochastic simulations.

Bibliography

[1] ASME. **Handbook: Drilling fluids processing**. Elsevier, Inc., Burlington, Massachusetts, 2005.

[2] ALAMO, F. J. C.. **Dinâmica de estruturas unidimensionais esbeltas utilizando o contínuo de Cosserat**. PhD thesis, PUC-Rio, Brazil, 2006.

[3] ALDRICH, J.. **R.A. Fisher and the making of maximum likelihood 1912–1922**. Statistical Science, 12(3):162–176, 1997.

[4] ALLEMANG, J. R.. **The modal assurance criterion – twenty years of use and abuse**. Sound and Vibration, 37(8):14–21, 2003.

[5] AXISA, F.; ANTUNES, J.. **Flexural vibrations of rotors immersed in dense fluids part I: Theory**. Journal of Fluids and Structures, 6(1):3–21, 1992.

[6] BATHE, K. J.. **Finite Element Procedures**. Prentice-Hall, Inc., Upper Saddle River, New Jersey, 1996.

[7] BAYES, T.. **An essay towards solving a problem in the doctrine of chances**. Trans. Roy. Soc., 53:330–418, 1763.

[8] BAZOUNE, A.; KHULIEF, Y.. **Shape functions of the three-dimensional Timoshenko beam element**. Journal of Sound and Vibration, 259(2):473–480, 2002.

[9] BECK, J. L.; KATAFYGIOTIS, L. S.. **Updating models and their incertainties: Bayesian statistical framework**. Journal of Engineering Mechanics.

[10] BELLIZZI, S.; SAMPAIO, R.. **Smooth Karhunen-Loève decomposition to analyze randomly vibrating systems**. Journal of Sound and Vibration, 325(3):491–498, 2009.

[11] BELLIZZI, S.; SAMPAIO, R.. **Karhunen-Loève modes obtained from displacement and velocity fields: Assessments and comparisons**. Mechanical Systems and Signal Processing, 23(4):1218–1222, 2009.

[12] BEN-TAL, A.; NEMIROVSKI, A.. **Robust optimization – methodology and applications**. Math. Programm., 92(3):453–480, 2002.

[13] BERLIOZ, A.; HAGOPIAN, J. D.; DUFOUR, R. ; DRAOUI, E.. **Dynamic behavior of a drill-string: experimental investigation of lateral instabilities**. Journal of Vibration and Accoustics, 118(3):292–298, 1996.

[14] BERZI, P.; R. BECCU, B. L.. **Identification of a percussive drill rod joint from its response to stress wave loading**. International Journal of Impact Engineering, 18(3):281–290, 1996.

[15] BERTINI, L.; BEGHINI, M.; SANTUS, C. ; BARYSHNIKOV, A.. **Resonant test rigs for fatigue full scale testing of oil drill string connections**. International Journal of Fatigue, 30(6):978–988, 2008.

[16] BISHOP, C. M.. **Pattern recognition and machine learning**. Springer, New York, USA, 2006.

[17] BLEHER, P. M.. **Random matrix models and their applications**. Cambridge University Press, England, 2001.

[18] BREIMAN, L.. **Statistics – With a View Toward Applications**. Houghton Mifflin Company, 1973.

[19] BUEZAS, F. S.; RITTO, T. G. ; SAMPAIO, R.. **Reduced model of a bar impacting an obstacle using the Karhunen-Loève basis.** Mecánica Computacional, XXVII:2195–2219, 2008.

[20] CAPIEZ-LERNOUT, E.; SOIZE, C.. **Robust design optimization in computational mechanics**. Journal of Applied Mechanics, Transactions ASME, 75(2):021001–1–021001–11, 2008.

[21] CHEUNG, S. H.; BECK, J. L.. **Bayesian model updating using hybrid monte carlo simulation with application to structural dynamics models with many uncertain parameters**. Journal of Engineering Mechanics.

[22] CHEN, C.; DUHAMEL, D. ; SOIZE, C.. **Probabilistic approach for model and data uncertainties and its experimental identification in structural dynamics: Case of composite sandwich panels**. Journal of Sound and Vibration, 194(1-2):64–81, 2006.

[23] CHRISTOFOROU, A. P.; YIGIT, A. S.. **Dynamic modeling of rotating drillstrings with borehole interactions**. Journal of Sound and Vibration, 206(2):243–260, 1997.

[24] CHRISTOFOROU, A. P.; YIGIT, A. S.. **Fully coupled vibrations of actively controlled drillstrings**. Journal of Sound and Vibration, 267:1029–1045, 2003.

[25] COUSSOT, P.; BERTRAND, F. ; HERZHAFT, B.. **Rheological behavior of drilling muds, characterization using MRI vizualization**. Oil and Gas Science and Technology, 59(1):23–29, 2004.

[26] CRANDALL, S. H.; MARK, W. D.. **Random Vibration in Mechanical Systems**. Academic Press, Inc., 1963.

[27] CRISFIELD, M. A.. **Nonlinear Finite Element Analysis of Solids and Structures**, volumen 2. John Wiley & Sons, New York, 1997.

[28] DAREING, D.; TLUSTY, J. ; ZAMUDIO, C.. **Self-excited vibrations induced by drag bits**. Journal of Energy Resources Technology, Transactions of the ASME, 112(1):54–61, 1990.

[29] DAUTRAY, R.; LIONS, J.-L.. **Mathematical Analysis and Numerical Methods for Science and Technology**. Springer, Berlin, 1992.

[30] DUCHEREAU, J.; SOIZE, C.. **Transient dynamics in structures with nonhomogeneous uncertainties induced by complex joints**. Mechanical Systems and Signal Processing, 20:854–867, 2006.

[31] DUNAYEVSKY, V.; ABBASSIAN, F. ; JUDZIS, A.. **Dynamic stability of drillstrings under fluctuating weight on bit**. SPE Drilling and Completion, 8(2):84–92, 1993.

[32] DURAND, J. F.; SOIZE, C. ; GAGLIARDINI, L.. **Structural-acoustic modeling of automotive vehicles in presence of uncertainties and experimental identification and validation**. J. Accoust. Soc. Am., 124(3):1513–1525, 2008.

[33] DYKSTRA, M. W.. **Nonlinear drill string dynamics**. PhD thesis, The University of Tulsa, OK, USA, 1996.

[34] EINSTEIN, A.. **On the motion of small particles suspended in liquids at rest required by the molecular-kinetic theory of heat**. Annalen der Physik, 17:549–560, 1905.

[35] ELISHAKOFF, I.; YONGJIAN, R.. **Finite Element Methods for Structures with Large Stochastic Variations**. Oxford University Press, USA, 2003.

[36] ESCUDIER, M. P.; GOULDSON, I. W.; OLIVEIRA, P. J. ; PINHO, F. T.. **Effects of inner cylinder rotation on laminar flow of a newtonian fuid through an eccentric annulus**. International Journal of Heat and Fluid Flow, 21:92–103, 2000.

[37] ESCUDIER, M. P.; OLIVEIRA, P. J. ; PINHO, F. T.. **Fully developed laminar flow of purely viscous non-newtonian liquids through annuli, including the effects of eccentricity and inner-cylinder rotation**. International Journal of Heat and Fluid Flow, 23:52–73, 2002.

[38] FABRO, A. T.; RITTO, T. G.; SAMPAIO, R. ; ARRUDA, J. R. F.. **Stochastic analysis of a cracked rod modeled via the spectral element method**. Mechanics Research Communications, 37:326–331, 2010.

[39] GHANEM, R. G.; SPANOS, P. D.. **Stochastic Finite Elements: A Spectral Approach**. Dover Publications, Inc., Mineola, New York, 2003.

[40] GILARDI, G.; SHARF, I.. **Literature survey of contact dynamics modelling**. Mechanism and Machine Theory, 37:1213–1239, 2002.

[41] GOLDBERG, D. E.. **Genetic Algorithms in Search, Optimization, and Machine Learning**. Addison-Wesley Professional, 1989.

[42] GUEDRI, M.; GHANMI, S.; MAJED, R. ; BOUHADDI, N.. **Robust tools for prediction of variability and optimization in structural dynamics**. Mechanical Systems and Signal Processing, 23(4):1123–1133, 2009.

[43] GUPTA, A.; NAGAR, D.. **Matrix Variate Distributions**. Monographs and Surveys in Pure and Applied Mathematics, Chapman and Hall/CRC, London, England, 2000.

[44] HEISIG, G.. **On the static and dynamic behavior of drill strings in spatially curved boreholes**. PhD thesis, M-Z Technical University, Braunsschweig, 1993.

[45] HOLMES, P.; LUMLEY, J. L. ; BERKOOZ, G.. **Turbulence, coherent structures, dynamical systems and symmetry**. Cambridge University Press, 1996.

[46] HUGHES, T. J. R.. **The Finite Element Method - Linear Static and Dynamic Finite Element Analysis**. Prentice-Hall, Inc., Englewood Cliff, New Jersey, 1997.

[47] JANSEN, J. D.. **Nonlinear dynamics of oilwell drillstrings**. PhD thesis, Technische Universiteit Delft, 1993.

[48] JANSEN, J. D.; VAN DEN STEEN, L.. **Active damping of self-excited torsional vibration in oil well drillstrings**. Journal of Sound and Vibration, 179:647–668, 1995.

[49] JAYNES, E.. **Information theory and statistical mechanics**. The Physical Review, 106(4):1620–630, 1957.

[50] JAYNES, E.. **Information theory and statistical mechanics II**. The Physical Review, 108:171–190, 1957.

[51] JOGI, P. N.; MACPHERSON, J. D. ; NEUBERT, M.. **Field verification of model-derived natural frequencies of a drill string**. Journal of Energy Resources Technology, 124(3):154–162, 2002.

[52] JOLLIFFE, I. T.. **Principal Component Analysis**. Springer-Verlag, New York, M.A. USA, 1986.

[53] KARHUNEN, K.. **Über lineare methoden in der wahrscheinlichkeitsrechnung, ann. acad. sci. fennicae. ser.** A. I. Math.-Phys., 37:1–79, 1947.

[54] KHULIEF, Y. A.; AL-NASER, H.. **Finite element dynamic analysis of drillstrings**. Finite Elements in Analysis and Design, 41:1270–1288, 2005.

[55] KHULIEF, Y. A.; AL-SULAIMAN, F. A. ; BASHMAL, S.. **Vibration analysis of drillstrings with self excited stick-slip oscillations**. Journal of Sound and Vibration, 299:540–558, 2007.

[56] KLEIBER, M.; TRAN, D. H. ; HIEN, T. D.. **The Stochastic Finite Element Method**. John Wiley and Sons, New York, USA, 1993.

[57] KOLMOGOROV, A.. **Foundations of the Theory of Probability**. Chealse, New York, USA, 2nd edition, 1956.

[58] KOTSONIS, S. J.; SPANOS, P. D.. **Chaotic and random whirling motion of drillstrings**. Journal of Energy Resources Technology, 119(4):217–222, 1997.

[59] KREYSZIG, G.. **Introductory functional analysis with applications**. John Wiley and Sons, 1978.

[60] KREE, P.; SOIZE, C.. **Mécanique aléatoire**. Dunod, Paris, France, 1983.

[61] KREE, P.; SOIZE, C.. **Mathematics of Random Phenomena: Random Vibrations of Mechanical Structures (Mathematics and Its Applications)**. Springer, New York, USA, 1986.

[62] LAPLACE, P. S.. **Théorie analytique des probabilités**. Courcier Imprimeur, Paris, France, 1812.

[63] LAPLACE, P. S.. **Essai philosophique sur les probabilités**. Courcier Imprimeur, Paris, France, 1814.

[64] LEAR, W.; DAREING, D.. **Effect of drillstring vibrations on mwd pressure pulse signals**. Journal of Energy Resources Technology, 112(2):84–89, 1990.

[65] LI, M.. **The finite deformation theory for beam, plate and shell part iii. the three-dimensional beam theory and fe formulation**. Computer Methods in Applied Mechanics and Engineering, 162:287–300, 1997.

[66] LIN, Y. K.. **Probabilistic Theory of structural Dynamics**. McGraw-Hill, Inc., 1967.

[67] LOÈVE, M.. **Probability theory**. Graduate Texts in Mathematics. Springer, USA, 4th edition, 1977.

[68] LUMLEY, J. L.. **Stochastic tools in turbulence**. Academic Press, Inc., 1970.

[69] LUTES, L. D.; SARKANI, S.. **Stochastic Analysis of Structural and Mechanical Vibrations**. Prentice-Hall, Inc., Upper Saddle River, New Jersey, USA, 1997.

[70] MACDONALD, K. A.; BJUNE, J. V.. **Failure analysis of drillstrings**. Engineering Failure Analysis, 14:1641–1666, 2007.

[71] MEHTA, M. L.. **Random Matrices**. Academic Press, San Diego, CA, 2nd edition, 1991.

[72] MIGNOLET, M. P.; SOIZE, C.. **Nonparametric stochastic modeling of linear systems with prescribed variance of several natural frequencies**. Probabilistic Engineering Mechanics, 23(2-3):267–278, 2008.

[73] MIGNOLET, M. P.; SOIZE, C.. **Stochastic reduced order models for uncertain geometrically nonlinear dynamical systems**. Computer Methods in Applied Mechanics and Engineering, 197(45-48):3951–3963, 2008.

[74] MISCOW, G. F.; DE MIRANDA, P. E. V.; NETTO, T. A. ; PLÁCIDO, J.. **Techniques to characterize fatigue behaviour of full size drill pipes and small scale samples**. International Journal of Fatigue, 26:575–584, 2004.

[75] MOENS, D.; VANDEPITTE, D.. **A survey of non-probabilistic uncertainty treatment in finite element analysis**. Computer Methods in Applied Mechanics and Engineering, 194(12–16):1527–1555, 2005. Special Issue on Computational Methods in Stochastic Mechanics and Reliability Analysis.

[76] MUKHERJEE, S.; PRATHAP, G.. **Analysis of shear locking in timoshenko beam elements using the function space approach**. Commun. Numer. Meth. Engng, 17:385–393, 2001.

[77] NELSON, H. D.. **A finite rotating shaft element using Timoshenko beam theory**. Journal of Mechanical Design, 102:793–803, 1980.

[78] NETTO, T. A.; LOURENCO, M. I. ; BOTTO, A.. **Fatigue performance of pre-strained pipes with girth weld defects:**

Full-scale experiments and analyses. International Journal of Fatigue, 30:767–778, 2008.

[79] PAEZ, T. L.. **The history of random vibrations through 1958**. Mechanical Systems and Signal Processing, 89:187–200, 2006.

[80] PAIDOUSSIS, M. P.. **Fluid-Structure Interactions: Slender structures and Axial Flow**, volumen 1. Academic Press, London, United Kingdom, 1998.

[81] PAIDOUSSIS, M. P.; LUU, T. P. ; PRABHAKAR, S.. **Dynamics of a long tubular cantilever conveying fluid downwards, which then flows upwards around the cantilever as a confined annular flow**. Journal of Fluids and Structures, 24:111–128, 2008.

[82] PASLAY, P. R.; JAN, Y. M.; KINGMAN, J. E. E. ; MACPHERSON, J. D.. **Detection of lateral ressonances while drilling with surface longitudinal and torsional sensors**. 67th SPE Annual Conferencem Washington, 1992.

[83] PINA, E. P. F.; CARVALHO, M. S.. **Three-dimensional flow of a newtonian liquid through an annular space with axially varying eccentricity**. Journal of Fluids Engineering, 128(2):223–231, 2006.

[84] RICHARD, T.; GERMAY, C. ; DETOURNAY, E.. **A simplified model to explore the root cause of stick–slip vibrations in drilling systems with drag bits**. Journal of Sound and Vibration, 305:432–456, 2007.

[85] RITTO, T. G.; SAMPAIO, R. ; SOIZE, C.. **Influence of the drilling fluid flow on the dynamics of a drill-string**. 8th World Congress on Computational Mechanics (WCCM8), 5th European Congress on Computational Methods in Applied Sciences and Engineering (ECCOMAS 2008), Venice, Italy, 2008.

[86] RITTO, T. G.; SAMPAIO, R. ; CATALDO, E.. **Timoshenko beam with uncertainty on the boundary conditions**. Journal of the Brazilian Society of Mechanical Sciences and Engineering, 30(4):295–303, 2008.

[87] RITTO, T. G.; SOIZE, C. ; SAMPAIO, R.. **Nonlinear dynamics of a drill-string with uncertain model of the bit-rock interaction**. International Journal of Non-Linear Mechanics, 44(8):865–876, 2009.

[88] RITTO, T. G.; SAMPAIO, R. ; SOIZE, C.. **Drill-string dynamics coupled with the drilling fluid dynamics**. Proceedings of the XIII DINAME, Angra dos Reis, RJ, 2009.

[89] RITTO, T. G.; SOIZE, C. ; SAMPAIO, R.. **Stochastic drill-string dynamics – random weight-on-hook**. Proceedings of the XIII DINAME, Angra dos Reis, RJ, 2009.

[90] RITTO, T. G.; SOIZE, C. ; SAMPAIO, R.. **Modeling uncertainties for local nonlinearities: application to the drill-string dynamics**. Proceedings of the 2nd International Conference on Computational Methods in Structural Dynamics and Earthquake Engineering, Rhodes, Greece, 2009.

[91] RITTO, T. G.; SOIZE, C. ; SAMPAIO, R.. **Drill-string dynamics with uncertainty in the bit-rock interaction model**. Proceedings of the 2nd International Conference on Uncertainty in Structural Dynamics, Sheffield, England, 2009.

[92] RITTO, T. G.; SOIZE, C. ; SAMPAIO, R.. **Uncertainties in drill dynamics: the role of a random weight-on-hook**. Proceedings of the ASME 2009 International Design Engineering Technical Conferences and Computers and Information in Engineering Conference, San Diego, USA, 2009.

[93] RITTO, T. G.; SOIZE, C. ; SAMPAIO, R.. **Probabilistic model for the bit-rock interaction model of a drill-string system**. Proceedings of the 20th International Congress of Mechanical Engineering, Gramado RS, Brazil, 2009.

[94] RITTO, T. G.; SOIZE, C. ; SAMPAIO, R.. **Drill-string with uncertainty in the bit-rock interaction**. Proceedings of the 11th Pan-American Congress of Applied Mechanics, Foz do Iguaçu PR, Brazil, 2010.

[95] RITTO, T. G.; SOIZE, C. ; SAMPAIO, R.. **Robust optimization of the rate of penetration of a drill-string using a stochastic nonlinear dynamical model**. Computational Mechanics, 45(5):415–427, 2010.

[96] RITTO, T. G.; SOIZE, C. ; SAMPAIO, R.. **Stochastic dynamics of a drill-string with uncertain weight-on-hook**. Journal of the Brazilian Society of Mechanical Sciences and Engineering, 2010.

[97] RITTO, T. G.; LOPEZ, R. H.; SAMPAIO, R. ; DE CURSI, J. E. S.. **Robust optimization of a flexible rotor-bearing system using the campbell diagram**. Engineering Optimization, 2010.

[98] RUBINSTEIN, R. Y.. **Simulation and the Monte Carlo Method**. Series in Probability and Statistics. John Wiley and Sons, New Jersey, USA, 2nd edition, 2007.

[99] SAMPAIO, R.; RITTO, T. ; CATALDO, E.. **Comparison and evaluation of two approaches of uncertainty modeling in dynamical systems**. Mecánica computacional.

[100] SAMPAIO, R.. **Introdução à Termomecânica dos Meios Contínuos**. SBMAC (CNMAC) 86, 1986.

[101] SAMPAIO, R.; PIOVAN, M. T. ; LOZANO, G. V.. **Coupled axial/torsional vibrations of drilling-strings by mean of nonlinear model**. Mechanics Research Comunications, 34(5-6):497–502, 2007.

[102] SAMPAIO, R.; SOIZE, C.. **Remarks on the efficiency of pod for model reduction in non-linear dynamics of continuous elastic systems**. International Journal for Numerical Methods in Engineering, 72(1):22–45, 2007.

[103] SAMPAIO, R.; RITTO, T. G.. **Short course on dynamics of flexible structures – deterministic and stochastic analysis**. Seminar on Uncertainty Quantification and Stochastic Modeling, PUC-Rio, September, 2008.

[104] SANTOS, H.; PLÁCIDO, J. ; C.WOLTER. **Consequences and relevance of drillstrings vibration on wellbore stability**. SPE/IADC Drilling Conference, 1999.

[105] SCHUELLER, G. I.. **A state-of-the-art report on computational stochastic mechanics**. Probabilistic Engineering Mechanics, 12(4):197–321, 1997.

[106] SERFLING, R. J.. **Approximation Theorems of Mathematical Statistics**. John Wiley and Sons, USA, 1980.

[107] SHANNON, C. E.. **A mathematical theory of communication**. Bell System Tech. J., 27:379–423 and 623–659, 1948.

[108] SHINOZUKA, M.; DEODATIS, G.. **Response variability of stochastic finite element systems**. Journal of Engineering Mechanics, 114(3):499–519, 1988.

[109] SIMO, J. C.. **A finite strain beam formulation. the three-dimensional dynamics problem: part i**. Computer Methods in Applied Mechanics and Engineering, 49:55–70, 1984.

[110] SIMO, J. C.; VU-QUOC, L.. **A three-dimensional finite-strain rod model. part ii: computational aspects**. Computer Methods in Applied Mechanics and Engineering, 58:79–116, 1985.

[111] SIVIA, D. S.. **Data analysis: a Bayesian tutorial**. Oxiford University Press Inc., New York, USA, 1996.

[112] SOIZE, C.. **A nonparametric model of random uncertities for reduced matrix models in structural dynamics**. Probabilistic Engineering Mechanics, 15:277–294, 2000.

[113] SOIZE, C.. **Maximum entropy approach for modeling random uncertainties in transient elastodynamics**. Journal of the Acoustical Society of America, 109(5):1979–1996, 2001.

[114] SOIZE, C.. **PROBABILITÉS ET MODÉLISATION DES INCERTITUDES - Eléments de base et concepts fondamentaux**. Université Paris-Est, Marne-la-Vallée, 2004.

[115] SOIZE, C.. **A comprehensive overview of a non-parametric probabilistic approach of model uncertainties for predictive models in structural dynamics**. Journal of Sound and Vibration, 288(3):623–652, 2005.

[116] SOIZE, C.. **Random matrix theory for modeling uncertainties in computational mechanics**. Computer Methods in Applied Mechanics and Engineering, 194(12-16):1333–1366, 2005.

[117] SOIZE, C.. **Short course on uncertainties and stochastic modeling**. Seminar on Uncertainties and Stochastic Modeling, PUC-Rio, August, 2008.

[118] SOIZE, C.; CAPIEZ-LERNOUT, E.; DURAND, J. F.; FERNANDEZ, C. ; GAGLIARDINI, L.. **Probabilistic model identification of uncertainties in computational models for dynamical systems**

and experimental validation. Computer Methods in Applied Mechanics and Engineering, 198:150–163, 2008.

[119] SOIZE, C.; CAPIEZ-LERNOUT, E. ; OHAYON, R.. **Robust updating of uncertain computational models using experimental modal analysis**. Mechanical Systems and Signal Processing, 22(8):1774–1792, 2008.

[120] SOIZE, C.. **Generalized probabilistic approach of uncertainties in computational dynamics using random matrices and polynomial chaos decompositions**. International Journal for Numerical Methods in Engineering, 81(8):939–970, 2010.

[121] SOLIS, F. J.; WETS, R. J.-B.. **Minimization by random search techniques**. Mathematics of Operations Research, 6(1):19–30, 1981.

[122] SPANOS, P. D.; SENGUPTA, A. K.; CUNNINGHAM, R. A. ; PASLAY, P. R.. **Modeling of roller cone bit lift-off dynamics in rotary drilling**. Journal of Energy Resources Technology, 117(3):197–207, 1995.

[123] SPANOS, P. D.; CHEVALLIER, A. M.. **Non linear stochastic drill–string vibrations**. In: 8TH ASCE SPECIALTY CONFERENCE ON PROBABILISTIC MECHANICS AND STRUCTURAL RELIABILITY, 2000.

[124] SPANOS, P. D.; CHEVALLIER, A. M. ; POLITIS, N. P.. **Nonlinear stochastic drill-string vibrations**. Journal of Vibration and Acoustics, 124(4):512–518, 2002.

[125] SPANOS, P. D.; CHEVALLIER, A. M.; POLITIS, N. P. ; PAYNE, M. L.. **Oil and gas well drilling: A vibrations perspective**. The Shock and Vibration Digest, 35(2):85–103, 2003.

[126] SPALL, J. C.. **Introduction to Stochastic Search and Optimization**. John Wiley and Sons, Hoboken, NJ, USA, 2005.

[127] SPANOS, P.; POLITIS, N.; ESTEVA, M. ; PAYNE, M.. **Drillstring vibrations**. Advanced Drilling and Well Technology (Society of Petroleum Engineers), p. 117–156, 2009.

[128] TRINDADE, M. A.; WOLTER, C. ; SAMPAIO, R.. **Karhunen–Loève decomposition of coupled axial/bending of beams subjected to impacts**. Journal of Sound and Vibration, 279:1015–1036, 2005.

[129] TUCKER, R. W.; WANG, C.. **An integrated model for drill-string dynamics**. Journal of Sound and Vibration, 224(1):123–165, 1999.

[130] TUCKER, R. W.; WANG, C.. **Torsional vibration control and Cosserat dynamics of a drill-rig assembly**. Meccanica, 38(1):143–159, 2003.

[131] VAISBERG, O.; VINCKE, O.; PERRIN, G. ; FAY, J. P. S. J. B.. **Fatigue of drillstring: State of the art**. Oil & Gas Science and Technology, 57(1):7–37, 2002.

[132] VANMARCKE, E.; GRIGORIU, M.. **Stochastic finite element analysis of simple beams**. Journal of Engineering Mechanics, 109(5):1203–1214, 1983.

[133] WIRSCHING, P. H.; PAEZ, T. L. ; ORTIZ, K.. **Random Vibrations: Theory and Practice**. Dover Publications, Inc., New York, USA, 2006.

[134] YIGIT, A.; CHRISTOFOROU, A.. **Coupled axial and transverse vibrations of oilwell drillstrings**. Journal of Sound and Vibration, 195(4):617–627, 1996.

[135] YIGIT, A.; CHRISTOFOROU, A.. **Coupled torsional and bending vibrations of drillstrings subject to impact with friction**. Journal of Sound and Vibration, 215(1):167–181, 1998.

[136] ZANG, C.; FRISWELL, M. ; MOTTERSHEAD, J.. **A review of robust optimal design and its application in dynamics**. Computers and Structures, 83(4–5):315–326, 2005.

[137] ZIENKIEWICZ, O. C.; TAYLOR, R. L.. **The Finite Element Method for Solid and Structural Mechanics**. Butterworth-Heinemann, Woburn, Massachusetts, 6th edition, 2005.

[138] ZUPAN, D.; SAJE, M.. **The three-dimensional beam theory: Finite element formulation based on curvature**. Computers & Structures, 81:1875–1888, 2003.